UNIVERSIDADE DE SÃO PAULO
INSTITUTO DE QUÍMICA DE SÃO CARLOS
DEPARTAMENTO DE FÍSICO-QUÍMICA

PEDRO FARINAZZO BERGAMO DIAS MARTINS

ICP-MS coupled to electrochemistry: correlation of corrosion with catalysis at atomic level

ICP-MS acoplado à eletroquímica: correlação entre corrosão e catálise em nível atômico

SÃO CARLOS, BRAZIL
2019

PEDRO FARINAZZO BERGAMO DIAS MARTINS

ICP-MS coupled to electrochemistry: correlation of corrosion with catalysis at atomic level

ICP-MS acoplado à eletroquímica: correlação entre corrosão e catálise em nível atômico

Tese apresentada ao Instituto de Química de São Carlos da Universidade de São Paulo como parte dos requisitos para a obtenção do título de Doutor em Ciências.

Área de concentração: Físico-Química

Orientador: **Prof. Dr. Edson Antonio Ticianelli**

SÃO CARLOS, BRASIL

2019

DEDICATORY

This work is dedicated to my dad, Francisco Sérgio Dias Martins, the most uprightly, honest and loving human being that I already met. Dad, thank you very much for always supporting me personal and professionally. You are my best friend!

DEDICATÓRIA

Eu dedico este trabalho ao meu pai, Francisco Sérgio Dias Martins, o ser humano mais íntegro, honesto e carinhoso que já conheci. Pai, muito obrigado por sempre me apoiar pessoal e profissionalmente. O senhor é o meu melhor amigo!

ACKNOWLEDGEMENTS

I would like to thank my mom, Debora Farinazzo Bergamo Martins, my dad, Francisco Sérgio Dias Martins, my grandmother and grandfather, Olga Dias Mendes Martins and Marciano Martins Ruiz, and my brother, Francisco Sérgio Dias Martins Júnior for all the moral and personal support throughout my professional career. I'm very thankful for having you as my family, and no word is strong enough to express my gratitude to you. You are and will always be in my heart wherever I am, no matter the physical distance between us.

I'm very thankful to my supervisor Edson Antonio Ticianelli for all academic and professional support, and also for giving me the chance to perform part of my Doctor in Sciences degree at Argonne National Laboratory (USA), where not only I was able to get professionally more mature, but it was also an opportunity for personal development. In the same line, I thank also Pietro Papa Lopes and Nenad M. Markovic for creating this opening, which I've enjoyed tremendously.

To my friends in the Electrochemistry Group at São Carlos (Brazil), for contributing to make the period during my appointment there so pleasurable and smooth, I'm in lifetime debt. Thanks to you, I was able to discover what is real friendship and how precious it is in my life.

To my friends in the Energy Conversion and Storage Group in Argonne National Laboratory (USA), I'm really thankful for all support given personal and professionally.

I would like to acknowledge the Institute of Chemistry of São Carlos (Brazil), which was responsible for tailoring the beginning learning-line process of me (electro)chemistry knowledge. Also, I would like to thank CNPq for the scholarship provided during my doctorate course (Process # 149621/2014-0).

AGRADECIMENTOS

Eu gostaria de agradecer à minha mãe, Debora Farinazzo Bergamo Martins, ao meu pai, Francisco Sérgio Dias Martins, aos meus avós, Olga Dias Mendes Martins e Marciano Martins Ruiz, e ao meu irmão, Francisco Sérgio Dias Martins Júnior, por todo suporte moral e pessoal ao longo da minha carreira profissional. Eu sou muito grato por ter vocês como a minha família, e não há palavras fortes o bastante para expressar a minha gratidão a vocês. Vocês estão e sempre estarão no meu coração aonde quer que eu esteja, não importa a distância física entre nós.

Eu sou muito grato ao meu orientador Edson Antonio Ticianelli por todo suporte acadêmico e profissional, e também por me dar a chance de realizar parte do meu Doutoramento em Ciências no Argonne National Laboratory (EUA), onde não somente amadureci profissionalmente, como também foi um momento de desenvolvimento pessoal. Nesta mesma linha, eu agradeço também a Pietro Papa Lopes e Nenad M. Markovic por criarem esta oportunidade, a qual eu tenho apreciado tremendamente.

Aos meus amigos do Grupo de Eletroquímica de São Carlos (Brasil), por tornar o período do meu Doutoramento em Ciências tão prazeroso e suave, encontro-me eternamente grato. Graças a vocês, eu descobri o significado de amizades verdadeiras, e o quão preciosas são para a minha vida.

Aos meus amigos do Grupo de Conversão e Armazenamento de Energia (EUA), eu sou muito grato por todo apoio pessoal e profissional.

Eu gostaria de agradecer ao Instituto de Química de São Carlos (Brasil), o qual foi responsável por guiar-me durante o começo do meu processo de aprendizado em (eletro)química. Eu gostaria de agradecer também ao CNPq pela bolsa-auxílio concedida para o meu curso de Doutorado em Ciências (Processo: 149621/2014-0).

ABSTRACT

The present work relies on the application of the stationary probe rotating disk electrode inductively coupled plasma mass spectrometry (SPRDE-ICPMS) method approach to examine: the dynamics of the electrochemical dissolution of Pt(111) surface atoms in clean, non-adsorbing $HClO_4$ electrolyte under experimental conditions that are relevant to fuel cell operation; and finally the dynamics of the electrochemical dissolution of crystalline chalcogenide and amorphous chalcogels surface atoms in clean, non-adsorbing $HClO_4$ electrolyte under experimental conditions that are relevant to electrolyzers operation (particularly the hydrogen evolution reaction (HER)). Furthermore, the experimental details of the SPRDE-ICPMS method and its validation are demonstrated. Overall, in Chapter 2 we examine the dynamics of the electrochemical dissolution of Pt(111) surface atoms in clean, non-adsorbing $HClO_4$ electrolyte under experimental conditions that are relevant to fuel cell operation. We focus on Pt(111) surfaces for two reasons: (I) the potential dependent adsorption of oxygenated species are well-established and reasonably well understood; and (II) this surface contains the least amount of surface defects — a structural necessity for exploring oxide/dissolution induced morphological changes at atomic scale. Using these well-defined surfaces, we probed the dynamics of Pt dissolution via the SPRDE-ICPMS, and tracked the concomitant morphological changes using scanning tunneling microscopy (STM). We found that two distinct Pt dissolution processes can take place on the positive going sweep and negative going sweep regions, respectively, during a cyclic voltammetry (CV) with dissolution rates and morphological changes strongly dependent on the experimental conditions. We also found that the rate of dissolution during oxide formation (positive going sweep) is small and can be considered a faradaic process, as it is not closely related to the kinetics of oxide formation. Furthermore, the rate of dissolution and its associated Pt re-deposition is a fast process that is controlled by the positive potential limit and also by the scan rate used for oxide reduction (negative going sweep). Overall, the results provide a strong foundation for understanding how different potential and time profiles have an impact on the stability of Pt surfaces and their corresponding transition from a well-defined to "rough" morphology that ultimately determines the long term electrode durability. In Chapter 3 we present evidence for active site deactivation and regeneration processes that are operational on Mo based chalcogenides (e.g., MoS_2) and chalcogels (e.g., MoS_x) materials. First, by monitoring the in situ dissolution rates of both Mo and S atoms together with HER activity we were able to establish their unique dissolution dynamics in acid media as a

function of the electrode potential. Surprisingly, we found a selective S atom loss with minimal Mo dissolution during HER, whilst at mild positive potentials Mo dissolution happens with minimum S loss. We propose that the selective sulfur release concomitant to H_2 production arise from its interaction to hydronium ions (H^+) and its thermodynamic driving force to form H_2S, while the Mo-S interaction is weakened as part of the HER catalytic cycle at more negative electrode potentials. As a consequence, we found that the selective removal of S leads to Mo-S active site conversion to Mo-O_x species formed by "free" Mo^{n+} that interacts with surrounding H_2O and H^+, creating new surface sites that are less active for hydrogen production (e.g., deactivation). In turn, we also found that this newly Mo-O_x species can be selectively removed from the catalyst surface, giving way for the selective Mo dissolution observed at higher electrode potentials, effectively cleaning the surface and exposing fresh Mo-S sites for the efficient hydrogen production (e.g., regeneration). Finally, our results demonstrate that electrochemical interfaces are constantly evolving, and that understanding the underlying kinetic processes is necessary to successfully design dynamic interfaces that can remain active after extensive electrocatalysis excursions.

RESUMO

O presente trabalho fundamenta-se na aplicação do método da sonda-estacionária acoplada a um eletrodo de disco rotatório (SPRDE) conectado a um inductively coupled plasma mass spectrometry (ICP-MS) para examinar: a dinâmica da dissolução de átomos na superfície de Pt(111) em eletrólito de $HClO_4$ sob condições experimentais relevantes para a operação de células a combustível; e finalmente a dinâmica da dissolução eletroquímica de átomos na superfície de calcogéis amorfos e cristalinos em eletrólito de $HClO_4$ sob condições experimentais relevantes para a operação de eletrolisadores (particularmente a reação de evolução de hidrogênio (HER)). Além disso, os detalhes experimentais do método SPRDE-ICPMS e sua validação são demonstrados. No geral, no Capítulo 2 examinamos a dinâmica da dissolução eletroquímica de átomos de superfície de Pt(111) em eletrólito $HClO_4$ limpo e não adsorvente sob condições experimentais que são relevantes para a operação da célula de combustível. Nós nos concentramos nas superfícies de Pt(111) por duas razões: (I) a adsorção dependente potencial de espécies oxigenadas está bem estabelecida e razoavelmente bem compreendida; e (II) esta superfície contém a menor quantidade de defeitos superficiais - uma necessidade estrutural para explorar mudanças morfológicas induzidas por óxidos/dissolução em escala atômica. Usando estas superfícies bem definidas, nós sondamos a dinâmica da dissolução de Pt através do SPRDE-ICPMS, e rastreamos as mudanças morfológicas concomitantes usando microscopia de tunelamento (STM). Descobrimos que dois processos distintos de dissolução de Pt podem ocorrer nas regiões de varrimento positivo e negativo, respectivamente, durante uma voltametria cíclica (CV) com taxas de dissolução e alterações morfológicas fortemente dependentes das condições experimentais. Descobrimos também que a taxa de dissolução durante a formação de óxido (varrimento positivo) é pequena e pode ser considerada um processo faradáico, uma vez que não está intimamente relacionada com a cinética de formação de óxido. Além disso, a taxa de dissolução e seu depósito de Pt associado é um processo rápido que é controlado pelo limite de potencial positivo e também pela taxa de varredura usada para redução de óxido (varredura negativa). No geral, os resultados fornecem uma base sólida para entender como diferentes perfis de tempo e potencial têm impacto sobre a estabilidade das superfícies de Pt e sua correspondente transição de uma morfologia bem definida para "rugosa" que determina a durabilidade do eletrodo a longo prazo. No Capítulo 3, apresentamos evidências de processos de desativação e regeneração de sítios ativos que estão operacionais em calcogenetos baseados em Mo (por exemplo, MoS_2) e calcogéis (por exemplo, MoS_x). Primeiro, monitorando as taxas de dissolução in situ de ambos os átomos, Mo e S, juntamente com a atividade de HER, fomos

capazes de estabelecer sua dinâmica única de dissolução em meio ácido em função do potencial do eletrodo. Surpreendentemente, encontramos uma perda seletiva de átomos de S com mínima dissolução de Mo durante o HER, enquanto nos potenciais positivos moderados a dissolução de Mo ocorre com perda mínima de S. Propomos que a liberação seletiva de enxofre concomitante à produção de H_2 provenha de sua interação com íons hidrônio (H^+) e sua força motriz termodinâmica para formar H_2S, enquanto a interação Mo-S é enfraquecida como parte do ciclo catalítico HER a mais negativo potenciais do eletrodo. Como conseqüência, descobrimos que a remoção seletiva de S leva à conversão do sítio ativo de Mo-S em espécies Mo-O_x formadas por Mo "livre" (Mo^{n+}) que interage com H_2O e H^+ circunvizinhos, criando novos sítios de superfície que são menos ativo para a produção de hidrogênio (por exemplo, desativação). Por sua vez, também descobrimos que essa nova espécie de Mo-O_x pode ser removida seletivamente da superfície do catalisador, dando lugar à dissolução seletiva de Mo observada em maiores potenciais de eletrodos, limpando efetivamente a superfície e expondo locais virgens de Mo-S para a produção eficiente de hidrogênio (por exemplo, regeneração). Finalmente, nossos resultados demonstram que as interfaces eletroquímicas estão em constante evolução, e que a compreensão dos processos cinéticos subjacentes é necessária para projetar com sucesso interfaces dinâmicas que podem permanecer ativas após extensas excursões de eletrocatálise.

LIST OF FIGURES

Contents

Page intentionally left blank

CHAPTER 1

GENERAL INTRODUCTION

1 General introduction

I would like to make clear that this section is based on my own point of view about the subject and, therefore, it was written as a first-person narrative.

From the confirmation of the Giant-Impact theory for the origin of the Moon to the determination on how the climate changes are affecting the Earth's history and nature of weathering, sedimentary processes, biological productivity, and ocean chemistry, inductively coupled plasma mass spectrometry (ICP-MS) has coined its place on the realm of fundamental analytical tools for science. Thanks to its development (first commercial instrument sold in 1983), medical doctors can determine a highly quantitative drug administration routine for patients that has had been exposed to and contaminated by heavy metals, tribunals can correctly judge an individual for using a knife found 'free' of any apparent physical evidence in his/her car trunk, but that cares the same proportion of metals and its isotopes present at the victim's body wounds. Unlike any other atomic spectroscopy instrumentation (*e.g.*, atomic absorption (AA)), ICP-MS is capable of measuring large quantities of different elements at the same time, providing faster, less dispendious experimentation procedures for industries, forensics, pharmaceutical laboratories, etc. Quoting Robert Thomas[1], *"ICP-MS not only offers extremely low detection limits in the sub parts-per-trillion (ppt) range, but also enables quantitation at the high parts-per-million (ppm) level. This unique capability makes the technique very attractive compared to other trace metal techniques such as electrothermal atomization (ETA), which is limited to determinations at the trace level, or flame atomic absorption (FAA) and inductively coupled plasma optical emission spectrometry (ICP-OES), which are traditionally used for the detection of higher concentrations"*. Figure 1 shows the detection limits for almost all elements in the periodic table (isotopic abundance shown for all elements)[2] using an ICP-MS instrument. Therefore, it is not surprising that since its first commercial release; more than 11,000 instruments were installed around the globe despite its relatively high price (approximately 14 times more expensive than an AA instrument).

Figure 1. Approximate detection capability of ICP-MS instruments produced by PerkinElmer, together with elemental isotropic abundance.

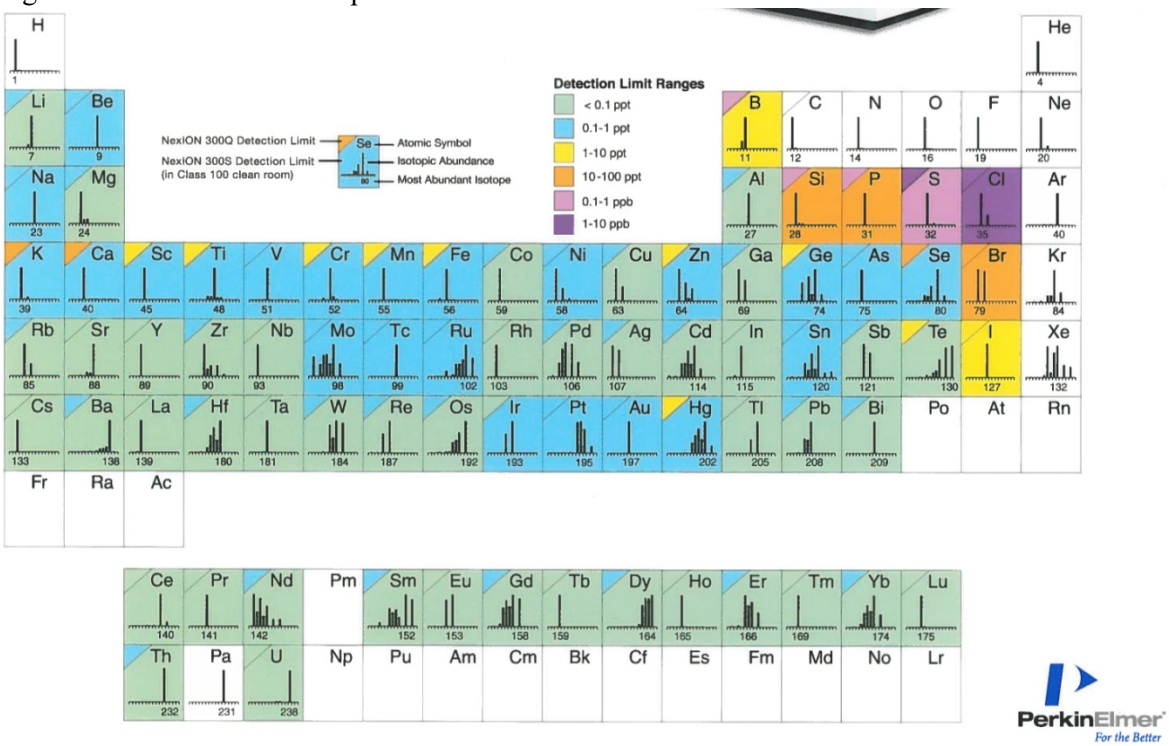

Source: Courtesy of PerkinElmer, Inc., © 2003-2018. All rights reserved. With permission.

It is not my purpose to describe in a detailed fashion all principles of operation for a typical ICP-MS instrument; this can be readily accessible in current literature[1,3]. However, based on the meaning of the term 'Dissertation', which derives from the Latin *dissertātiō*, meaning "*path*", I would be wrong if not provided the paths towards the understanding of my final doctoral degree findings as clear and as self-explanatory as possible, trying, in turn, to avoid being tedious and prolonged.

1.1 The inductively coupled plasma mass spectrometry (ICP-MS) instrument

Any ICP-MS system follows the same basic physical steps regardless of how it was designed. The word “basic” used above is very well put, since several designs of ICP-MS from each company can, and usually are, completely different in terms of how the performance of the instrument is maximized. In any case, the fundamental steps continue always to be meticulously respected (Figure 2). First, the analyte and the matrix in which it is contained have to be inserted into argon plasma as aerosol droplets (sample introduction). The high temperature (energy) of the plasma (around 6,000 K, equal to the temperature at the surface of the sun (this is in fact the closest that we can get safely an instrument to the ‘sun’)) readily ionizes the sample, which is then directed into a mass spectrometer (sampling). Most ICP-MS commercially available employ a quadrupole mass spectrometer (MS), which allows only ions of a particular isotope to pass through at any given time (speciation). These ions strike an electron multiplier (detection) releasing a cascade of electrons, which are amplified to ensure that a measurable pulse is generated. Finally, the software compares the intensities of these measurable pulses to those created by the standards (calibration curve) to identify the concentration of that isotope. One may wonder why I use the word isotope instead of element, and this is to emphasize the exceptional capability of ICP-MS to measure accurately and quantitatively any isotope from a particular element. Why is this feature useful? A simple answer is the case of lead (Pb). Unlike the rest of the naturally occurring elements, Pb does not follow the natural isotope abundance rule; it can occur naturally from two sources: one is the Pb placed in the earth upon its creation, and the other one is the result of the radioactive decaying of some elements. In other words, Pb has different isotopic ratios depending where it was collected. Therefore, in order to perform an accurate measurement of Pb concentration in any sample, it is necessary to consider the sum of several Pb isotopes available.

Figure 2. Basic instrumental components of a typical ICP-MS system.

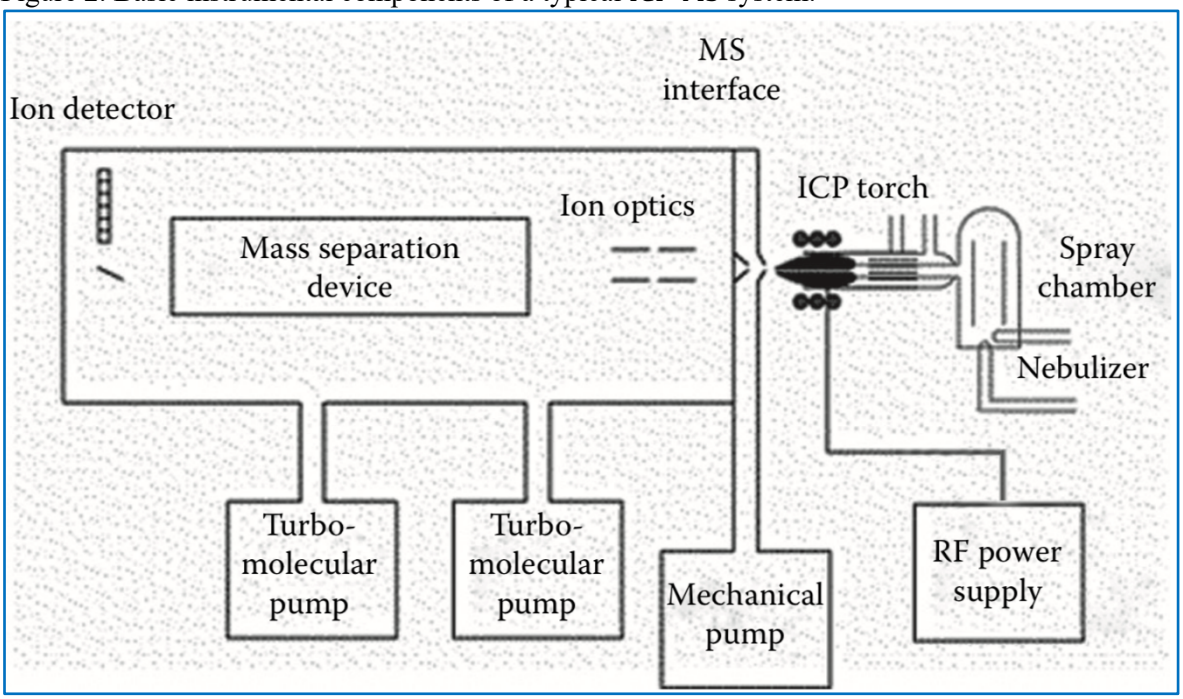

Source: image reproduced from Thomas, R. Practical Guide to ICP—MS. (CRC Press, 2013)[1]. With permission.

1.2 The inductively coupled plasma mass spectrometry ICP-MS and the electrochemistry community

Being working in the field of electrocatalysis applied to fuel cells, electrolyzers and batteries since my undergraduate course in Chemistry, it is surprising to me that only 28 years after the first commercialization of an ICP-MS instrument, the electrochemistry community started to pay more attention to it and successfully coupled this analytical technique towards the understanding of the electro(chemical) processes occurring at electrode surface/electrical double layer interfaces[4]. For instance, corrosion and dissolution events have been one of the most impediment to the success deployment of long-term affordable electrochemical devices[5,6]. Moreover, corrosion processes are responsible for astronomical debts designated to maintain metal structures in the environment. In Unites States (US), the impact of corrosion is estimated to be 276 billions of US dollars, which represents 3.1% of US gross domestic product (GDP)[7].

On 2005, Shao-Horn and co-authors[8] used a ICP instrument to measure the concentration of platinum (Pt) in acid electrolyte collected after a determined electrochemical routine. However, this powerful analytical technique was applied merely to identify and confirm the presence of Pt ions dissolved in the electrolyte collected after applying different potentials on electrodes based on carbon supported Pt nanoparticles (Pt-C); it was found that equilibrium concentrations of dissolved Pt species in 0.5 mol L^{-1} of H_2SO_4 at 353 K increase with applied potential from 0.9 to 1.1 V vs. reversible hydrogen electrode (RHE), trend also found in Pourbaix's Atlas of Electrochemical Equilibria in Aqueous Solutions dated back to 1966[9]. Only by sophisticated and ex situ techniques like incidence angle X-ray diffraction and transmission electron microscopy it was possible to propose that the coarsening of Pt nanoparticles was responsible for the low stability of polymer electrolyte membrane fuel cells (PEMFCs). Moreover, by this experimental approach, it is only possible to observe the final stage ('postmortem') of an electrode after any particular electrochemical process; so, any attempt to correlate its dissolution processes with its electrocatalysis performance is senseless. On 2006, Myers and co-authors[10] used ex situ ICP-MS to determine the amount of Pt dissolved during electrochemical events related to the PEMFCs. The potentiostatic conditions relevant to PEMFC cathode electrodes were applied to study the long-term dissolution behavior of Pt-C and Pt polycrystalline (Pt(Poly)) in 0.57 mol L^{-1} of $HClO_4$. The authors concluded that the equilibrium concentrations of dissolved Pt species increase from 0.65 to 1.1 V vs. standard hydrogen electrode (SHE) (very similar to Shao-Horn and

co-authors' findings[8]) and decrease at potentials higher than 1.1 V vs. SHE. An attempt to determine the $_{Pt}$ dissolution rate was made by calculating the slope of the curve generated by analyzing the concentration of Pt species present in the electrolyte that was collected during the first 6 h at different time intervals with the electrode polarized at 0.9 V vs. SHE. The dissolution rates for Pt bulk and nanoparticles were comparable (1.4 and 1.7×10^{-5} ng cm^{-2} s^{-1}). Two main drawbacks are readily observed by the current analysis approach: first, similar to Shao-Horn and co-authors' study[8], no dissolution and electrochemical event can be directly correlated; and second, the graph of dissolution vs. time obtained for the first 70 h (please see fig. 1 of reference [10]) showed that the rate of dissolution is a transient phenomenon, which implies that the dissolution rates calculated are a roughly approximation at most.

The examples above suggest that the directly coupling of ICP-MS to an electrochemical cell (EC) was overdue.

1.3 The electrochemical cell (EC) and inductively coupled plasma mass spectrometry (ICP-MS) systems coupling (EC-ICPMS)

Why in situ measuring the electrode surface dissolution during an electrochemical cell operation is important? For instance, it provides a distinction between the dissolved and precipitated form of ions and allows associating the overall net current to the dissolution of specific elements in multi-component systems. For more than four decades the electrochemistry community had been working on the development of practical electrodes to be applied in fuel cells[11–16]. It is important to keep in mind that even if the fuel cell electrodes are composed of metal (mainly Pt) nanoparticles supported on a high surface area carbon[17], a controlled (chemically and physically homogeneous) and reproducible surface is mandatory to one be able to make any correlation assumptions between structure-(electrochemical)activities. In the early 1980s, thanks to a new approach developed by Clavilier and co-authors[18] to prepare single-crystal surfaces a new door was opened towards the reproducible single-crystal experimental results and consequently, reliable structure-activity relationships were defined for several single-crystal metals (platinum[19,20], gold[21], etc.[22]). These relationships formed the basis for the tailored design of more active materials for fuel cells electrochemical reactions (oxygen reduction reaction, ORR, and hydrogen oxidation reaction, HOR) ever since. For instance, one of the most successful use of the structure-active relationship was made by Stamenkovic and co-workers[23]. By a careful and meticulous experimental routine, the authors were able to not only identify the most active electrocatalyst for ORR, but also to make precisely correlations between the electronic and structure of each bi-metallic single-crystal alloys to their respective electrocatalysis activity performances output. Several other reports were subsequently released by other research groups[24–26], which make the structure-active relationship the basis of any predictive ability in tailor-making nanomaterials with desirable properties, often called as materials by design strategy. One may ask: are these high active materials also stable under realistic experimental conditions? In earlier reports, the stability of surface atoms has been examined by monitoring the potential-dependent change in surface morphology, either by utilizing cycling voltammetry (CV) alone[27] or by a combination of CVs and scanning tunneling microscopy (STM)[28–31] or surface X-ray scattering (SXS)[32–35]. Although these approaches were successful in measuring oxide-induced changes in both the local structure of surface atoms (STM) and long-range roughening of well-defined single-crystals (SXS), these methods were unable to provide any information about the corrosion of metal surface atoms. Therefore, to answer the question above, we need to understand first the correlations between

the stability of the atoms present in the electrode surface with its atomic-level surface structure (structure-stability relationships). It is the route to these relationships understanding that makes the EC-ICPMS system a very desirable method.

The 2018 fiscal year project budget of the Department of Energy (DOE) of United States (US) dedicated to the study of the parameters that are responsible for the dissolutions processes in electrodes employed in fuel cells, in order to implement rational design approaches for the synthesis of electrochemically stable surfaces, is of ~4 million US dollars[36]. Therefore, research groups involved in this project should have no issues regarding the costs for the purchase of an ICP-MS instrument and the proper maintenance routines. Shockingly, up to now, September of 2018, none of those research groups implemented a proper in situ ICP-MS method to any electrochemical system. Under these circumstances, my guess is that one the reasons for the late implementation of ICP-MS as a direct coupled analytical system to any type electrochemical cell may be the engineering complexity to create a feasible physical interface EC-ICPMS which guarantees accurate and reproducible data[37]. The first relatively successful attempt to my knowledge was made by Mayrhofer and co-authors[4] in 2011 at Germany. By means of a scanning flow cell (SFC) coupled to an ICP-MS, the authors enabled in situ measurements of the dissolution of polycrystalline metal electrodes. This method made possible to establish relationships between potential-dependent oxide formation in various environments (pH 1-13, presence of chlorine anions (Cl^-), and reactive atmospheres such as di-hydrogen (H_2), di-oxygen (O_2), and carbon monoxide (CO)) and the dissolution of the corresponding cations with high sensitivity (ca. 3 pg $cm^{-2}s^{-1}$). Despite the breadth of these experiments, knowledge of potential-induced surface stability at atomic/molecular levels still remains incomplete, even for platinum-based materials. Two key fundamental and technical barriers that limited a deep understanding are: (I) current in situ ICP-MS methodologies are not sensitive enough to probe the stability of various defects such as ad-islands and step edges that are inherently present on single-crystal surfaces and (II) there is no experimental strategy capable of simultaneously monitoring stability-reactivity relationships at well-defined surfaces and under well-established diffusion/kinetic conditions. The development of such a methodology would offer the ability to embrace a science-based strategy capable of exploring, at atomic/molecular levels, the role of covalent and noncovalent interactions in metal dissolution/activity rates. It is reasonable to anticipate that establishing such activity-stability trends on well-defined single-crystals in various electrochemical environments would open new opportunities for elucidating key fundamental descriptors that govern these processes

and, ultimately, make use of these descriptors to develop reliable energy conversion and storage systems.

As mentioned earlier, the bottle neck for successful implementation of ICP-MS to an electrochemical cell is its physical interface connection. Thanks to the brilliant approach made by Markovic and co-authors[38], this problem was masterly solved. The authors developed a stationary probe (SP) coupled to ICP-MS, combined with a rotating disk electrode (RDE), then called SPRDE-ICPMS method, to study the role of surface geometry on the stability of surface atoms and enable "atom-by-atom" detection of the adsorbate-induced dissolution of atoms in both acidic and alkaline environments. This work is the first true and reliable attempt to make correlations between structure with stability at atomic/molecular levels.

1.4 The stationary probe rotating disk electrode-inductively coupled plasma mass spectrometry (SPRDE-ICPMS) method applied to both well and poorly organized electrocatalyst material surfaces

The present work relies on the application of the $SPRDE\text{-}ICPMS$ method[38] approach to examine: in Chapter 2, the dynamics of the electrochemical dissolution of $Pt(111)$ surface atoms in clean, non-adsorbing $HClO_4$ electrolyte under experimental conditions that are relevant to fuel cell operation[39];and in Chapter 3, the dynamics of the electrochemical dissolution of crystalline chalcogenide and amorphous chalcogels surface atoms in clean, non-adsorbing $HClO_4$ electrolyte under experimental conditions that are relevant to electrolyzers operation (particularly the hydrogen evolution reaction (HER)). The experimental details of the $SPRDE\text{-}ICPMS$ method and its validation are exposed in the following chapter.

CHAPTER 2

DYNAMICS OF ELECTROCHEMICAL Pt DISSOLUTION AT ATOMIC AND MOLECULAR LEVELS

2 Dynamics of electrochemical Pt dissolution at atomic and molecular levels (Journal of Electroanalytical Chemistry, 2018, v. 819, pp. 123-129, DOI: 10.1016/j.jelechem.2017.09.047)

The content of this chapter has been derived from the above publication with some minor technical modifications. Some of the experimental procedures were extended and more detailed exposed in order to make the chapter as self-contained as possible. Any omitted experimental details were properly cited in case the reader finds it useful to complement his/her knowledge about the subject.

2.1 Introduction

Understanding and controlling electrochemical interfaces at atomic and molecular levels have transformed electrochemistry from primarily phenomenological event description to a science with clearly defined fundamental principles that have led to the discovery of a new generation of energy conversion and storage systems [40,41], the production of clean chemicals[42], the design of superior (bio)sensors[43,44], the development of advanced electroplating techniques[45,46], and more efficient corrosion protection strategies[47–49]. A major contributing factor was the development of reliable experimental methods that enabled the study of well-defined metal single-crystal surfaces in clean electrochemical environments[18,50].

Single-crystalline surfaces of Pt have been subject to intense studies since the beginning of the 1980s, as Pt is one of the best-known catalysts for a variety of electrochemical reactions, including the fundamentally intriguing bond-making and bond-breaking events at electrochemical interfaces that drive energy conversion processes[22,51–56]. One of such examples is the formation of the puzzling "butterfly" feature that is observed in the current-voltage curve on $Pt(111)$ in both H_2SO_4 and $HClO_4$ solutions (see example for $HClO_4$ solution at Figure 3). It took years of heated debate to interpret the true nature of the "butterfly", which many of those working with Pt single-crystals today may take for granted. Whereas in H_2SO_4 the "butterfly" is formed by adsorption-desorption of (bi)sulfate anions, in $HClO_4$ the "butterfly" is shaped by the adsorption-desorption of hydroxyl species[22]. Unfortunately, there are many ways one can destroy the beauty of the "butterfly"; for example, by adding trace levels of impurities in the supporting electrolyte or simply through the formation of irreversible oxide, which transforms well-ordered single-crystals to rougher surfaces with various types of structural defects[27,57–61].

Figure 3. Typical cyclic voltammetry (CV) for $Pt(111)$ in clean 0.1 $mol\,L^{-1}$ of $HClO_4$ solution at several scan rates.

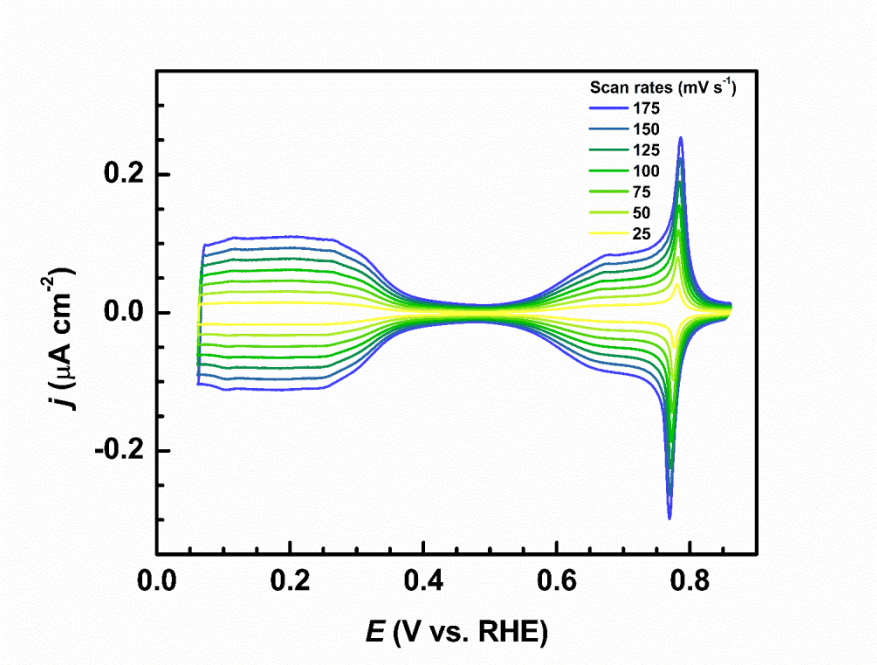

Source: own authorship.

Besides the simple change in morphology, the formation/reduction of irreversibly formed oxide is believed to be associated with the dissolution (corrosion) of surface atoms. Although such a supposition is plausible, microscopic characterization of the stability of oxide single-crystal surfaces and investigations of the corresponding dissolution kinetics have rarely been explored due to the lack of methods available for establishing such structure-stability relationships. Very recently, however, we introduced a new method that is capable of providing highly quantitative information about the stability of single-crystal electrodes during electrochemical processes, allowing for in situ monitoring of the dissolution of metal atoms almost "atom-by-atom"[38]. This method has helped in exploring the role of surface structure and adsorbate-induced Pt dissolution processes, showing that dissolution primarily takes place concomitantly with oxide reduction. Nevertheless, it is still intriguing as to how the combined effect of time and potential may impact the dynamics of Pt dissolution, as these two parameters are crucial in defining the amount of oxide formation and reduction processes[27,59,62].

In this chapter, we examine the dynamics of the electrochemical dissolution of $Pt(111)$ surface atoms in clean, non-adsorbing $HClO_4$ electrolyte under experimental conditions that are relevant to fuel cell operation. We focus on $Pt(111)$ surfaces for two reasons: (I) the potential-dependent adsorption of oxygenated species are well-established and reasonably well understood[22,54,55,63]; and (II) this surface contains the least amount of

surface defects[61,64] — a structural necessity for exploring oxide/dissolution-induced morphological changes at atomic scale. Using these well-defined surfaces, we probed the dynamics of Pt dissolution via the stationary probe rotating disk electrode (SPRDE) method coupled to inductively coupled plasma mass spectrometry (ICPMS), and tracked the concomitant morphological changes using scanning tunneling microscopy (STM). We found that two distinct Pt dissolution processes can take place on the positive going sweep and negative going sweep regions, respectively, during a cyclic voltammetry (CV) with dissolution rates and morphological changes strongly dependent on the experimental conditions. We also found that the rate of dissolution during oxide formation (positive going sweep) is small and can be considered a faradaic process, as it is not closely related to the kinetics of oxide formation. Furthermore, the rate of dissolution and its associated Pt re-deposition is a fast process that is controlled by the positive potential limit and also by the scan rate used for oxide reduction (negative going sweep). Overall, the results provide a strong foundation for understanding how different potential and time profiles have an impact on the stability of Pt surfaces and their corresponding transition from a well-defined to "rough" morphology that ultimately determines the long-term electrode durability.

2.2 Experimental procedures

2.2.1 Description of the stationary probe rotating disk electrode ($SPRDE$) setup — the 'wizard wand' that enabled the 'magic' connection between structure with stability of electrocatalyst materials at atomic and molecular levels

The stationary probe rotating disk electrode (SPRDE) setup is shown in Figure 4; metal ions were detected with a PerkinElmer ICP-MS instrument (NexION 300S). The crystal preparation procedures and electrochemical measurements are described in the next section (2.2.2). The stationary probe (SP) consists of a polychlorotrifluoroethylene (PCTFE) capillary tube (400 µm inner diameter (i. d.)) positioned at the edge of the disk electrode, less than 1 mm distant from the disk surface, with electrolyte flow direction perpendicular to the electrode surface normal direction. To avoid any height adjustments between the probe and electrode surface, as it would change collection efficiency (N) (described in the following paragraph), the whole probe was precisely machined and easily inserted into the probe holder fixed in the rotator case (Pine Instruments MSR). This setup led to N values with no more than 5% variation between each experiment.

Figure 4. The stationary probe rotating disk electrode (SPRDE) setup scheme used to analyze the dissolution processes happening during the electrochemical phenomena on electrocatalyst materials. ICP-MS: inductively coupled plasma mass spectrometry; Pt(hkl): platinum single-crystals with low-index surface structure (hkl) = (111), (100), or (110)); Pt(NP): platinum nanoparticles.

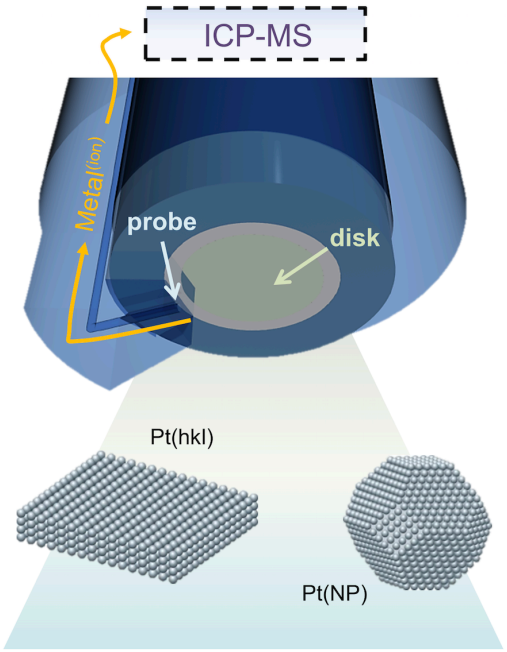

Source: image reproduced from Lopes, P. P. et al. Relationships between Atomic Level Surface Structure and Stability/Activity of Platinum Surface Atoms in Aqueous Environments. ACS Catal. 6, 2536–2544 (2016)[38]. With permission.

In order to study structure-stability relationships on single-crystal electrodes at the same well-established conditions as those used for obtaining structure-activity relationships[22,23,40], Markovic and co-authors[38] developed a SPRDE setup able to collect dissolved ions from the electrode surface and transfer them at reasonable flow rates to an ICP-MS instrument to gain in situ information with high sensitivity under unaltered kinetic conditions. In a way, this new SPRDE setup resembles the ring-disk method, with the probe functioning in almost the same way as the ring electrode[65]. As it only collects a fraction of the ions produced at the surface, it is necessary to determine the N for the system (Figure 5(a)). For that we used a silver (Ag) polycrystalline electrode (Ag(Poly)), as its continuous dissolution at electrode potentials above 0.6 V vs. RHE can be used to correlate corrosion current (univalent cation, Ag^+) and concentration of Ag^+ in solution measured by external standard solutions (called here as method α).

Figure 5. Experimental determination of the SPRDE collection efficiency (N). (a) Polycrystalline silver (Ag(Poly)) electrode is used to provide constant dissolution at potentials above 0.6 V vs RHE, and analysis of the real time in situ dissolution measured by ICP-MS as depicted in (a) can be used to obtain the N values plotted in (b) showing the dependence of N with electrode rotation (ω) values for a given flow rate (f_{pump}) and total cell solution volume (V_{cell}). I_d = the ion count in arbitrary units (a. u.). Δt = time interval used for integration ($\int_{\Delta t}$) process.

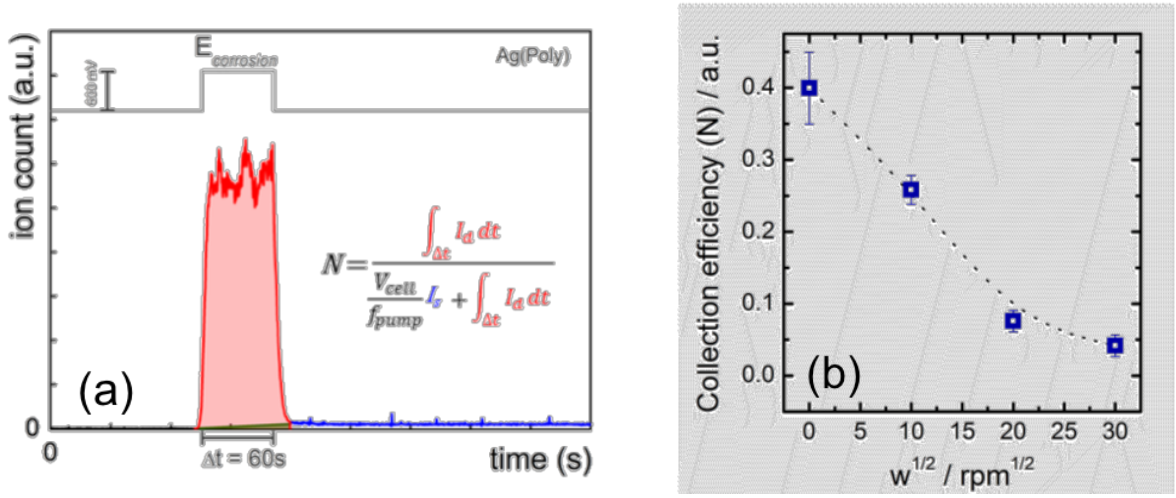

Source: image reproduced from Lopes, P. P. et al. Relationships between Atomic Level Surface Structure and Stability/Activity of Platinum Surface Atoms in Aqueous Environments. ACS Catal. 6, 2536–2544 (2016)[38]. With permission.

Another way of obtaining the value of N is by correlating the dissolution profile under a corrosion potential step, as shown in Figure 5(a), and making use of mass balance to account for the fact that part of the ions generated from the surface will go to the probe and the remaining will go to the bulk of the electrolyte contained in the cell (called here as

method β). To avoid any complications from a decrease in the total cell volume due to continuous electrolyte removal by the SPRDE, we replenish the electrolyte at the same flow rate (f_{pump}) that it is being removed by using a distinct channel from the peristaltic pump (ESI MP2 micro peristaltic pump). In this way we ensure that the overall cell volume is fixed (ca. 60 mL) and that for a fixed f_{pump} (ca. 7.5 $\mu L\, s^{-1}$) we can correlate the area under the corrosion pulse (Equation 1), where I_d is the ion count in arbitrary units (a. u.) and Δt is the time interval in s (where the integration process was applied) with the offset in the background signal measured after the potential pulse is over (I_s).

$$\int_{\Delta t} I_d dt \qquad \text{(Equation 1)}$$

This method does not require pre-calibration of the instrument to know absolute concentrations or any correlation with previous knowledge of the passed electric charge corresponding to dissolution, but it does require that the number of generated ions is large enough to create an offset in the background levels. Note that due to the relatively large cell volume and considering the ICP-MS detection limit of 2 ppt, a minimum concentration corresponding to a fraction of the surface atoms of about one thousandth of a monolayer (ML) can be detected (using an average of 425 $\mu g\, cm^{-2}$ of Pt surface as the mass density of 1 ML[22,56,66]). Therefore, for small amounts of dissolved ions (of the order of $pg\, cm^{-2}$), the increase in background signal is negligible. Both methods (α and β) give equivalent results for N ($< 0.5\%$ difference).

Unlike the rotating ring-disk electrode (RRDE) method[65], where N is independent of rotation speed (ω), both ω and f_{pump} can change N due the hydrodynamic flow balance between electrode drag (either under constant rotation or due to hydrodynamic continuity without rotation) and probe pumping electrolyte out at a fixed flow rate. This can be seen in Figure 5(b), where changes in collection efficiency are observed for a given ω. We note that without any electrode rotation, no reliable hydrodynamic conditions can be established, rendering the N high but with added noise in the concentration measurements. On the other hand, in the presence of continuous rotation, the N decreases continuously for increasing ω, but a steady flow can be achieved. We emphasize that the flow through the pump does not affect the diffusion layer ('Nernst layer') at the electrode surface[65], as it is located further from the typical 'Nernst thickness', which renders the same hydrodynamic properties for the RDE method unaltered[65]. Therefore, we kept the f_{pump} at 7.5 $\mu L\, s^{-1}$ in order to minimize any

delay time from the electrode all the way to the ICP-MS nebulizer system (typically 5.5 s). All experiments shown in this dissertation were taken at a ω of 100 revolutions per minute (r. p. m.), which gives $N = 0.25 \pm 0.02$.

2.2.2.1 Inductively coupled plasma mass spectrometry ($ICP\text{-}MS$) measurements

The electrolyte was pumped out of the electrochemical cell with an ESI MP2 micro peristaltic pump at 7.5 $\mu L\, s^{-1}$ by the probe capillary connected to a polyether-ether-ketone (PEEK) tube (200 µm i. d.), all the way to the ICP-MS inlet system. The ICP-MS inlet is comprised of a Meinhard nebulizer (1.1 liter per minute (Lpm) of argon (Ar) as nebulizing gas) and a cyclonic spray chamber. The f_{pump} was optimized to minimize the transport time between the electrode surface and the ICP-MS detector (delay time ~5.5 s and total internal volume ~42 µL) while preventing bubble formation inside the capillary as observed at higher f_{pump} values. The importance of the delay time just mentioned above may be better understood by the analyzis of the curves presented in Figure 6, where it is shown that by decreasing the delay time, the detection limit for the Pt species can be continuously improved and the dissolution phenomenon itself can be well-correlated with the potential (E) pulse applied (crucial for quick transients). In other words, diminishing the delay time we can come very close to a truly (accurately) stability-structure-activity relationship.

Fresh electrolyte was replenished to the cell at the same f_{pump} to keep the total cell volume (~60 mL) constant. Plasma parameters were set to 1,600 W radio frequency (RF) power, 15.6 Lpm plasma flow rate, and 1.0 Lpm auxiliary gas (Ar). The Pt signal was measured at mass-to-charge ratio (m/z) of 195 atomic mass unit (amu) $^{195}Pt^{+}$with 230 ms dwell time and the $^{40}Ar^{35}Cl^{+}$ (75 amu) dimers generated inside the plasma[67,68] from $HClO_4$ electrolyte were used as internal standards with 20 ms dwell time (total of 0.25 s per replicate), important to achieve higher sensitivities. The intensities were calibrated by immersing the SP in external solutions containing known concentrations of Pt ('mother' Pt standard solution purchased from Sigma-Aldrich®) in the electrolyte of interest (0.1 mol L^{-1} of $HClO_4$) prior to each experiment (a typical calibration curve is shown in Figure 7). An external trigger signal from the potentiostat (Metrohm Autolab® PGSTAT 302N) was set to initiate ICP-MS data collection, ensuring synchronicity between Pt dissolution intensities and electrode potential changes over time (the so-called SPRDE-ICPMS method[38]). So, putting in a perspective that a fundamental electrochemist would appreciate: there are four key

advantages to our SPRDE-ICPMS[38] method as compared to other methods developed in the past. First, it provides almost one order of magnitude higher sensitivity for metal dissolution in comparison with the SFC-ICPMS studies mentioned earlier (e.g., 0.4 pg $cm^{-2}s^{-1}$ in the present work vs. 3 pg $cm^{-2}s^{-1}$in reference [4]). Second, the RDE configuration permits control over mass transport properties at the electrode surface, enabling correlations between the structure-sensitive adsorption of covalently bonded species on well-defined single-crystal surfaces and the stability of surface atoms on those surfaces. Third, the use of well-defined surfaces allows for explorations of the synergetic role of covalent adsorbate-substrate interactions and noncovalent interactions (operating in the double layer region)[69] in guiding the corrosion of metal surface atoms[40,70]. Finally, the SPRDE-ICPMS method enables the in situ measurement of activity-structure-stability relationships — functional links that have never been studied at atomic/molecular levels.

Figure 6. Pt dissolution response towards a potential (E) pulse of 1.2 V for 2 s applied at a Pt(Poly) electrode in 0.1 mol L^{-1} of $HClO_4$ for different transport time (delay time) magnitudes. r_{Pt} = mass dissolution rate.

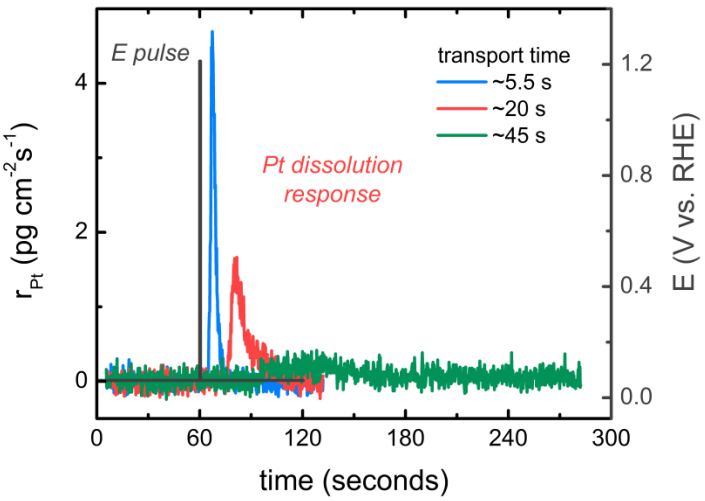

Source: own authorship.

Figure 7. Typical calibration curves obtained for any element measured by SPRDE-ICPMS system. In this case, the curves shown are for $^{195}Pt^{+}$ and $^{40}Ar^{35}Cl^{+}$ ions.

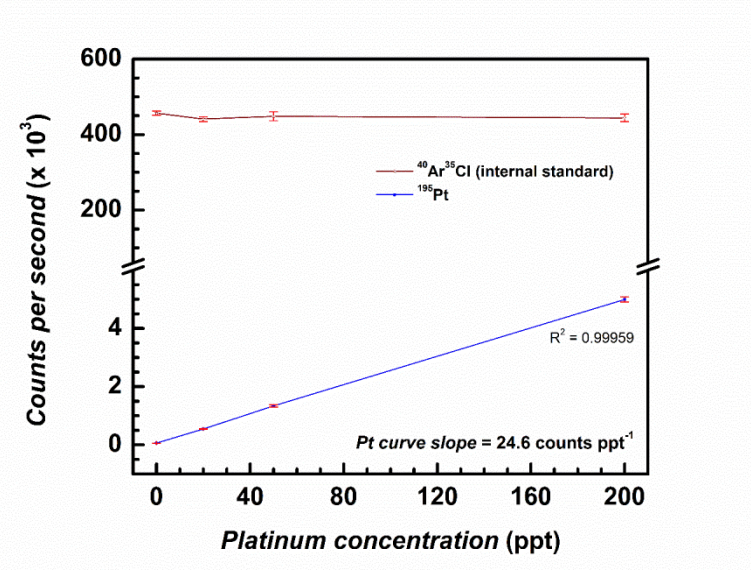

Source: own authorship.

2.2.2 Electrochemical measurements

Electrode preparation and electrochemical measurements were similar to those described in complete detail elsewhere[22,57,64,66]. Briefly, the working electrodes consist of Pt(111) rods of 4 mm in height by 6 mm in diameter (~0.283 cm^{-2} of geometric surface area), which were annealed up to 1,400 K in a mixture of 3% of di-hydrogen diluted in argon (3% H_2/Ar) atmosphere for 10 min After slow cooling for 7 min a drop of ultrapure and deionized water (Milli-Q®) was placed on the crystal surface still in the 3% H_2/Ar atmosphere to further protect it from oxidation and contamination by any organic and/or inorganic molecules diluted in air before its assembly into an RDE system. The final step was the transfer of the RDE system still protected by the water droplet into the electrochemical cell, always immersing the crystal polarized at 0.05 V vs. RDE. All solutions were prepared with ultrapure deionized water to make an 0.1 mol L^{-1} of $HClO_4$ (EMD®, Omnitrace ultra), and purged with Ar (6N0 grade, Airgas) to remove the dissolved O_2. A carbon rod (purity grade of 99.995%, purchased from Alfa Aesar®) was used as counter electrode to avoid any metal contamination. We employed a Ag/AgCl sat. KCl as reference electrode, which was located in an external compartment and connected to the main compartment in the cell through a glass-bridge in order to avoid chlorine ions (Cl^{-}) contamination. However, all potentials noted along this work are given vs. the reversible hydrogen electrode (RHE) by

previously calibrating the $Ag/AgCl\,sat.\,KCl$ reference electrode using the H_2 oxidation/evolution potential obtained in a $Pt(Poly)$ employed as both working and counter electrodes in a separate experiment prior to all electrochemical measurements. We applied ohmic drop ($iR\,drop$) correction to all experiments[71]. To gain insight into the role of anodic and cathodic sweeps on Pt dissolution we performed the so-called asymmetrical cyclic voltammetry, with independent control of the scan rates of both the anodic and cathodic regions. We employed scan rates ranging from $1\ mV\ s^{-1}$ to $500\ V\ s^{-1}$. After the working electrode immersion, a first voltammetric scan was recorded together with the Pt dissolution signal at sweep rate of $50\ mV\ s^{-1}$ to confirm the surface cleanliness. All experiments were performed at room temperature ($\sim 298\ K$) and a ω of $100\ r.p.m.$.

2.2.3 Scanning tunneling microscope (STM) measurements

Scanning tunneling microscopy (STM) images were acquired with a Digital Instrumentations Multi-Mode Dimension STM controlled by a Nanoscope III control station. After the electrochemical experiments, the $Pt(111)$ surface was covered with CO molecules at $0.05\ V$ vs. RHE and then mounted on a microscope head which was then enclosed in an airtight cylinder filled with CO gas at pressure of $1\ atm$. Full experimental description of CO apparatus can be found in references[64,72].

2.3 Results and discussion

2.3.1 Surface speciation and Pt dissolution

We begin by exploring the potential-dependent stability of Pt(111) in 0.1 mol L^{-1} of $HClO_4$ measured by in situ SPRDE-ICPMS. As depicted in Figure 8(A), the SPRDE-ICPMS probe allows for simultaneous monitoring of variations in surface coverage by adsorbates and the dissolution kinetics of Pt surface atoms. In line with previous results[22], the typical cyclic voltammetry (CV) of Pt(111) reveals that the initial adsorption/desorption of hydrogen (historically termed as underpotentially deposited of hydrogen, H_{upd}) from 0.05 up to 0.4 V is followed first by a double-layer region up to 0.55 V, then by reversible adsorption/desorption of hydroxyl species in the so-called "butterfly" potential region (0.55-0.8 V). After the "butterfly" region, the CV profile shows another "double-layer-like" feature from 0.8 to 1.05 V and finally, above 1.05 V, the formation of irreversible oxide that is usually considered to be Pt-O. For the results reported here, the positive potential will be limited to 1.15 V. We note that although the CV of Pt(111) indicates that the surface is nominally "perfect," the representative STM image in Figure 8(B) reveals the presence of a small density of step edges and ad-islands with monoatomic height, confirming our previous suggestion that even Pt(111) contains a small number of defects.

Figure 8. (A) Cyclic voltammetry and corresponding dissolution rate curves for Pt(111) in 0.1 mol L^{-1} of $HClO_4$ at 50 mV s^{-1} at two vertex potentials: 0.95 V (gray) and 1.15 V (blue). Inset curve shows the exponential relationship between the total amount of Pt dissolution and the vertex potential where Pt oxide formation begins (Pt-O_{ad}). (B) Scanning tunneling microscopy (STM) image of the pristine Pt(111) surface, where only small amounts of ad-islands and monoatomic step edges over large terraces are visible.

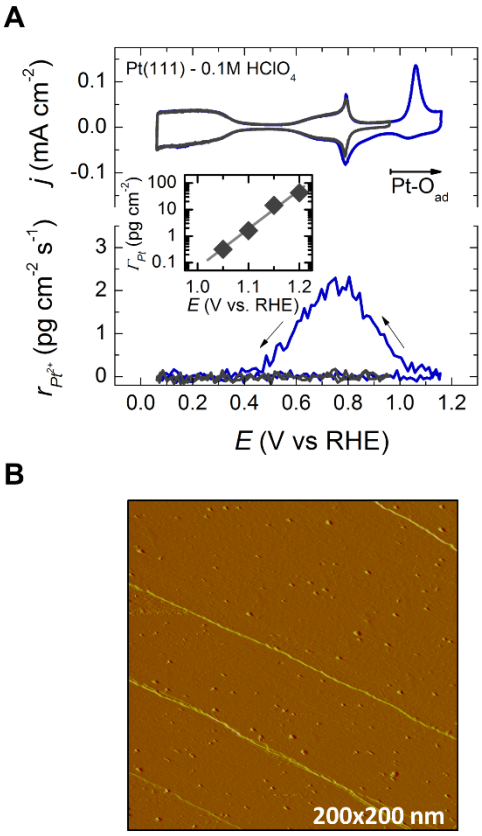

Source: Lopes, P. P. et al. Dynamics of electrochemical Pt dissolution at atomic and molecular levels. J. Electroanal. Chem. 819, 123–129 (2018)[39]. With permission.

The corresponding potential-dependent stability of Pt(111) surface atoms is summarized in the bottom portion of Figure 8(A). Although Pt surface atoms are rather stable in the reversible portion of the CV (e.g., 0.05-0.95 V), irreversible Pt-O_{ad} formation above 1.05 V is accompanied by picogram levels of Pt dissolution (minimum mass dissolution rate, r_{Pt} of ca. 0.2 pg $cm^{-2}s^{-1}$). The stability in the "butterfly" region is not surprising given that the Pt — OH surface interaction involves covalent forces that do not substantially affect the position of surface atoms, as verified by analysis of SXS data[73–76]. On the other hand, the formation of Pt-O bonds that involve a transition from Pt^0 to Pt^{2+} (confirmed by X-ray photoelectron spectroscopy (XPS)[77] and nanobalance experiments[78]) has a strong effect on the stability and roughening of Pt(111), especially after reduction of the oxide. The total amount

of dissolution (Γ_{Pt}) can be quantified as the area under the dissolution rate curve (Equation 2), which is dependent on the amount of oxide that is formed in the irreversible potential region (Q_{ox}). The traditional view of irreversible oxide formation on Pt(Poly) electrodes considers Q_{ox} formation as controlled by the applied electrode potential (E) (and the time (τ) spent in the irreversible potential region. As proposed by Conway-Jerkiewicz and co-authors[27,59,62], this "place-exchange" mechanism has two main features: first, the Q_{ox} vs. E relationship follows an exponential function; and second, the Q_{ox} vs. τ relationship is given by a direct logarithmic rate law[79]. More recently, Feliu and co-authors[54,55] suggested that Pt-O_{ad} formation on Pt(111) surfaces follows a two-dimensional (2D) surface nucleation and growth mechanism, a distinct perspective from the traditional "place-exchange" process. Nonetheless, the fact that the amount of Pt dissolution increases exponentially with increases in the positive vertex potential (inset in Figure 8(a)) signals that there is a direct correlation between Γ_{Pt} and Q_{ox}. The SPRDE-ICPMS data also show that the dissolution rate is always higher during the negative going sweep than during the positive going sweep. In other words, dissolution takes place preferentially during the oxide reduction, a phenomenon that has been noticed before on polycrystalline metal electrodes but did not provide any significant, atomic-level insights beyond simple correlations to the "place-exchange" mechanism[80].

$$\Gamma_{Pt} = \int_0^{\infty} r_{Pt} dt \qquad \text{(Equation 2)}$$

Given that the number of experiments required to fully explore all possible parameters that can control surface stability as a function of Q_{ox}, E and τ is enormous, for our purposes here we utilized a "simple" experimental protocol made it possible to capture the most important transient parameters that may control the stability of metal oxide materials. It is important to note, however, that Pt(111) is the most stable surface due to the hexagonal geometry of surface atoms, and therefore the dissolution rate on other Pt oxide surfaces will be much higher, as discussed by Markovic and co-authors[38]. Nevertheless, to separate the effects of oxide formation on Pt dissolution from those of oxide reduction, we employed a potential-time ramp scheme in which the applied sweep rates on individual anodic (positive sweep direction) and cathodic (negative sweep direction) regions are independent of each other, varying one sweep rate while keeping the other constant. This type of "asymmetric" cyclic voltammetry provides a convenient experimental framework that provides deeper insight into the kinetics of Pt dissolution, as presented below.

2.3.2 The rates of Pt dissolution during anodic scan

Using the asymmetric CV protocol described earlier, we monitored the dissolution of Pt during the positive and negative sweep directions under specific experimental conditions; e.g., oxide formation with varying anodic sweep rates (1 mV s^{-1} up to 50 mV s^{-1}) followed by oxide reduction at a fixed cathodic sweep rate (50 mV s^{-1}), as shown in Figure 9(A). Our main focus here is to explore the Pt dissolution that takes place during the anodic scan, with the varying sweep rates making it possible to explore how the kinetics of oxide formation may affect the rate of Pt dissolution at high electrode potentials. Keeping the scan rate constant in the cathodic sweep direction enabled simultaneous investigations of the impact of oxide formation process on the resulting oxide reduction and concurrent Pt dissolution behavior. We chose the upper potential limit of 1.15 V for two reasons: first, the Pt-O_{ad} formation peak is completed just after 1.15 V (as seen in Figure 8(A)); and second, the total amount of oxide formed at this potential limit is independent of the sweep rate[55]. For the analysis of the results, the data will be presented either as dissolution rates vs. time or vs. potential. As there are no interesting features before 1,000 s for the longest running CV (1 mV s^{-1}), the acquired data will be presented only after this time.

Figure 9. (A) Asymmetric cyclic voltammetry potential-time program and the corresponding Pt dissolution profile for Pt(111) at 0.1 mol L^{-1} of $HClO_4$, where the anodic sweep rate is varied from 1 mV s^{-1} up to 50 mV s^{-1} while keeping the cathodic sweep rate and vertex potential fixed at 50 mV s^{-1} and 1.15 V, respectively. The values for the total amount of dissolution per cycle at each anodic sweep rate are noted for comparison. (B) Equivalent dissolution current vs. potential curve, showing no dependence on scan rate.

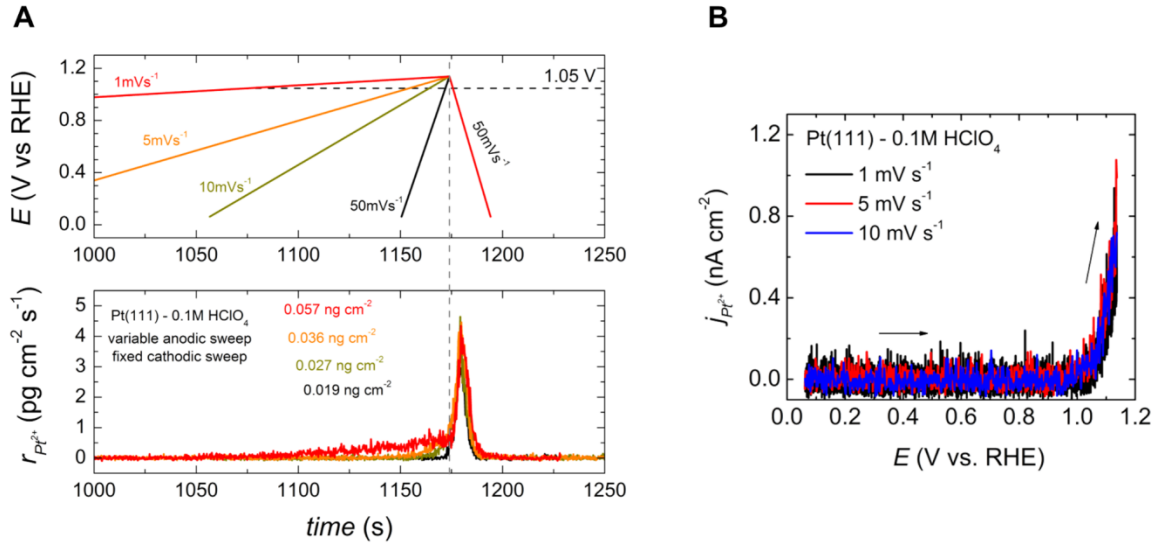

Source: Lopes, P. P. et al. Dynamics of electrochemical Pt dissolution at atomic and molecular levels. J. Electroanal. Chem. 819, 123–129 (2018)[39]. With permission.

As depicted in Figure 9(A), dissolution of Pt starts above 1.05 V in the anodic sweep direction, and we observed low Pt^{2+} dissolution rates (pg cm^{-2} s^{-1} levels) that increase with potential (time) up to the vertex potential. This behavior is observed at scan rates of 1, 5 and 10 mV s^{-1}, but becomes much less resolved at 50 mV s^{-1} because there are only 2 s between the onset of dissolution and the vertex potential at this scan rate. Furthermore, the total amount of Pt^{2+} dissolved during the positive sweep direction is higher for 1 mV s^{-1} than for 50 mV s^{-1}, e.g., Γ_{Pt} increases from 0.002 ng cm^{-2} at 50 mV s^{-1}, which arises mainly from the cathodic portion, to 0.005 ng cm^{-2} at 10 mV s^{-1}, to 0.010 ng cm^{-2} at 5 mV s^{-1}, and finally to 0.038 ng cm^{-2} at 1 mV s^{-1}. It is important to emphasize that this amount of dissolution, expressed as a surface monolayer equivalent (where 1 ML of Pt(111) = 487 ng cm^{-2})[22,66], corresponds to $\leq$ 100 µML. Although this might seem like an

irrelevant amount of Pt in the time frame of one single cycle, this small amount of dissolution will become quite significant over thousands of cycles, ultimately causing cumulative changes to the initial surface structure and morphology related to the kinetics of dissolution.

Figure 9(B) shows the kinetics of dissolution versus potential during anodic polarization for different sweep rates. Note that the mass dissolution rate (r_{Pt}) is converted to an equivalent Pt ion current ($j_{Pt^{2+}}$) via Faraday's law with a generic di-valent ion (X^{2+}). Surprisingly, the dissolution curves acquired for 1, 5 and 10 mV s^{-1} overlap with each other (within experimental error), signaling that the Pt dissolution kinetics are independent of sweep rate. The exponential increase in ion current with electrode potential can be fitted by the Butler-Volmer equation with $\alpha = 0.58 \pm 0.02$[69]. Although the current scale is rather small (ca. 1 nA cm^{-2}), this behavior is similar to that observed for Ag dissolution, for which the rapid electrodissolution kinetics are considered to be a purely faradaic reaction (i.e., independent of sweep rate)[69,81]. In line with Ag dissolution, it is plausible that the anodic dissolution of Pt follows an electrochemical reaction pathway, e.g., $Pt \rightarrow Pt^{2+} + 2e^{-}$. Unlike Ag dissolution, Pt undergoes surface passivation through PtO formation, which affects the rates and quantity of Pt dissolution. We note that the kinetics observed in Figure 9(B) would still follow the same thermodynamic potential as expected from Pourbaix's diagram[9] ($E_0 = 1.2$ V) but differences in the "onset" potential for dissolution might arise due to the local concentration of Pt^{2+} near the electrode surface and kinetic limitations from concomitant oxide formation. Having uncovered the kinetics of anodic Pt dissolution, we turn our attention to the r_{Pt} profile for cathodic dissolution during oxide reduction.

2.3.3 Kinetics of Pt dissolution and re-deposition during the oxide reduction

As expected for the similar Q_{ox} values[55] with the same cathodic sweep rate, the area under the cathodic dissolution peak in Figure 10(A) is similar between all asymmetrical voltammograms, (close to $\sim 0.022 \pm 0.003$ ng cm^{-2}), highlighting that the dissolution of Pt in the cathodic scan is a different process than that during the anodic scan. To further understand cathodic Pt dissolution, we explore how varying the cathodic sweep rate affects the dissolution/re-deposition of Pt during the oxide reduction after an anodic sweep up to 1.15 V at fixed rate (50 mV s^{-1}). Holding the anodic sweep rate fixed while varying the negative sweep rate provides an identical oxide formation step prior to the cathodic sweep, making it possible to independently monitor how the dynamics of oxide reduction impact the dissolution kinetics. For the sake of clarity, we divide the results into slow (1 to 50 mV s^{-1})

and fast (0.05 to 500 V s^{-1}) scan rates (Figure 10(A) and Figure 10(B), respectively). These different conditions reveal the dynamic relationship between the kinetics of oxide reduction and the kinetics of Pt dissolution (Figure 10(C)), as well as how this dynamic relationship impacts the overall amount of Pt loss and consequent Pt re-deposition (Figure 10(D)).

Figure 10. Asymmetric cyclic voltammetry potential-time programs and corresponding Pt dissolution profiles for Pt(111) in 0.1 mol L^{-1} of $HClO_4$, where the cathodic sweep rate is varied (A) from 1 mV s^{-1} up to 50 mV s^{-1} and (B) from 50 mV s^{-1} up to 500 V s^{-1}, while keeping the anodic sweep rate and vertex potential fixed at 50 mV s^{-1} and 1.15 V, respectively. The values for the total amount of dissolution per cycle at each anodic sweep rate are noted for comparison. (C) Equivalent dissolution current versus potential curve, showing that the peak dissolution profile is closely related to the Pt oxide reduction peak and increases at faster scan rates up to 50 mV s^{-1}. (D) Plot of the total amount of Pt dissolution (Γ_{Pt}) vs sweep rate, demonstrating that the cathodic sweep rate controls the total amount of Pt lost per voltammetry cycle.

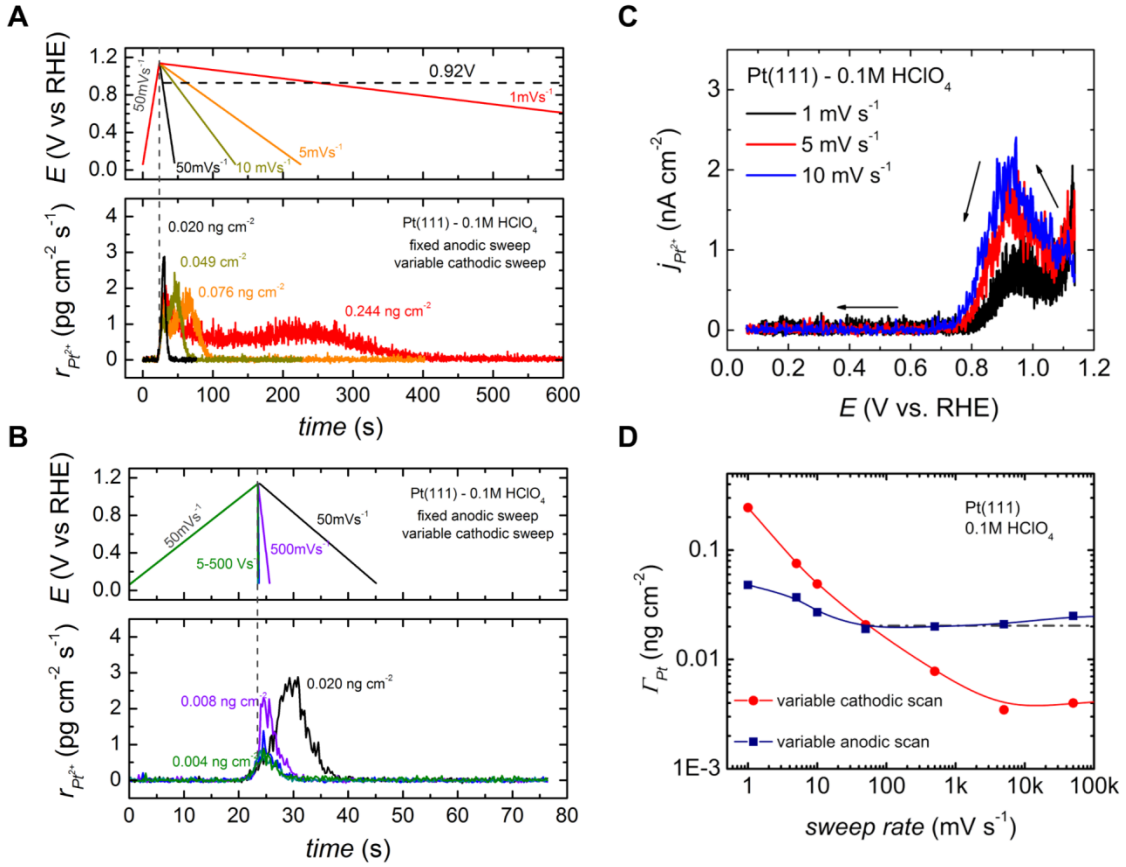

Source: Lopes, P. P. et al. Dynamics of electrochemical Pt dissolution at atomic and molecular levels. J. Electroanal. Chem. 819, 123–129 (2018)[39]. With permission.

As depicted in Figure 10(A), a decrease in the sweep rate from 50 to 1 mV s^{-1} causes two main changes to the overall dissolution profile. First, a dissolution peak is clearly resolved that is closely related to the oxide reduction peak observed in typical CV (Figure 8(A)); and second, the total amount of dissolved Pt changes from 0.020 ng cm^{-2} to

0.244 ng cm^{-2} at 50 and 1 mV s^{-1}, respectively. To further highlight the sweep rate dependence of the dissolution upon oxide reduction we refer to Figure 10(C), where the mass dissolution rate r_{Pt} is converted to an equivalent Pt ion current ($j_{Pt^{2+}}$). Three points are noteworthy: (I) the onset potential for Pt dissolution coincides with that of Pt oxide reduction, which are observed between 1.1 and 0.8 V under these experimental conditions; (II) the kinetics of Pt dissolution are sweep rate-dependent, mimicking the characteristic oxide reduction peak shape with a peak maximum that shifts to more negative potentials at faster sweep rates; and (III) the peak dissolution current also depends on sweep rate, but unlike a typical "pseudo-capacitive" process it does not increase linearly at faster sweep rates. Based on all of these facts, and in contrast to the anodic dissolution of Pt as discussed in the previous section, we propose that the mechanism governing the cathodic dissolution of Pt is a combination of electrochemical reduction of the oxide, e.g.,

$$PtO + 2H^+ + 2e^- \rightarrow Pt^0 + H_2O,$$

and chemical dissolution given by an equilibrium between unstable Pt — O system ($PtO \overset{E}{\rightarrow} PtO^*$) and Pt^{2+} in solution,

$$PtO^* + 2H^+ \rightarrow Pt^{2+} + H_2O.$$

This mechanism provides a functional link between the kinetics of cathodic Pt dissolution and the oxide reduction process. In addition, it is reasonable to anticipate that the concomitant re-deposition of Pt may happen on virgin Pt sites ($Pt^{2+} + 2e^- \rightarrow Pt$), which is a consequence of the simultaneous formation of Pt^0 on the electrode surface and Pt^{2+} in solution at negative potential. The kinetics of re-deposition must be extremely fast given the high overpotential, and the amount of redeposited platinum would strongly depend on the local concentration of Pt^{2+} in the double layer, defined by the balance between the diffusion rate to the bulk and the re-deposition kinetics.

To probe this effect, we employed extremely fast sweep rates in order to prevent Pt^{2+} from diffusing away from the double layer/diffusion layer to the bulk of electrolyte. Under the fastest "sweep rate" (e.g., 500 V s^{-1}, achieved by stepping directly from 1.15 to 0.05 V), the amount of dissolved $_{Pt}$ was found to be extremely low (0.004 ng cm^{-2}), signaling that fast reduction of oxide is followed by equally fast deposition of Pt (Figure 10(B) and Figure

10(D)). A decrease in sweep rate from 500 V s^{-1} to 50 mV s^{-1} leads to an increase in detected Pt^{2+}, supporting our hypothesis that the amount of Pt^{2+} detected during oxide reduction is determined by the kinetics of Pt dissolution and Pt re-deposition, as well as by the transport process of Pt^{2+} from the near-surface region to the bulk of the electrolyte.

To further explore the ability of Pt to re-deposit and change the morphology of the pristine surface, we utilized STM imaging after cycling Pt(111) electrodes (summarized in Figure 11). Three distinct potential-time treatments were utilized to highlight how the dissolution dynamics can tune the morphology evolution: (I) sweeping from 0.05 to 1.15 V, holding the potential for 1,000 s at 1.15 V, and sweeping back to 0.05 V at 50 mV s^{-1} (hereafter termed as sweep-hold-sweep conditions); (II)stepping from 0.05 to 1.15 V, holding the potential for 1,000 s at 1.15 V, and stepping back to 0.05 V (hereafter termed as step-hold-step conditions); and (III) sweeping from 0.05 to 0.6 V, followed by 50 consecutive cycles between 0.6 and 1.15 V, and sweeping back to 0.05 V at 50 mV s^{-1} (hereafter termed as sweep-cycle-sweep conditions). Following the sweep-hold-sweep protocol, the STM image in Figure 11(A) shows the presence of only a few ad-islands deposited on the well-defined terraces and slightly modified step edges. This morphology change may be a consequence of the small dissolution of Pt at anodic conditions, as discussed in Figure 9. On the other hand, by applying the step-hold-step protocol, the STM image is characterized by a high density of Pt ad-islands that are about one atom thick and a few nanometers wide (Figure 11(B)), confirming our hypothesis that fast rates of oxide reduction are indeed followed by equally fast Pt re-deposition, leading to the reduced amount of Pt loss in Figure 10(B) and Figure 10(D). We emphasize that the importance of Pt re-deposition goes beyond simple surface "roughening," as the newly formed ad-islands may create new step edge conditions such as those found in stepped single crystals, with $(111) \times (111)$ or $(111) \times (100)$ types of "defects"[22,82,83]. In order to understand the impact of Pt dissolution/re-deposition under more "realistic" conditions, the sweep-cycle-sweep protocol was used to mimic the pre-conditioning of Pt catalysts before the ORR studies in fuel cells[66]. As depicted in Figure 11(C), extensive oxide formation-reduction cycles lead not only to the formation of ad-islands, but also to substantial damage to the Pt surface, which is seen as single-atom-deep pits present on the (1×1) terraces. There are many forces that could lead to pit formation, including the cumulative damage to ad-islands formed at each reduction cycle and their surrounding terrace atoms, and/or volume-/strain-induced morphological changes due to differences in the atomic radius of Pt^0 (139 pm)[84] and the ionic radius of Pt^{2+} (84 pm,

average of distinct coordination environments)[85]. A detailed understanding of such potential-dependent kinetic and morphological changes is not yet at hand; however, the observation of markedly different variations between the thermodynamics and kinetics of Pt dissolution under different rates of oxide formation and reduction are quite intriguing in their own right. Further use of in situ SPRDE-ICPMS method to probe the kinetics of such processes at other single-crystal surfaces stands at a fascinating juncture and may provide further insights into the dynamics of surface restructuring[28].

Figure 11. Scanning tunneling microscopy (STM) images showing changes to surface morphology at atomic level depending on different potential-time programs. (A) Surface morphology changes after the mild dissolution of step edges the sweep-hold-sweep protocol. (B) Surface morphology with a high density of ad-islands because of instantaneous potential steps in the step-hold-step protocol. (C) Highly "roughened" surface due to multiple cycles in the sweep-cycle-sweep protocol, showing not only step edge damage and ad-island formation but also pit formation on terraces as the result of dissolution upon oxide reduction.

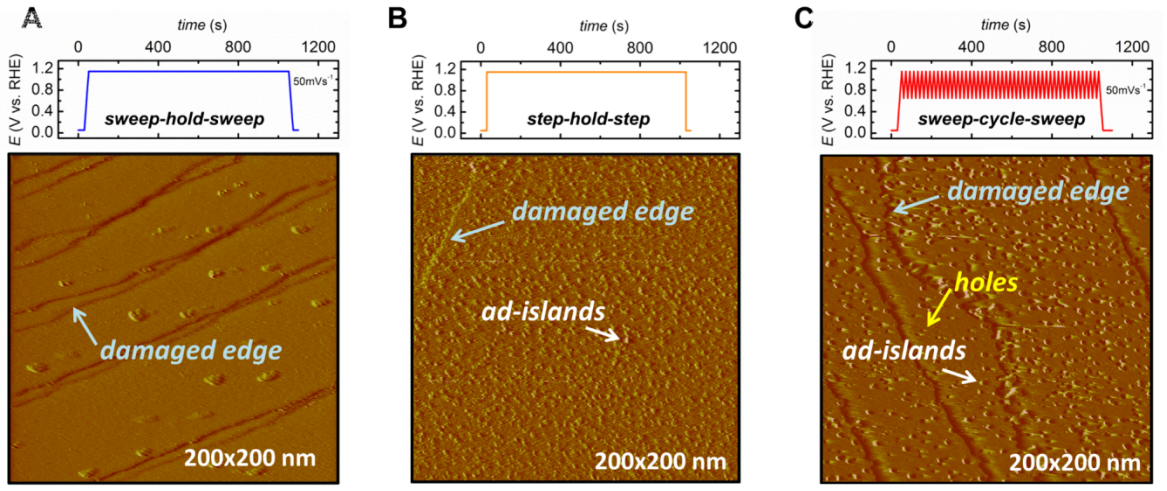

Source: Lopes, P. P. et al. Dynamics of electrochemical Pt dissolution at atomic and molecular levels. J. Electroanal. Chem. 819, 123–129 (2018)[39]. With permission.

2.4 Conclusions

Here, we have demonstrated that it is possible to uncover the relationships between Pt dissolution and Pt oxide formation/reduction through systematic investigations of the underlying reaction kinetics. The dissolution dynamics were shown to correspond to changes in atomic-level surface morphology, providing a firm basis for understanding how the degradation of well-defined surfaces may ultimately define how nanoparticle systems will be affected by advanced degradation test (ADT) protocols. Indeed, current ADT protocols briefly dwell in the oxide formation and reduction region, which will induce the dissolution of the Pt surface to some extent. As anticipated from our results, coupled with the fact that ADTs use fast cycling, the overall response will be to promote more dissolution and re-deposition than simple removal of surface layers. Thus, it is not surprising that the most commonly observed nanoparticle degradation mechanism is particle size growth, resulting in a loss of surface area[86–90]. Given the insights into Pt dissolution and re-deposition processes outlined above, it is likely that all mechanisms of particle coarsening, growth and dissolution are, in fact, caused by the same underlying process —Pt dissolution during both the anodic and cathodic scans coupled with Pt re-deposition under cathodic conditions. As a result, it should be possible to control the morphological evolution of nanoparticle materials via the careful control of potential, time and the amount of irreversible oxide formed. Finally, our results reinforce the idea that using Pt as a counter electrode must be done with extreme caution, especially if the intent is to explore non-Pt-group-metal (non-PGM) materials for electrocatalysis where Pt is already a highly active electrocatalyst.

CHAPTER 3

IN SITU QUANTIFICATION OF SULFUR DISSOLUTION USING THE SPRDE-ICPMS METHOD AND ITS EXPERIMENTAL APPLICATION TO SIMULTANEOUSLY MONITOR THE ACTIVITY AND STABILITY OF CRYSTALLINE MoS_2 AND AMORPHOUS MoS_x TOWARDS HYDROGEN EVOLUTION REACTION IN ACIDIC ENVIRONMENT

3 In situ quantification of sulfur dissolution using the SPRDE-ICPMS method and its experimental application to simultaneously monitor the activity and stability of crystalline MoS_2 and amorphous MoS_x towards hydrogen evolution reaction in acidic environment

This chapter is composed by experiments that are currently being prepared for publishing. Briefly, we studied the use of molybdenum-disulfide-based materials as electrocatalysts for the hydrogen evolution reaction (HER) in acidic environments. Both activity and stability towards HER were simultaneously monitored by the SPRDE-ICPMS method previously described (please refer to Chapter 2).

3.1 Introduction

A considerable share of humanity has been trying to convince us that some facts and issues (eg., the Earth is round and continuously getting warmer) experimentally proved by the scientific community are just myths and/or conspiracy theories. It is intriguing to still believe that the Earth is flat considering that the knowledge regarding the spherical Earth dates back to the sixth century BC by the Greek philosophy[91]. Luckily, most of humans have already watched a ship sail off to sea or the beauty of sunset, which give us simple but unquestionable evidence that the Earth has a spheroidal shape. A considerable raise in the global warming rate process, however, was first evidenced in the 1950s, due to the large greenhouse gases (eg., CO_2, N_2O, CH_4, etc.) emission by the modern society (the so-called greenhouse effect (GHE))[92,93]. Regardless of the infancy status of the GHE evidence if compared to the Earth's shape evidences above mentioned, we cannot be misguided by non-scientific speculations[94]. Indeed, comparing the total CO_2 emission (TCE) from energy consumption from 1950 to 2011 (Figure 12), we observe that by 1995 the TCE had already doubled[95,96]. The total world population (TWP) was also at the same pace, being doubled in that 45 years period[97]. It was then clear that something has to be done to slow the $\overline{TCE}$ and, consequently, the GHE. Several nations started to adopt alternative energy sources (AESs) that can generate small to zero amounts of CO_2. Although solar and windy sources (Figure 13) may never be considered as primary energy sources for society[98], they are convenient candidates as AESs. However, due to their 'seasonal' characteristics, they must be readily captured, converted and either promptly used (eg., applying the electricity produced to power electric-machines) or stored (eg., applying the electricity to produce fuels)[98–107]. The solar

energy source, particularly, extensively used for carbon-neutral fuel production, where the electric power generated by photovoltaic cells is subsequently used to electrochemically convert H_2O to H_2 in electrolyzers. In turn, the H_2 produced may be used to power fuel cells. Fortunately, this kind of approach has already started to show improved results regarding the carbon emissions, where the TCE/TWP ratio is 20% smaller in 2011 compared to 1950 (Figure 12)[95,96]. Nevertheless, the continuous improvement of the energy-converters efficiency is mandatory to accelerate the process for the upmost goal: reduce the global warming rate[92,93,98].

Figure 12. Carbon dioxide (CO_2) emissions from energy consumption by source (total) from 1949 to 2011.

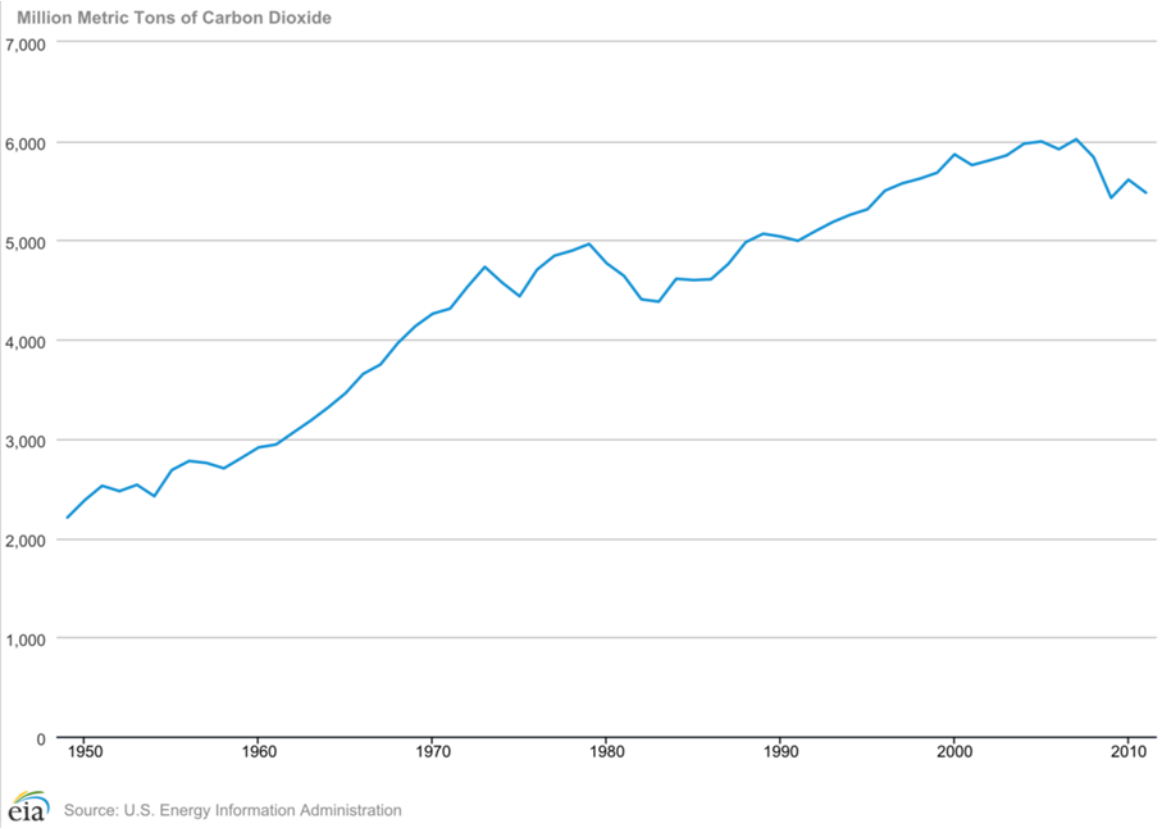

Source: adapted from U.S. Energy Information Administration (EIA)[95,96,108].

Figure 13. Share of non-fossil electricity generation by source from 1990 to 2016.

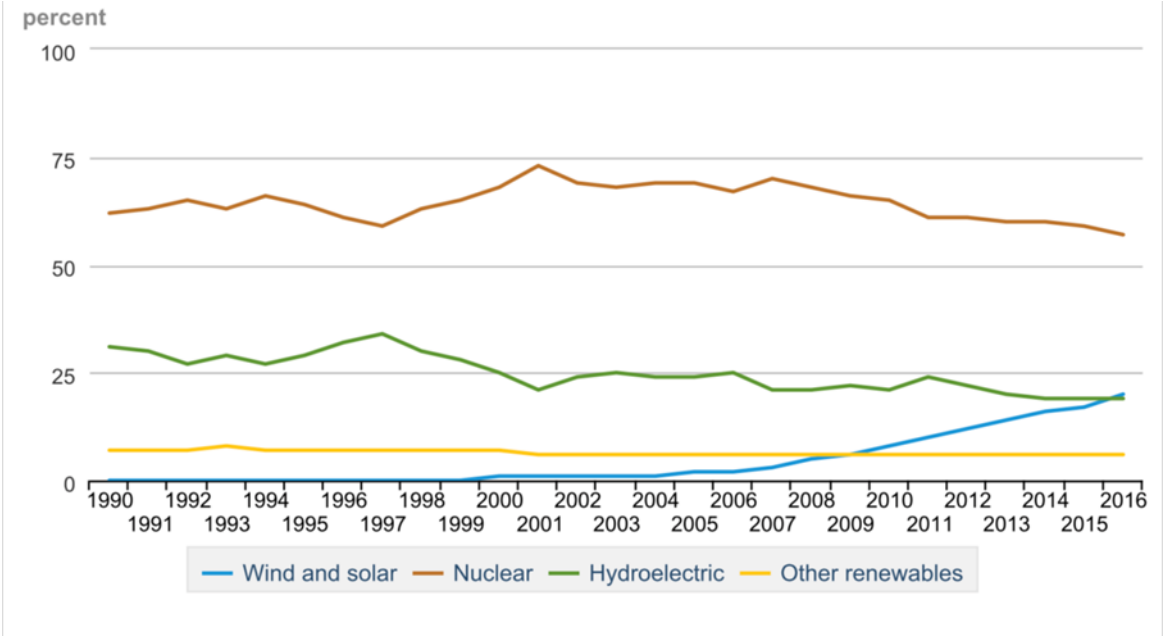

Source: adapted from U.S. Energy Information Administration (EIA)[95,96].

To be considered an applicable alternative energy converter (AEC), its cost-price has to be at least comparable to the typical fossil-fuel energy converters. For instance, polymer electrolyte membrane fuel cells (PEMFCs) have being continuously implemented as an AEC for transportation due to their ability to power vehicles (fuel cell vehicles, FCVs) with zero carbon-emissions (water and heat as final products) and their potential for high efficiency (Figure 14). In fact, a typical PEMFC used today in vehicles are two to three times more efficient than an internal combustion engine running on gasoline. However, to reach this level of efficiency, expensive materials like platinum and highly-pure hydrogen gas (H_2) have to be used. Indeed, due to factors like high-cost, the number of FCVs keep oscillating from year to year (Figure 14). Contrary to the cheap H_2 derived from the well-known steam reforming from hydrocarbons[109–111], which inevitably contain other gases as impurities (resulting in decreased-performance due to catalyst-poisoning[112,113]) and also contribute to the global warming, the clean H_2 derived from the electrolysis of water is still very expensive because of its high electric power and expensive material requirements. For instance, even if one uses the solar energy to power a water electrolyzer, which would keep a CO_2-free system (Figure 15), the whole energy conversion process (i.e., from the sun energy to the vehicle locomotion) would still be more expensive than the fossil fuel-based system.

Figure 14. Number of fuel cell vehicles (FCVs) and fuel consumption from 2003 to 2016.

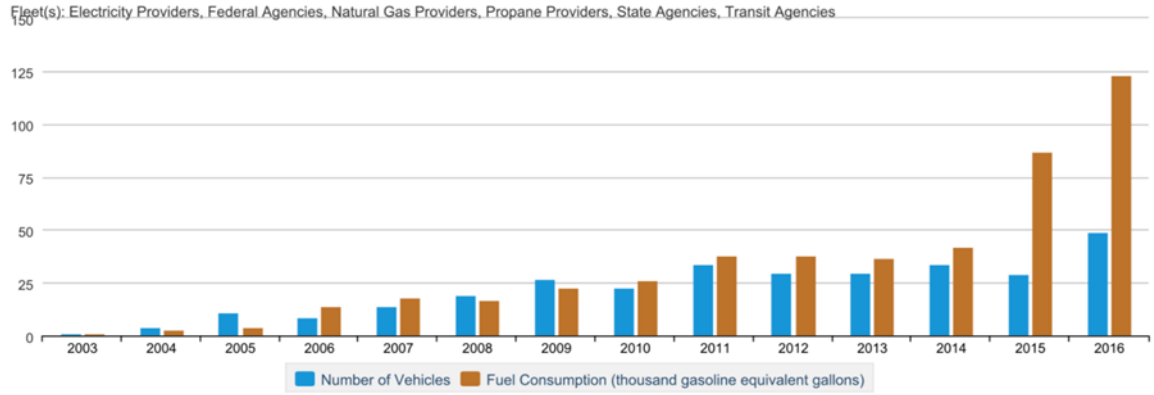

Source: adapted from U.S. Energy Information Administration (EIA)[95,114].

Figure 15. H_2 and O_2 are combined in a proton electrolyte membrane fuel cell (PEMFC) to generate a flow of electrons and protons across an external circuit and a polymeric membrane, respectively, producing electrical energy. The solar fuel cell uses light to run the electron and proton flow in reverse. Coupling the electrons and protons to catalysts breaks the bonds of water and makes the bonds H_2 and O_2 to effect solar fuel production. cat and PV stand for catalyst and photovoltaic, respectively.

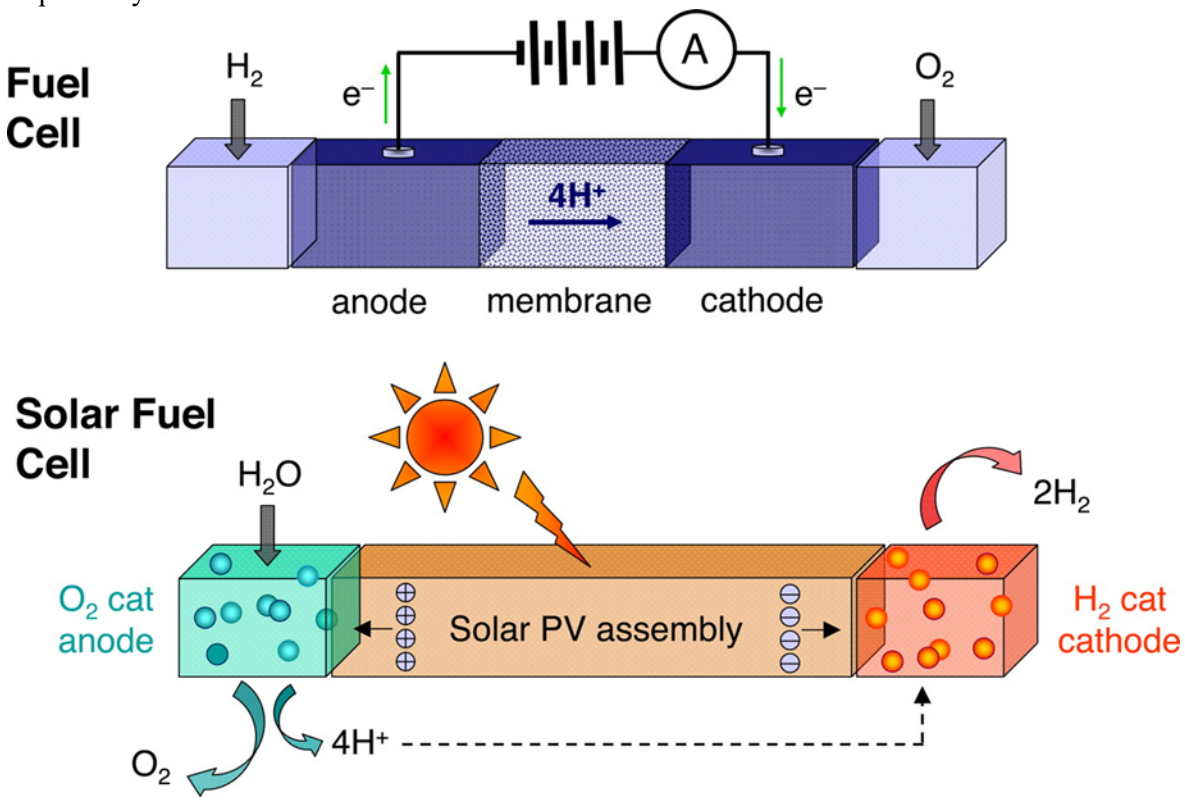

Source: reproduced from Lewis, N. S. & Nocera, D. G. Powering the planet: Chemical challenges in solar energy utilization. Proc. Natl. Acad. Sci. 103, 15729 LP-15735 (2006)[98]. With permission.

The common and determinant factor in the processes described above is the catalytic efficiency. By producing better catalysts, one would accomplish all the energy conversion

steps more efficiently and, therefore, at low cost. So, what makes a good catalyst? Two main pre-requisites are: high activity and stability. It is well known that platinum is a high-active and stable electrocatalyst for hydrogen oxidation and reduction (evolution) reactions. In fact, when in contact with H_2 (pressure at 1 bar) and H^+ (ion activity of 1), the $Pt\,|\,H_2, H^+$ interface was chosen as the main reference electrode (namely standard hydrogen electrode, SHE) in the standard potential table in thermodynamics due to its ideally non-polarizable behavior[65,69]. Unfortunately, Pt is a very expensive material. Therefore, as an alternative, one should either diminish the Pt content without losing the overall activity-stability or find cheaper materials with close or better catalytic activities and stabilities as the typical Pt-based electrodes.

3.1.1 Molybdenum disulfide (MoS_2) nanoparticles for hydrogen evolution reaction (HER) in acidic environment

When trying to find alternatives to 'classical' (electro)catalysts for any type of (electro)chemical reaction, one smart first option is learning and relying on nature's highly evolved way (although physical-chemically complex) to speed (electro)chemical reactions: enzymes[98,100,101,103,105–107,115]. Hydrogenases are known as very effective catalysts for the hydrogen evolution reaction (HER) in bio-systems[116–121]. Thanks to thousands of years of evolution, enzymes 'perfected' the way towards "affordable" HER by means of only non-noble metals (Mo, Fe, Ni, etc.) and non-metals (S, N, C, O, etc.) in their chemical composition[116,119,122,123]. Based on this nature's example, researchers have been trying to find an applicable inorganic analogue to ultimately substitute the expensive Pt-based electrocatalysts. Surprisingly, a chalcogenide compound (molybdenum disulfide, MoS_2) long used as a dry-lubricant[124,125], and as a catalyst in the petroleum industry for removing sulfur from natural gas and refined petroleum products, a process called hydrodesulfurization (HDS)[126–135], was found to be a good candidate to promote HER in acidic-aqueous electrolyzers[136]. The immediately question risen was: what is(are) the active-site(s) for the hydrogen formation? In 2007, Chorkendorff and co-authors[137] identified the edge sites of nanoparticulate MoS_2 crystals as active for HER in H_2SO_4 electrolyte (pH 0.24 at a temperature of 296 K). The dominant nature of edges' structure is comprised by sulfided-Mo-edge, regardless of the MoS_2 nanoparticle size. These observations are corroborated by previous density functional theory (DFT) results, in which the sulfide $(10\bar{1}0)$ Mo-edge was predicted to be the active site for HER[136]. However, these

conclusions were solely based on nanoparticles composed by flat polygons of S-Mo-S tri-layers. Depending on the synthetic conditions, these tri-layers can be stacked to form a graphite-like structure the same way as graphene-sheets[138–144]. As will be discussed below, the more general class of layered transition metal dichalcogenides (TMDCs), in which MoS_2 is one example, may have completely different chemical and electronic properties depending on their structural conformation and the number of "single"-tri-layers (hereafter called just by single-layer) forming the stacked-crystal.

3.1.2 Very brief description of the chemistry and electronics of molybdenum disulfide (MoS_2) - a transition metal dichalcogenide (TMDC) - and speculations regarding the nature of the electrocatalytic active-site(s)

The transition metal dichalcogenides (TMDCs) chemistry and electronics are extremely versatile[145–148]. Figure 16(A) shows the three-dimensional scheme for a typical TMDC. The crystal structure of the TMDCs can assume three main polymorphs (Figure 16(B)), which are composed of individual and/or stacked single-layers (X-M-X, Xstands for chalcogens (S, Se and Te) and M stands for transition metals (Mo, W, Nb, etc.)), namely 1T, 2H and 3R (1, 2 and 3 indicate the number of singlet-layers X-M-X units forming the unit cell, and T, Hand R stand for trigonal, hexagonal and rhombohedral, respectively), and these polymorphs can be stacked in different arrangements depending on their synthesis conditions. Molybdenum disulfide (MoS_2), is commonly found in nature in the 2H structure (with stacking sequence of S-Mo-S — Mo-S-Mo)[145]. The 2H-like structure has a semiconducting character, with its bandgap value varying from 1.8 to 1.2 eV when changed from single-layered to multi-layered composition[149,150]. As mentioned in the Section 3.1.1, Chorkendorff and co-authors[137] showed experimentally that the edge-sites in the single-layer MoS_2 nanoparticles are composed by sulfide-Mo-edge in this 2H-like structure. However, Jin and co-authors[151] were able to isolate MoS_2 sheets composed of 1T-like structure (a metastable phase of MoS_2[145], which has a metallic character[151], by the chemical exfoliation method. Both structural and electrochemical findings confirmed the increased electrode kinetics and the high yield in electrical transport assigned to the metallic nature of 1T-like polymorph. The authors claim that this 'new' metallic MoS_2 polymorph possess a high and spread number of catalytic active-sites, which together to its metallic conductivity provide a better electrocatalyst for HER in acidic media then 2H-like MoS_2 nanoparticles[137,152]. Therefore, even though these materials demonstrate good performance for HER, almost approaching performance that of Pt[151,153], the true nature of the active sites is still open to

debate, specially to which extent Mo and S sites are involved in the transition-state for H_2 formation[136,137,154–158].

Figure 16. (A) Ball-stick representation scheme of a typical transition metal dichalcogenide (TMDC) of MX_2 structure, where M and X stands for the transition metal (in black) and the chalcogenide (in yellow), respectively. (B) Schematics of the structural polymorphs: 2H (hexagonal symmetry, two layers per repeat unit, trigonal prismatic coordination), 3R (rhombohedral symmetry, three layers per repeat unit, trigonal prismatic coordination) and 1T (tetragonal symmetry, one layer per repeat unit, octahedral coordination). The chalcogen atoms (X) are yellow and the metal atoms (M) are grey. The lattice constants a are in the range 3.1 to 3.7 Å for different materials[159]. The stacking index c indicates the number of layers in each stacking order, and the interlayer spacing is ~6.5 Å.

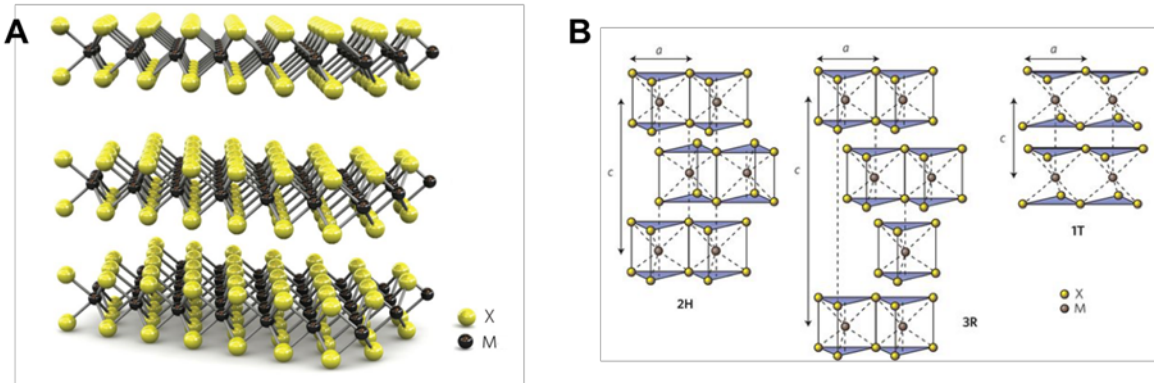

Sources: (A) and (B) adapted from Radisavljevic, B., Radenovic, A., Brivio, J., Giacometti, V. & Kis, A. Single-layer MoS2 transistors. Nat. Nanotechnol. 6, 147 (2011)[148] and Wang, Q. H., Kalantar-Zadeh, K., Kis, A., Coleman, J. N. & Strano, M. S. Electronics and optoelectronics of two-dimensional transition metal dichalcogenides. Nat. Nanotechnol. 7, 699 (2012)[147], respectively. With permission.

3.1.3 Amorphous molybdenum disulfide (MoS_x) and its related-moieties as hydrogen evolution reaction (HER) catalysts

The quest for identification of the true nature of active-site(s) for $\overline{HER}$ in well-ordered surfaces (stable-2H and metastable-1T polymorphs) of MoS_2 crystals is proved to not be an easy business in electrocatalysis (please refer to Section 3.1.2). When dealing with completely random surface-compositions in Mo_xS_y-amorphous and/or moieties structures, asserting possible electrocatalytic active-site(s) sounds impractical. Nevertheless, it was found that these non-crystalline molybdenum sulfides are very active towards HER[160]. For instance, at a MoS_x mass loading of 0.2 mg cm^{-2}, Hu and Vrubel[161] measured a current density of 10 mA cm^{-2} at -0.16 V vs. RHE in pH 0. The authors suggested that regardless of the different electrochemical deposition methods employed for the syntheses of the amorphous MoS_x catalysts, all surfaces present the same activity-sites, which were attributed to the MoS_{2+x} species.

It is a fact, as already mentioned in Section 1.2, that the knowledge of the structure-activity relationships may guide us to a rational design of even more electrocatalytic-active surfaces. The works above cited (Sections 3.1.1, 3.1.2 and 3.1.3) focus mainly on these relationships; although stability tests (both in transient and/or steady-state regimes)[162–168] have been performed, little to no knowledge is well-stablished at atomic-level. Some catalysts show good electrochemical stability[162], others are deactivated just after a few excursion-cycles towards HER[169]. What structural-chemical features guarantee good stability? Furthermore, what are the factors impeding MoS_2 and MoS_x-based materials to be stable during HER? We think that due the vast chemical and electronic versatility of TMDCs (crystalline- MoS_2 and amorphous- MoS_x), finding common descriptors that govern the structure-stability relationships may guide future studies towards a rational tailoring of both durable and active Pt-free electrocatalysts. Finally, it is rather puzzling that these materials are considered highly stable[162–165,167,168], despite the fact that dissolution of Mo species to the electrolyte is a ubiquitous process and would eventually lead to catalyst degradation after many cycles[170]. Moreover, it is unclear what is the stability of sulfur atoms, which are known to form H_2S species in acidic environments, an issue not yet discussed but that may present a profound impact on our understanding of TMDCs catalysts for the HER.

Herein, we present evidence for active site deactivation and regeneration processes that are operational on Mo-based chalcogenides (e.g., MoS_2) and chalcogels (e.g., MoS_x) materials. First, by monitoring the in situ dissolution rates of both Mo and S atoms together with HER activity we were able to establish their unique dissolution dynamics in acid-media as a function of the electrode potential. Surprisingly, we found a selective S atom loss with minimal Mo dissolution during HER, whilst at mild positive potentials Mo dissolution happens with minimum S loss. We propose that the selective sulfur release concomitant to H_2 production arise from its interaction to hydronium ions (H^+) and its thermodynamic driving force to form H_2S, while the Mo-S interaction is weakened as part of the HER catalytic cycle at more negative electrode potentials. As a consequence, we found that the selective removal of S leads to Mo-S active site conversion to Mo-O_x species formed by "free" Mo^{n+} that interacts with surrounding H_2O and H^+, creating new surface sites that are less active for hydrogen production (e.g., deactivation). In turn, we also found that this newly Mo-O_x species can be selectively removed from the catalyst surface, giving way for the selective Mo dissolution observed at higher electrode potentials, effectively cleaning the surface and exposing fresh Mo-S sites for the efficient hydrogen production (e.g., regeneration). Finally, our results demonstrate that electrochemical interfaces are constantly evolving, and that

understanding the underlying kinetic processes is necessary to successfully design dynamic interfaces that can remain active after extensive electrocatalysis excursions.

3.2 Experimental procedures

3.2.1 Electrochemical experiments and in situ inductively coupled plasma mass spectrometry (ICP-MS) analysis

All electrochemical measurements were performed with a potentiostat (Methron Autolab® PGSTAT 302N), and a standard three-electrode electrochemical cell coupled with inductively coupled plasma mass spectrometry (ICP-MS) by a stationary probe rotating disk electrode (SPRDE), as previously described in Section 2.2. Briefly, Mo and S dissolution rates were simultaneously measured in the ICP-MS while the working electrode was controlled by a potentiostat. This allowed us to measure the dissolution profile together with the electrochemical activity during the HER (negative potentials) and typical CV (positive potentials). All dissolution profiles were calibrated using Mo and S standards (Ultra Trace Select, Fluka®) measured previously to any electrochemical experiments. The working electrodes were prepared by first dispersing each electrocatalyst in dimethylformamide (DMF) solution to the final concentration of $\sim 566\ \mu g\ mL^{-1}$.

All the electrocatalyst material preparation was performed in a glove box to avoid any contamination by O_2. The materials studied in this work were: MoS_2 nano-flakes (2D Materials ©), MoS_x (kindly supplied by Kanatzidis's research group; please see reference [171] for syntheses procedure), MoO_2 and MoO_3 (Aldrich®). A 15 µL aliquot of the as-prepared dispersion was deposited in a clean-mirror-like glassy carbon rod already inserted in the RDE setup and allowed to dry completely in air-free atmosphere. The electrode was transferred to the anti-chamber by the glove box and an aliquot of 15 µL of Nafion® solution (0.05% in a water/isopropanol solution ($v{:}v = 1{:}1$)) was deposited over the as-prepared catalyst surface. The electrode was dried under vacuum and immediately protected with a drop of water before being transferred to the electrochemical cell under potential control (0.05 V vs. RHE). A high-purity graphite rod was used as a counter-electrode to prevent any cross-contamination of metals in the working electrode, and an $Ag/AgCl$ sat. KCl was used as a reference electrode. All potentials described in this work were converted to RHE, determined by a separated experiment (please refer to Section 2.2 for more details). The electrolyte used was $0.1\ mol\ L^{-1}$ of $HClO_4$ solution prepared using ultra-clean deionized water (Milli-Q® system) and high purity $HClO_4$ (EMD, Omnitrace ultra). The potential sweep rate applied for all voltammetry and polarization curves was $50\ mV\ s^{-1}$. Chrono-amperometry experiments were performed by applying the potentials steps to the desired potentials values. The electrode was rotated at $100\ r.p.m.$ during all

electrochemical experiments as this is the optimized rotation rate for high collection efficiency by the SPRDE for ICP-MS measurements (see details in Section 2.1).

3.2.2 Characterization by X-ray photoelectron spectroscopy (XPS)

The X-ray photoelectron spectroscopy (XPS) measurements were performed using a Thermo Scientific ESCALAB 250 Xi spectrometer equipped with a monochromatic Al K_α X-ray source (1,486.6 eV) and operated at 300 W. All samples were analyzed under vacuum (pressure $< 10^{-8}$ mbar), whereas survey scans and high-resolution scans were collected using pass energies of 50 and 25 eV, respectively. Binding energies were referred to the C 1s binding energy at 284.6 eV. All XPS studies were performed at 294 K, using an 45° take-off angle. Also, a low-energy electron flood gun was employed for charge neutralization. The XPS measurements were performed before and after the electrochemical studies, were the electrocatalysts deposited onto a glassy carbon rod by the drop-casting method mentioned above (Section 3.2.1), seated on a copper foil and subsequently put into the entry-load chamber to pump.

3.3 Results and discussion

3.3.1 Selective dissolution of sulfur during hydrogen evolution reaction (HER)

The hydrogen evolution reaction (HER) in acid-media is proposed to follow three main reaction steps: (I) first, a hydronium discharge occurs in the so-called Volmer step ($H_3O^+ + e^- \rightleftharpoons M\text{-}H_{ad} + H_2O$), followed by either the (II) Heyrovsky step, that requires both H_{ad} and H_3O^+ for the H_2 formation ($H_3O^+ + e^- + M\text{-}H_{ad} \rightleftharpoons H_2 + M + H_2O$), or the (III) Tafel step, which is the simple recombination of two neighboring H_{ad} species to make the H-H bond and leave the surface as H_2 molecules ($2M\text{-}H_{ad} \rightleftharpoons H_2 + 2M$)[65,69]. While a rigorous kinetic analysis of the HER requires knowledge of the true number of active sites[137], and electronic conductivity of the electrode material[147], we shall focus our analysis to the trends obtained simultaneously between activity and stability. Thus, we begin by exploring the electrochemical dynamics of two classes of Mo-S_x materials in 0.1 mol L^{-1} of $HClO_4$ electrolyte as a function of electrode potential. We purposely choose both MoS_2-crystalline chalcogenide and MoS_x ($x \approx 6$)-amorphous[171] chalcogel for two main reasons: first, while only a limited number of edge sites are available for catalysis in the crystalline material[137,158], the molecular structure of amorphous chalcogel provides a much higher active surface area for the HER to take place[160]. Second, the difference in chemical composition and chemical oxidation states between both materials gives us the opportunity to evaluate how the chemical properties correlate to observed electrochemical dynamics. This can be seen in Figure 17(A), where XPS analysis reveals that in the crystalline-MoS_2 Mo and S atoms are entirely present as Mo^{4+} and S^{2-}, respectively. However, XPS results for the amorphous chalcogel shown in Figure 17(B) reveals that the Mo sites are mainly composed of 4+ oxidation state, containing a mixture of Mo-S and to a minor extent Mo-O bonds, with S speciation comprised of both sulfide (S^{2-}) and poly-sulfide (S_2^{2-}) moieties. Overall then, the differences in chemical speciation between both materials will provide an important framework for establishing activity-stability relationships, as discussed next.

Figure 17. X-ray photoelectron spectroscopy (XPS) spectra for Mo and S species present in the carbon supported (A) MoS_2(crystalline) and (B) MoS_x(amorphous) prior any electrochemical procedure. Hydrogen evolution reaction (HER) cyclic voltammetry (CV) and corresponding dissolution rate curves for (C) MoS_2(crystalline) and (D) MoS_x(amorphous) in 0.1 mol L^{-1} of $HClO_4$ at 50 mV s^{-1} with a rotation rate of 100 r. p. m.. The potential interval where different in order to reach a close amount of current density due to different HER catalysis performance for each material. Anyway, the start potential was 0.05 V vs. RHE for both materials. The black arrows are present just to indicate the direction of the potential cycling.

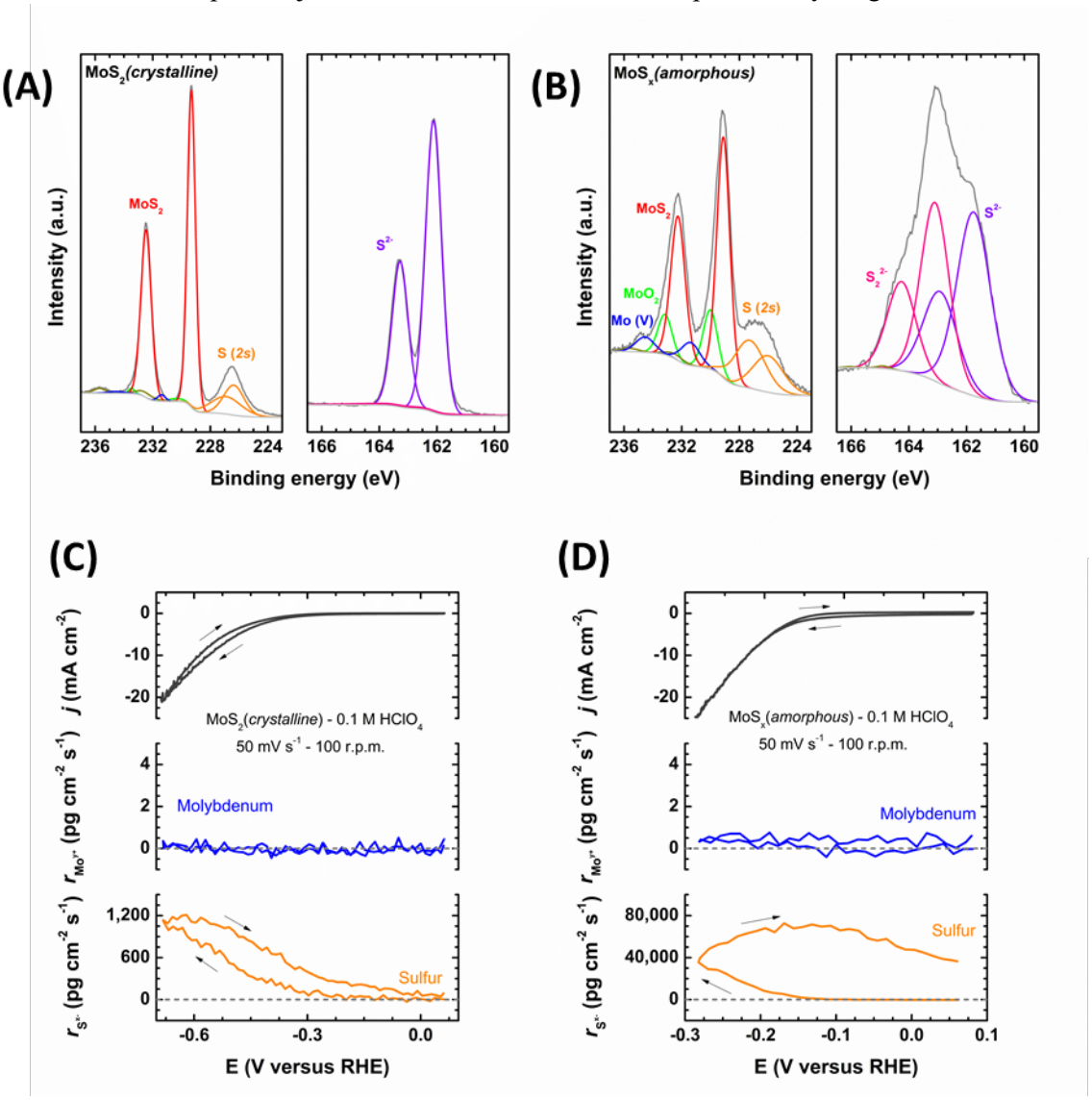

Source: own authorship.

To establish activity-stability relationships we utilize the SPRDE connected to an ICP-MS[38], which allows determining the HER activity by measuring the electrochemical current and the materials stability by measuring dissolution rates from both Mo and S with the ICP-MS, all together while varying the electrode potential values with respect to the reference electrode, e.g., the RHE (see experimental procedures in Section 3.2 for further

details). Figure 17(C) shows the typical HER polarization profile for MoS_2, reaching about 20 mA cm^{-2} at -0.7 V (top panel), with the respective dissolution rates for Mo (middle panel) and for S (bottom panel) showing a rather surprising profile. On one hand, the dissolution of Mo is negligible, with the rates hovering around zero throughout the entire potential scan. However, sulfur dissolution rates show a profile resembling that of the HER polarization curve, with an increase in dissolution at more negative potentials that reaches a maximum dissolution rate of ca. 1.2 ng cm^{-2} s^{-1} at -0.7 V. It is noteworthy to mention that such dissolution process is not continuous, but higher dissolution rates are observed only in the first voltammetric cycles, which decays after multiple scans into the HER (see Figure 18(A) and Figure 18(B)). Also, it is important to emphasize that this "selective-sulfur-loss" concomitant to H_2 production has never been shown before (to our knowledge), that could only be revealed with the help of experimental methods such as the SPRDE-ICPMS that can probe in situ kinetics of dissolution processes of both metal and non-metal species of active electrocatalysts.

Figure 18. Consecutive hydrogen evolution curves followed by the dissolution processes of Mo and S for (A) MoS_2(crystalline) and (B) MoS_x(amorphous) in 0.1 mol L^{-1} of $HClO_4$ at Ar atmosphere, with 50 mV s^{-1} scan rate and 100 r. p. m. rotation rate. It is clearly seen that sulfur has a high dissolution rate at the first 2 cycles, followed by fast dissolution rate decay as the electrode is continuously cycled. The cyclic voltammetries for both materials remain relatively stable after the applied cycles. The small differences may be due removal of possible impurities and reactants residues after the material synthesis.

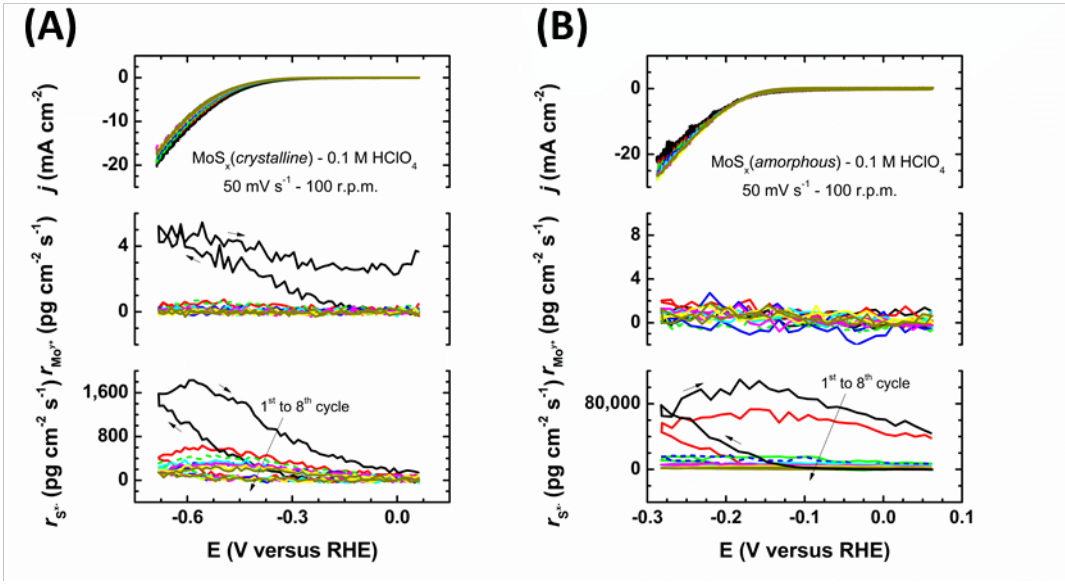

Source: own authorship.

Although quite unexpected, the occurrence of selective sulfur loss with no measurable dissolution to Mo indicates three important aspects of this process. First, even though the ICP-MS cannot distinguish the chemical nature of the sulfur species that are being leached from the catalyst surface, the XPS analysis in Figure 17(A) together with the highly acidic electrolyte (e.g., pH ~1) would suggest that sulfur may be reacting with hydronium ions and forming H_2S, as expected from thermodynamic considerations. Despite possible formation of H_2S, we emphasize that the rate of sulfur loss is rather small relative to H_2 production currents (see Figure 19). Second, the transient nature of the process (Figure 18) reveals that only the very first atomic layers of material may be participating in this process, reducing the role of the bulk of MoS_2 as the source of sulfur loss. In this sense, it is plausible to suggest that the selective sulfur loss observed in Figure 17(C) is somehow connected to the catalytic mechanism for hydrogen production. Third, the absence of $_{Mo}$ dissolution in Figure 17(C), a 4+ species as revealed by the XPS analysis (Figure 17(A)), may indicate that some other non-soluble Mo species is being left behind after sulfur is leaving the surface.

Figure 19. Hydrogen evolution reaction (HER) curves and S dissolution curves plotted in E vs j mode for (A) MoS_2(crystalline) and (B) MoS_x(amorphous). Conditions: 0.1 mol L^{-1} of $HClO_4$ at Ar atmosphere, with 50 mV s^{-1} scan rate and 100 r. p. m. rotation rate. Analyzing this data, we see that the amount of sulfur dissolved during HER process represents only a really percentage of the HER current density (~0.03% for MoS_2(crystalline) and ~1.8% for MoS_x(amorphous)). By doing this comparison, we can avoid miss interpretation of the real HER activity for the electrocatalysts studied, separating the contribution of sulfur dissolution in the total measured current density. It is worth noting that Mo dissolution rate are too small to have any significance in the total current density.

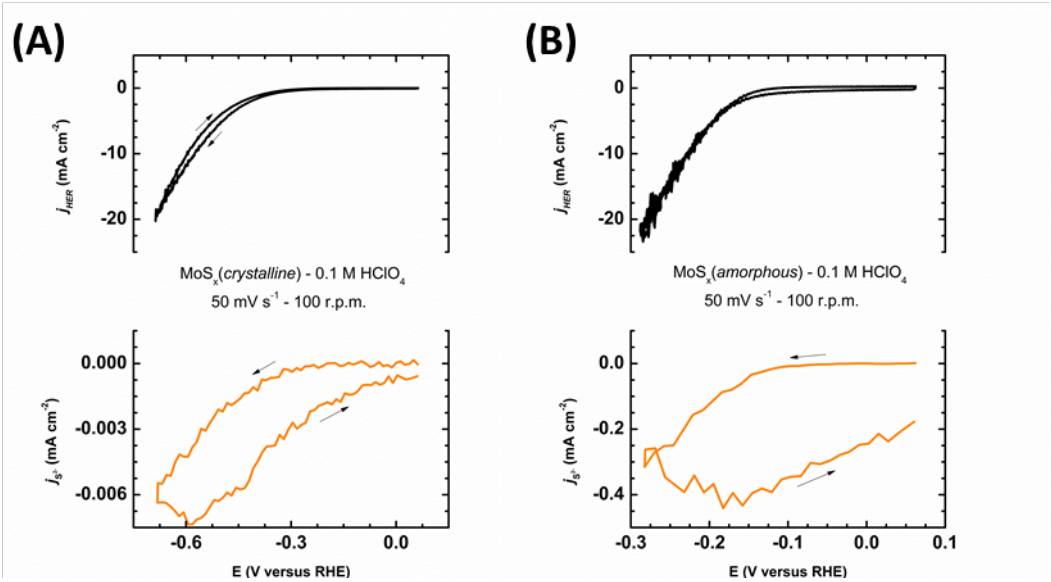

Source: own authorship.

All of features mentioned above are also observed on the MoS_x chalcogel, as seen in Figure 17(D). As previously discussed, the inherent high surface area of the amorphous structure increases the number of active sites for HER, as demonstrated in the polarization curve for H_2 production. Unlike observed for MoS_2, the MoS_x catalyst generates HER currents of ca. 20 mA cm^{-2} at only -0.28 V, decreasing the overpotential for the HER by 0.42 V as compared to MoS_2, even though both electrodes contain the same mass-load of material (see Section 3.2). However, the higher activity of the amorphous chalcogel is accompanied by a higher dissolution of sulfur (ca. 70 ng cm^{-2} s^{-1}, maximum rate value), also occurring at lower overpotentials simultaneous to H_2 formation (Figure 17(D)). We highlight that the substantial increase in the rate of sulfur loss from MoS_x as compared to MoS_2 might be related to the presence of poly-sulfide moieties (XPS results shown in Figure 17(B)), as it will be discussed in detail in the next section. Taken together, these results demonstrate the existence of a selective sulfur dissolution process concomitant to the HER that occurs on both well-defined crystalline MoS_2 and amorphous MoS_x materials, showing that the surfaces are evolving (changing) during hydrogen electrocatalysis. This selective dissolution raises the question about what might be happening to the surface of MoS_x materials, which species are left behind, and how it can influence the overall HER electrocatalysis. These issues will be discussed in the next section.

3.3.2 Surface deactivation by MoS_x conversion to MoO_x

In order to investigate the consequences of the selective dissolution of sulfur during HER we performed potential step experiments (i.e., chrono-amperometry measurements, as shown in Figure 20(A)), which is representative of operational conditions of water electrolyzers[53], but it can help us to understand the origin of the transient nature of the process, as well as to draw correlations to modifications in the surface chemistry and changes to HER activity. For that, we will focus our attention to MoS_x as the higher density of active sites compared to MoS_2 allows XPS to be employed to probe changes in the surface chemical speciation after electrochemical conditioning. However, we emphasize that both materials experiences similar processes, namely, selective sulfur dissolution followed by decrease in HER activity (Figure 20(B) Figure 21). An important feature observed from stepping the potential to negative values is the immediate dissolution of sulfur together with H_2 formation, decreasing to steady values after a few seconds, but only stops when the potential returns to the initial holding conditions. It is noteworthy to mention that during the potential step it was

possible to observe a small, yet distinguishable Mo leaching rate together with the HER on MoS_x, which is still 3 orders of magnitude smaller than the corresponding dissolution of S from the same catalyst surface (Figure 20(A) and Figure 20(C)). The overall effect of the selective S loss can be seen in Figure 20(B) and Figure 20(C), which show that 5 min of continuous H_2 production is enough to decrease the activity of MoS_2 by half (e.g., from 4 to 2 mA cm^{-2} at -0.5 V), while near 75% of the initial HER activity was retained on MoS_2 during the same polarization time. Overall, the results shown in Figure 17, and Figure 20(A)-(C) indicate a correlation between the catalyst deactivation and sulfur loss, emphasizing that the origin of deactivation might be related to changes to Mo species near the surface. Considering that in situ X-ray spectroscopy does not reveal any significant formation of reduced Mo atoms, excluding the formation of metallic Mo at negative potentials (Figure 22(A)-(B)), it is unlikely that the lack of Mo dissolution is not accompanied by chemical speciation changes.

Figure 20. (A) Steady-state polarization curve at HER regime and concomitant Mo and S dissolution profiles for MoS_x(amorphous). It is evident that at negative potential values the dissolution is selective towards S, which is continuously dissolved over the 5 min course of HER. (B) Deactivation process of both MoS_2(crystalline) and MoS_x(amorphous) after 5 min at HER regime. The potential magnitude applied for each material is different in order to obtain close activity towards hydrogen evolution. (C) Correspondent amounts of Mo and S dissolved during the course of HER regime described in (A) and (B) for both catalysts. (D) XPS spectra for MoS_x(amorphous) before and after 5 h at HER regime (E = -0.30 V vs RHE). (E) Density functional theory (DFT) results adapted from[172]. Briefly, the calculated Pourbaix diagram for the surface states of the Mo-edge cluster and the schematic of the transition state structure considered for H_2 formation are shown in the left and right sides, respectively.

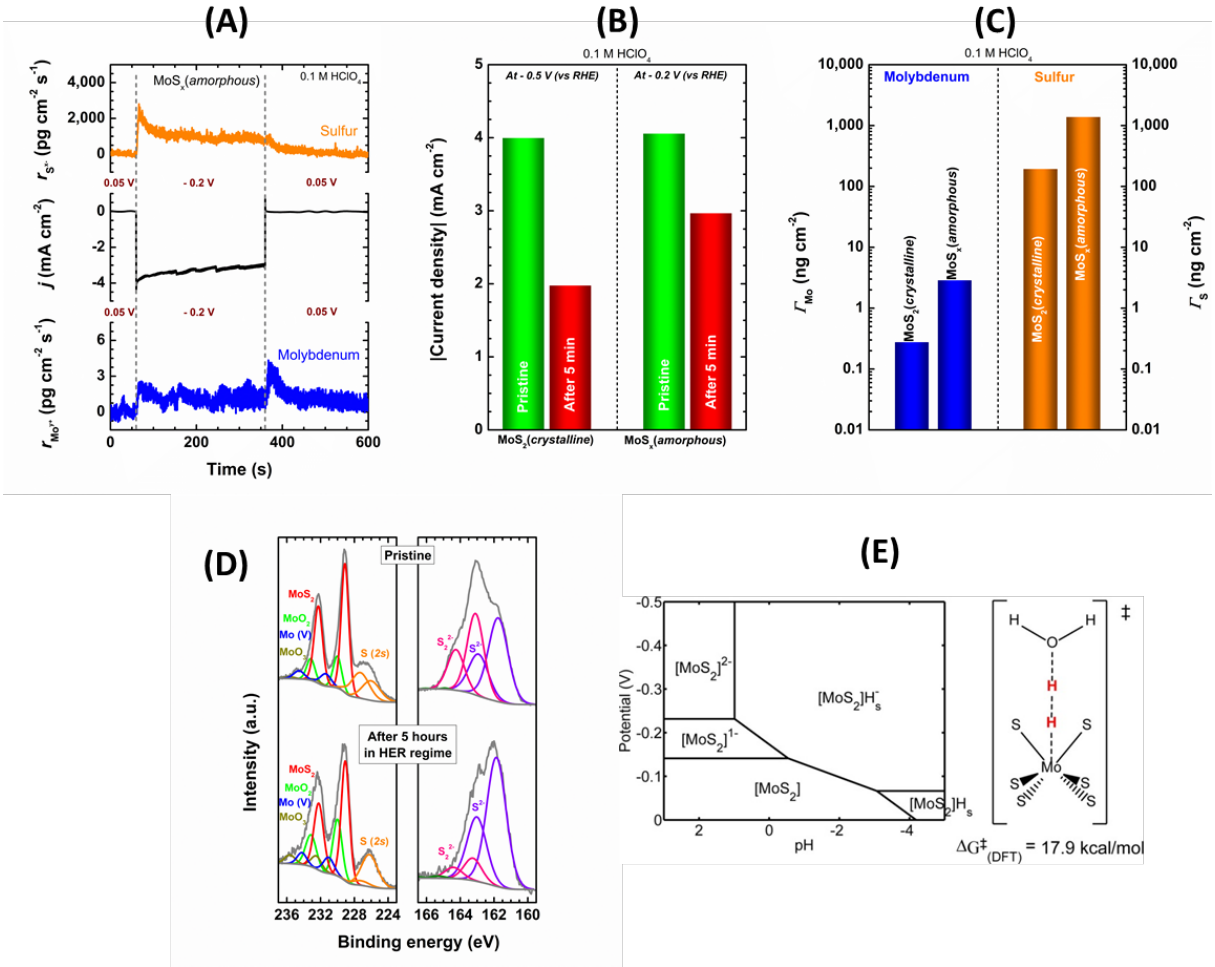

Source: (A), (B) and (C) – own authorship. (D) – adapted from reference [172].

Figure 21. Steady-state polarization curve at HER region (middle panel) with concomitant dissolution profiles of Mo (upper panel) and S (bottom panel) for MoS_2(crystalline). Conditions: 0.1 mol L^{-1} of $HClO_4$ at Ar atmosphere, with 50 mV s^{-1} scan rate and 100 r. p. m. rotation rate. After polarizing the electrode at -0.2 V vs RHE, we observe a high S dissolution compared with Mo dissolution, which continue until the electrode is polarized back to 0.05 V vs RHE, where we can see a considerable Mo dissolution which is later ascribed to MoO_x species dissolution from the electrode/electrolyte interface. This MoO_x species are suggested to be formed concomitant with HER process, and MoO_x has a detrimental consequence to the HER activity (see Figure 23).

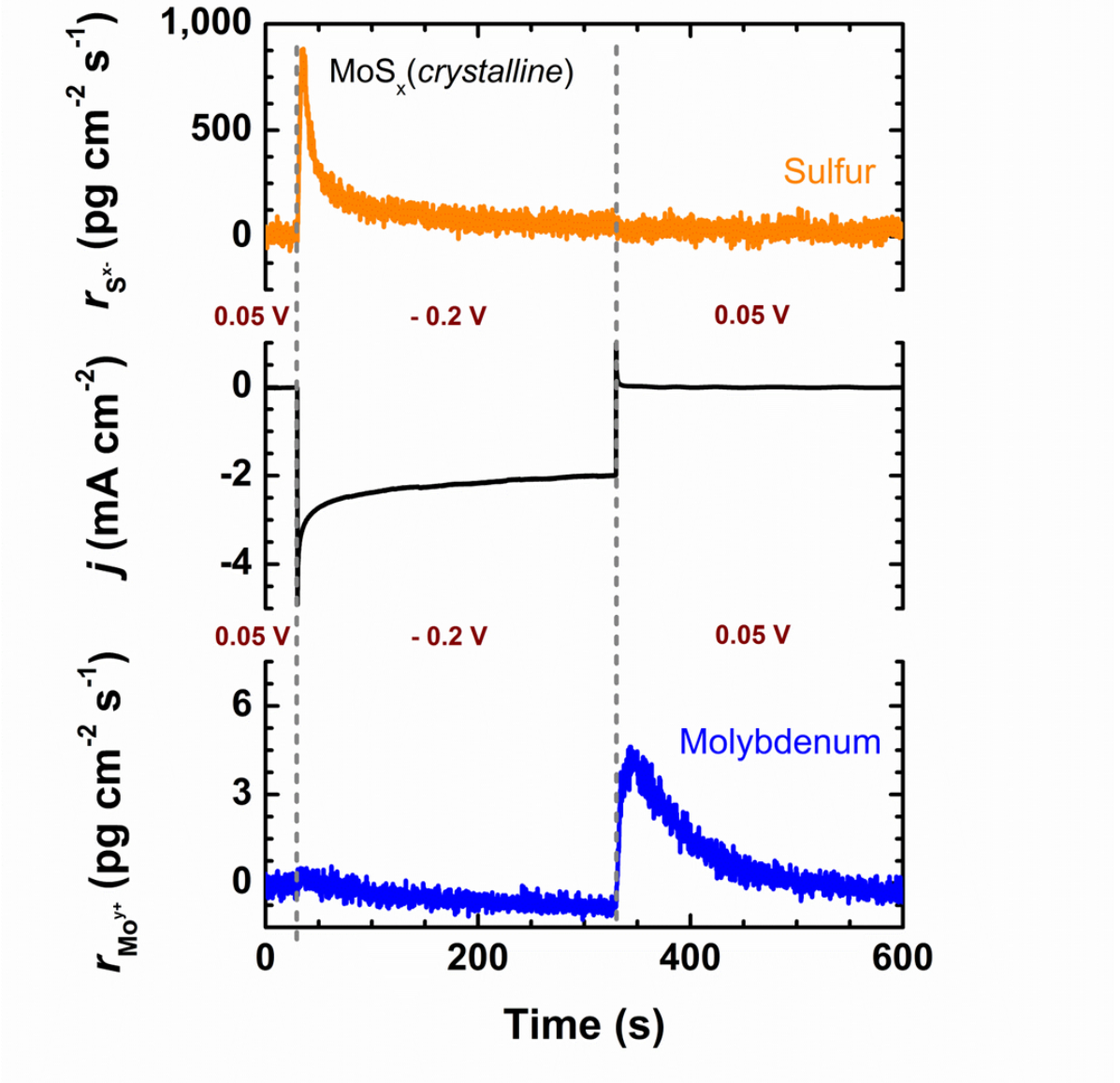

Source: own authorship.

Figure 22. XPS spectra of MoS_2(crystalline) (A) before and (B) after polarization at HER region. No major differences can be seen between these samples, contrary with what was seen for MoS_x(amorphous) (see main text). This indicates if any changes have occurred, they are below 1% the first 5-10 nm of the materials surface.

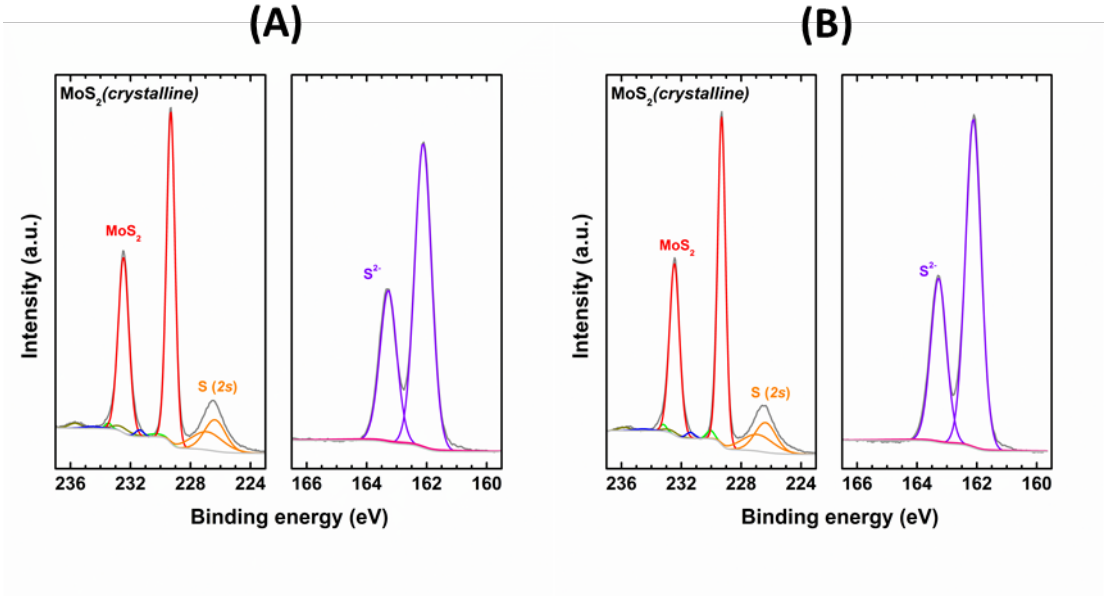

Source: own authorship.

To address this in further detail, XPS analysis of the catalyst surface before and after extended continuous polarization to HER (ca. 5 h of potential hold) reveals significant modifications to surface chemistry on both Mo and S sites (Figure 20(D)). While we observe a decrease in the poly-sulfide content relative to sulfide peaks in the S 2p core-level region, in line with the higher rates of S loss from MoS_x than on MoS_2 (Figure 17), it is noteworthy the significant increase in the MoO_x content as seen from Mo 3d core-level region. The appearance of more oxides with decrease in Mo-S content would suggest that indeed, the selective sulfur loss induces molybdenum speciation change; namely, Mo-S bonds are converted to Mo-O bonds as sulfur is being removed from the catalyst surface. This fact would explain the decrease in HER activity, as MoO_x are less active for HER than MoS_x (Figure 23).

Figure 23. HER curves of MoS_2(crystalline) and MoO_2(crystalline) at 0.1 mol L^{-1} of $HClO_4$ at Ar atmosphere, with 50 mV s^{-1} scan rate and 100 r. p. m. rotation rate. These curves clearly show the HER activity differences between Mo oxide and Mo sulfide, which is in great accordance with the proposed mechanism of MoS_2 de-activation that may happen concomitant with the HER process.

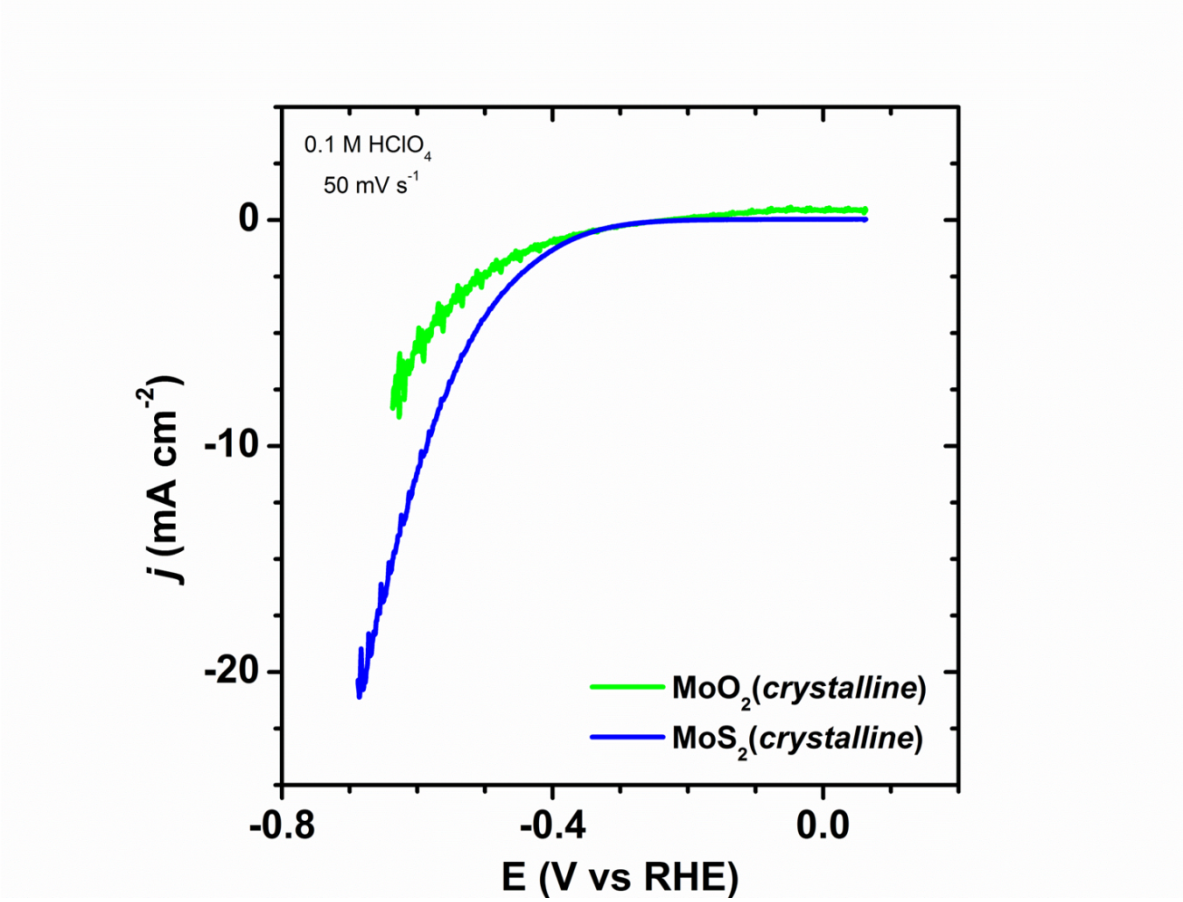

Source: own authorship.

Thus, the overall surface modification process can be seen as a sequence of steps, first triggered by selective sulfur dissolution due S-H interaction, which then is accompanied by molybdenum oxide formation, as the abundance of water and hydronium would promptly replace the recently removed sulfur atoms by oxygen, rendering the catalyst surface less active for the HER, thus, completing the deactivation pathway. In order to gain deeper insight into the deactivation mechanism, we are currently working on DFT calculations (results not yet available, therefore not shown in this work) to explore the thermodynamic driving forces behind sulfur loss, oxygen replacement and HER deactivation. Nevertheless, previous DFT results calculated by Goddard and co-workers[172] (summarized in Figure 20(E)) identified that the rate determining step, where a sulfur-bind hydrogen needs to overcome a kinetic barrier to form a Mo-H intermediate, is crucial for the sulfur removal step. As the strong interaction between sulfur and hydrogen weakens the Mo-S bond at negative potentials, this leads to the possibility of another proton to interact with the existing SH group, effectively removing

sulfur as H_2S. However, the presence of water serves to stabilize the Mo sites that are being left behind (new 'empty' sites), lowering further the thermodynamic barrier for this process to occur. As a consequence, the newly formed Mo-O-H activated complex has a higher barrier for hydrogen to bind to molybdenum sites, making the HER catalytic cycle less effective, in agreement with MoO_x sites being less active for the HER than MoS_x ones (Figure 23). Therefore, our experimental and Goddard and co-workers[172] theoretical results indicate the origin for the active site deactivation mechanism that occurs on MoS_x materials that are catalyzing the HER in acid media. Now that we have a better understanding of the mechanism behind HER deactivation, we shall explore the possibility of regenerating the active sites in situ by selective dissolution of inactive Mo oxides.

3.3.3 Selective molybdenum dissolution and active-site regeneration

The deactivation mechanism observed on Mo-S-based materials (Figure 17 and Figure 20) can be considered as a site-blocking process, where the newly formed MoO_x species block the underlying Mo-S sites, similarly to what is observed on fuel cell catalysts in the presence of anion (Cl^-, Br^-, etc.) impurities[22], that are known to strongly adsorb on the surface of Pt at potentials relevant for the oxygen reduction reaction. However, in order to regenerate these blocked sites, it is necessary to drive the electrode potentials to conditions such that the adsorbed species are no longer stable at the surface of the material. Thus, in Figure 24(A) we perform another potential step experiment, but this time driving the electrode potential to positive values, e.g., 0.8 V, as previous studies indicate that MoS_x species should not be stable at such conditions[171].

Figure 24. (A) Steady-state polarization curve at a positive potential (E ~0.8 V vs RHE) and concomitant Mo and S dissolution profiles for MoS_x(amorphous). (B) Cyclic voltammetry at positive potentials and concomitant Mo dissolution profile for MoS_2(crystalline), MoS_x(amorphous) and MoO_2(crystalline) in 0.1 mol L^{-1} of $HClO_4$ at Ar atmosphere, with 50 mV s^{-1} scan rate and 100 r. p. m. rotation rate. (C) Regeneration process for MoS_x(amorphous): after ca. 30 min polarized at ~-0.3 V, a cyclic voltammetry starting at ~-0.3 V and going positive is performed (gray curve in upper panel). The regeneration process is clearly seen in the negative direction of cyclic voltammetry, matching the pristine HER activity of the pristine electrode. The dissolution process of Mo (middle panel) and S (bottom panel) is followed during the cyclic voltammetry.

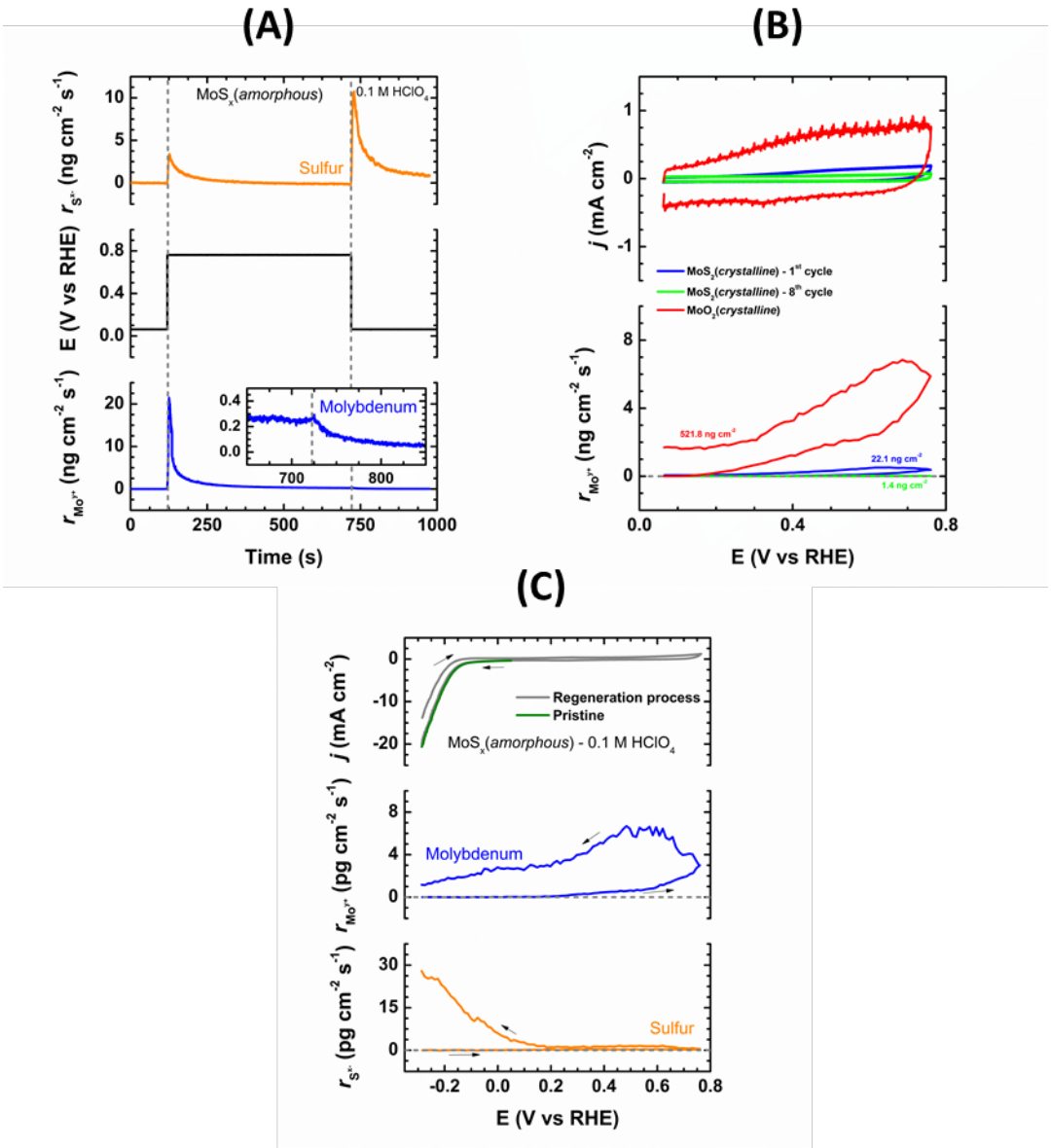

Source: own authorship.

Opposite to the trends observed in Figure 17 and Figure 20, the MoS_x material pre-covered with MoO_x undergo substantial dissolution of Mo at positive potentials, with initial S dissolution rates at least 10 times slower than what is observed for Mo dissolution rates. Note that the same process occurs on MoS_2 (Figure 25), providing an indirect

confirmation that the crystalline edge sites may also be converted to MoO_x species, even though XPS analysis cannot detect chemical speciation changes that are below 1% the first 5-10 nm of the material's surface (Figure 26). We also observe that after the first few minutes, the dissolution rate of Mo shows a small but continuous rate that returns to zero only after the electrode potential is stepped back to its initial value, ca. 0.05 V. Not surprisingly, returning the potential back to 0.05 V now triggers some sulfur loss, as the surface is freshly clean from MoO_x-blocking-species. To confirm that the selective dissolution of Mo arises from molybdenum oxides species we performed similar electrochemical experiments on a crystalline MoO_2 material that can serve as a standard MoO_2 surface. Figure 24(B) shows the results for cyclic voltammetry at MoO_2 and MoS_2, the later after it was polarized to negative potentials to form the MoO_x species at its surface (denoted as MoO_x/MoS_2). Note that there is a larger Mo dissolution rate coming from the MoO_2 material, while Mo loss from MoO_x/MoS_2 is noticeable only in the first scan towards positive potentials, but is almost on the background after the tenth consecutive scan. Thus, the selective dissolution of Mo observed from MoS_2 and MoS_x after they were subjected to HER conditions can be assigned to the dissolution of MoO_2-like species. Note that MoO_3 that are also formed on MoS_x in minor amounts (Figure 20(D)) can also undergo dissolution (Figure 27), but to a smaller degree than MoO_2.

Figure 25. Steady-state polarization curve at positive potential (~0.6 V vs. RHE) for MoS_2(crystalline). Conditions: 0.1 mol L^{-1} of $HClO_4$ at Ar atmosphere, 50 mV s^{-1} scan rate and 100 r. p. m. rotation rate. Mo dissolution is constantly dissolved at positive (~0.6 V vs. RHE), showing the high instability of this material in that region, which would impede it to be used for oxygen evolution/reduction reaction in pH 1.

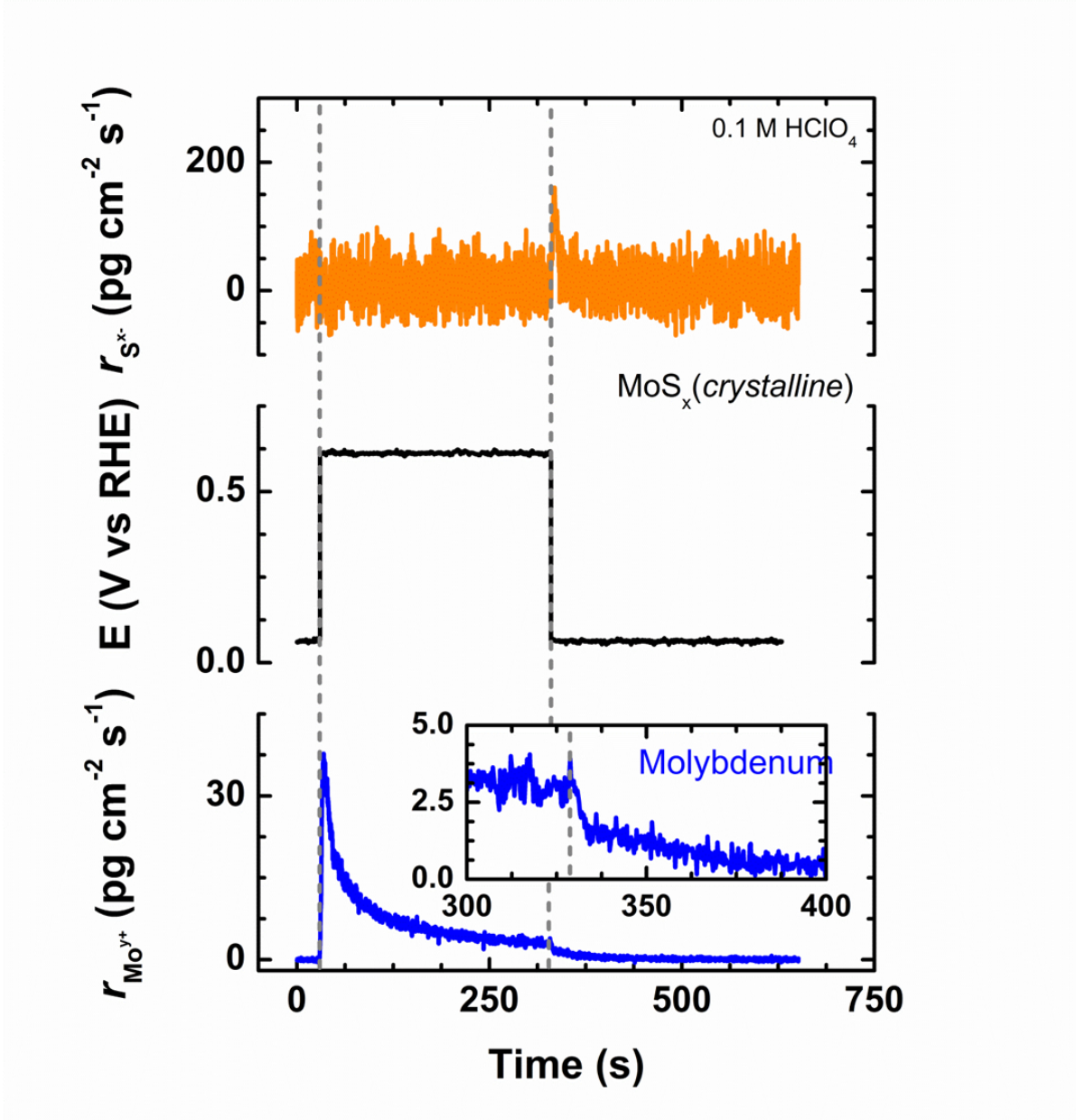

Source: own authorship.

Figure 26. XPS spectra of MoS_2(crystalline) (A) before and (B) after polarization at positive potentials. No major differences can be seen between these samples. This indicates if any changes have occurred, they are below 1% the first 5-10 nm of the material's surface.

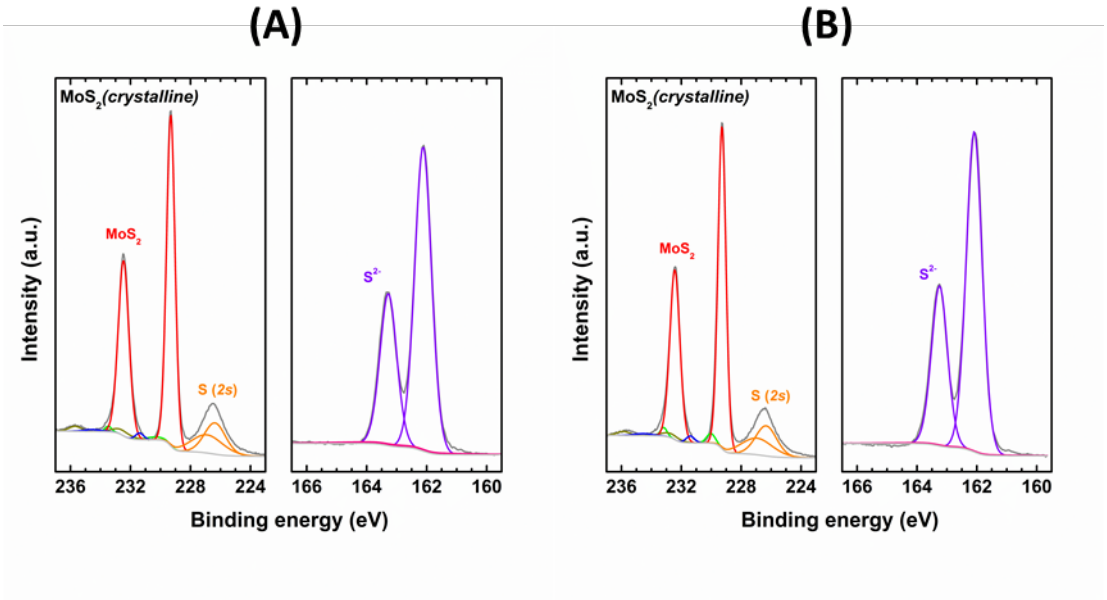

Source: own authorship.

Figure 27. Mo dissolution rates for MoO_2(crystalline) and MoO_3(crystalline) at positive potentials in 0.1 mol L^{-1} of $HClO_4$ at Ar atmosphere, 50 mV s^{-1} scan rate and 100 r. p. m. rotation rate. Both Mo oxides show high dissolution rates when polarized at positive potentials, which agrees with our proposition that any MoO_x species formed during the de-activation of MoS_2 material can be eliminated by simply polarizing the electrode at positive potentials.

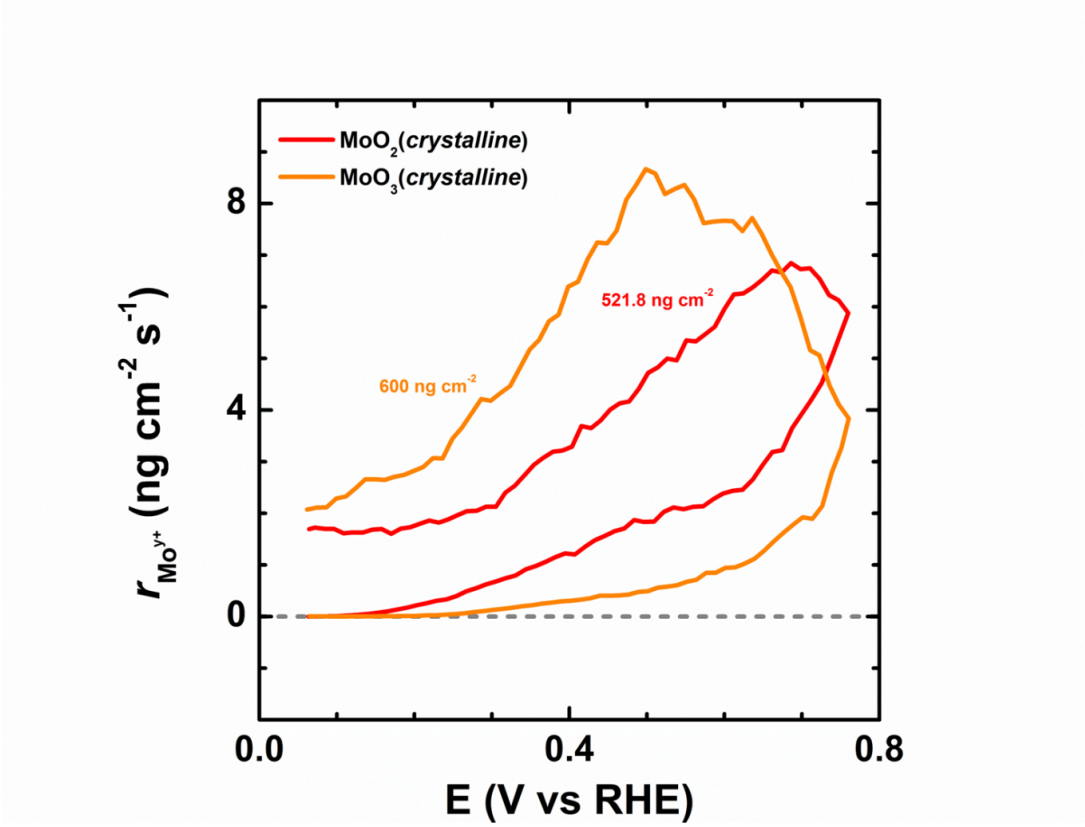

Source: own authorship.

The important consequence of being able to selectively remove MoO_x species is that it allows the catalyst surface to become active again for the HER. This regeneration step can be observed in Figure 24(C), where we perform a voltammetry scan starting from HER potentials (ca. -0.3 V), after the electrode was held at those potentials for at least 1 h. By starting the potential scan from negative to positive potentials, we observed the polarization curve less active than the pristine curve (Figure 24(C) (top panel)), and an close to zero dissolution rate of sulfur (Figure 24(C) (bottom panel)). However, while no Mo dissolves at HER conditions, soon after the potential goes above 0.2 V a selective Mo loss is observed (Figure 24(C) (middle panel)). By going all the way to 0.8 V and now scanning back to HER potential-region, the Mo dissolution process starts to decrease while sulfur dissolution appears below 0.2 V. As expected from the removal of MoO_x species, the activity of the catalyst for the HER is completely recovered to its pristine magnitude, emphasizing that it occurred after only one potential scan to positive values. We note that scanning the potential above 0.9 V can lead to simultaneous dissolution of molybdenum oxide and sulfide species (Figure 28(A)-(B)), which will cause instantaneous degradation of the active sites, leading to lower HER activity.

Figure 28. (A) Cyclic voltammetry followed by Mo and S dissolution rates for MoS_x(amorphous) at high positive potentials showing both high Mo and S dissolution. (B) HER curves before (black curve) and after (red curve) cyclic voltammetry presented in (A), showing the decrease of activity after just one high positive cycle. If we polarize at very positive potentials, the electrode is highly dissolved and this reflects in a decrease of HER activity (B) as one can expect that the amount of electro-active sites in the surface is smaller than in the pristine catalyst.

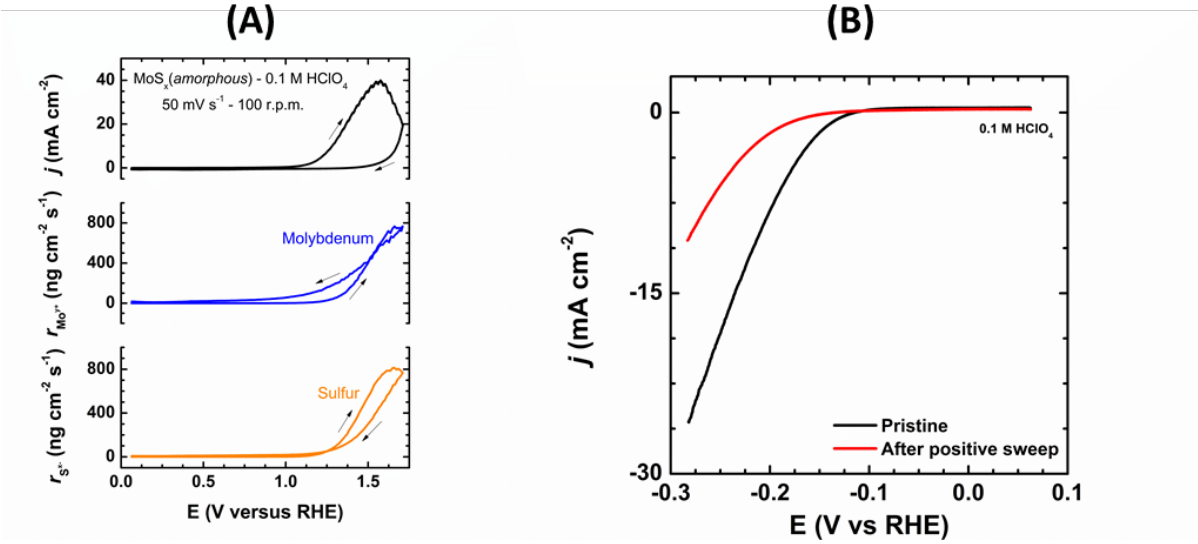

Source: own authorship.

3.4 Conclusions

The results presented in this Chapter demonstrate that the catalytic surfaces of both crystalline and amorphous Mo-S-like materials are constantly evolving in the electrochemical environment. The unexpected selective dissolution of sulfur that occurs at negative potentials concomitant to the HER leads to active site deactivation by MoO_x formation. However, even though these MoO_x species are less active for the HER than Mo-S-like sites, they can be selectively removed at positive potentials, restoring the catalytic performance of the initial Mo-S-like surface sites.

Overall then, we summarize these surface dynamics in Figure 29, showing a proposed reaction scheme that combine two important catalytic cycles: first the activity-cycle, depicting the sequence of steps and reaction intermediates for the HER on Mo-S-like sites; and second, the stability-cycle, comprised of both the deactivation mechanism and the regeneration step, that contains common intermediate species to the activity cycle. In the catalytic cycle, the initial Mo-S-like sites are reduced by the electrode potential, triggering a strong interaction between sulfur, hydronium and water molecules, forming a Mo-S-H complex. This Mo-S-H intermediate species are important for continuation of the HER cycle (activity-cycle), as the hydrogen can move to Mo centers and form the H_2 molecules following a Heyrovsky step and recovering the initial Mo-S-like sites, but also to sulfur removal as another hydronium or water can interact with SH groups and release sulfur as H_2S. As suggested by our preliminary DFT calculations (not shown in this work), the removal of sulfur is followed by oxygen coordination to Mo centers, producing then the MoO_x species observed experimentally that are less active for the HER than the initial Mo-S-like sites. After entering the stability-cycle by the deactivation mechanism, the inactive MoO_x species that are blocking the underlying Mo-S-like sites can be selectively removed by driving the electrode potential to higher values, effectively oxidizing the MoO_x centers to soluble ionic species. The final consequence is that fresh Mo-S-like sites become available once more for the activity cycle to continue the H_2 production. Finally, we emphasize that our results present a unique example of how understanding the underlying electrochemical properties of a material allow us to devise strategies to create a dynamic interface, which despite its inherent driving force for instability, can remain active by a simple re-activation step.

Figure 29. Proposed hydrogen evolution cycle and Deactivation/Re-activation mechanism.

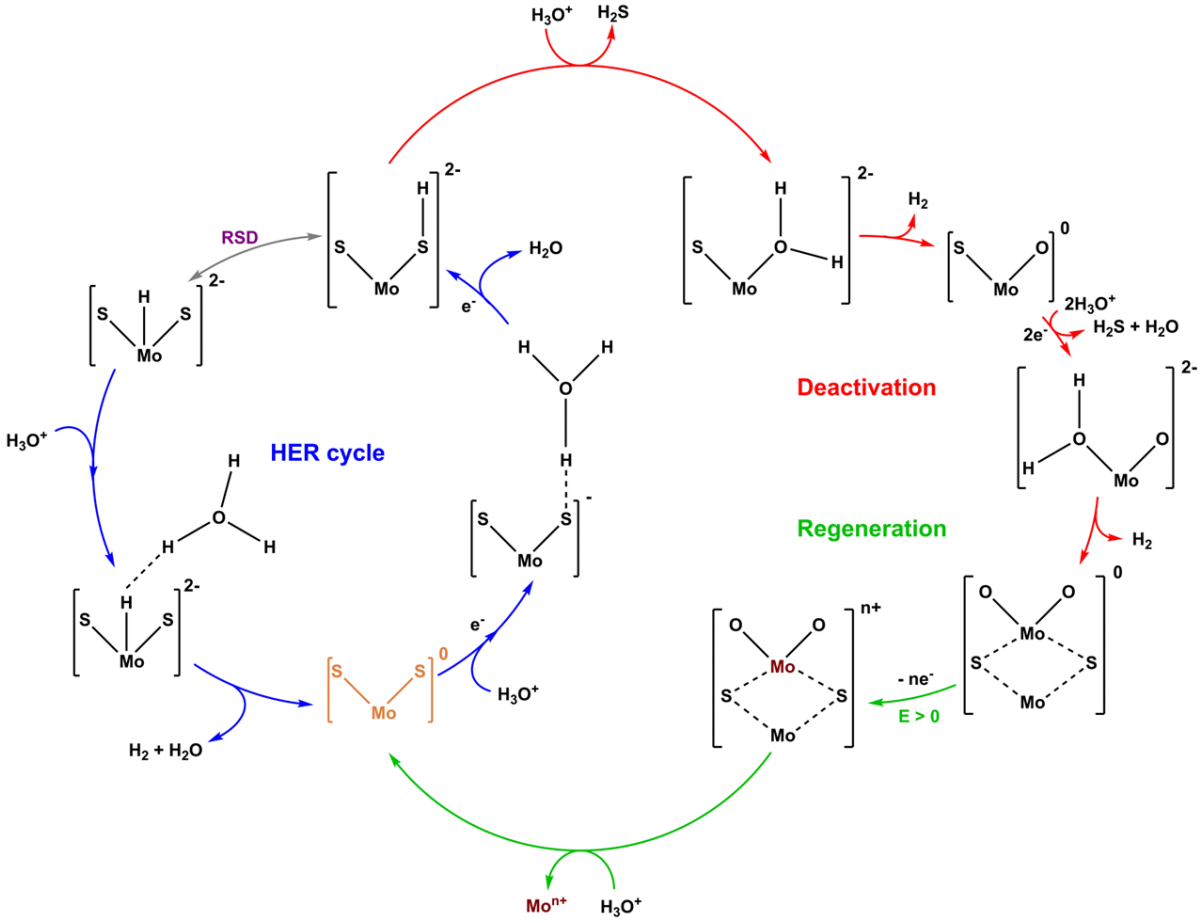

Source: own authorship.

CHAPTER 4

GENERAL CONCLUSIONS

4. General conclusions

In Chapter 2 we probed the dynamics of Pt dissolution via the stationary probe rotating disk electrode (SPRDE) method coupled to inductively coupled plasma mass spectrometry (ICPMS), and tracked the concomitant morphological changes using scanning tunneling microscopy (STM). We examine the dynamics of the electrochemical dissolution of Pt(111) surface atoms in clean, non-adsorbing $HClO_4$ electrolyte under experimental conditions that are relevant to fuel cell operation. Using this well-defined surface, we found that two distinct Pt dissolution processes can take place on the positive going sweep and negative going sweep regions, respectively, during a cyclic voltammetry (CV) with dissolution rates and morphological changes strongly dependent on the experimental conditions. We also found that the rate of dissolution during oxide formation (positive going sweep) is small and can be considered a faradaic process, as it is not closely related to the kinetics of oxide formation. Furthermore, the rate of dissolution and its associated Pt re-deposition is a fast process that is controlled by the positive potential limit and also by the scan rate used for oxide reduction (negative going sweep). Overall, the results provide a strong foundation for understanding how different potential and time profiles have an impact on the stability of Pt surfaces and their corresponding transition from a well-defined to "rough" morphology that ultimately determines the long-term electrode durability.

Furthermore, the results presented in Chapter 3 demonstrate that the catalytic surfaces of both crystalline and amorphous Mo-S-like materials are constantly evolving in the electrochemical environment. The unexpected selective dissolution of sulfur that occurs at negative potentials concomitant to the HER leads to active site deactivation by MoO_x formation. However, even though these MoO_x species are less active for the HER than Mo-S-like sites, they can be selectively removed at positive potentials, restoring the catalytic performance of the initial Mo-S-like surface sites. Thanks to SPRDE-ICPMS method, we were able to propose the surface dynamics of these materials by two important catalytic cycles: first the activity-cycle, depicting the sequence of steps and reaction intermediates for the HER on Mo-S-like sites; and second, the stability-cycle, comprised of both the deactivation mechanism and the regeneration step, that contains common intermediate species to the activity cycle. In the catalytic cycle, the initial Mo-S-like sites are reduced by the electrode potential, triggering a strong interaction between sulfur, hydronium and water molecules, forming a Mo-S-H complex. This Mo-S-H intermediate species are important for continuation of the HER cycle (activity-cycle), as the hydrogen can move to Mo centers and

form the H_2 molecules following a Heyrovsky step and recovering the initial Mo-S-like sites, but also to sulfur removal as another hydronium or water can interact with SH groups and release sulfur as H_2S. In sequence, the removal of sulfur is followed by oxygen coordination to Mo centers, producing then the MoO_x species observed experimentally that are less active for the HER than the initial Mo-S-like sites. After entering the stability-cycle by the deactivation mechanism, the inactive MoO_x species that are blocking the underlying Mo-S-like sites can be selectively removed by driving the electrode potential to higher values, effectively oxidizing the MoO_x centers to soluble ionic species. The final consequence is that fresh Mo-S-like sites become available once more for the activity cycle to continue the H_2 production. Finally, we emphasize that our results present a unique example of how understanding the underlying electrochemical properties of a material allow us to devise strategies to create a dynamic interface, which despite its inherent driving force for instability, can remain active by a simple re-activation step.

Overall, the present thesis forms yet another solid pillar (together with ref. 38) to support the importance of this relatively new analytical method (i.e. SPRDE-ICPMS) for electrochemistry processes. We hope that the readers can fell encouraged to pursue for a whole myriad of electrocatalytic phenomena well stablished in terms of structure-activity relationship, but still poor understood at the activity-stability level.

References

1. Thomas, R. *Practical Guide to ICP – MS*. (CRC Press, 2013). doi:10.1201/b14923
2. Available at: http://www.perkinelmer.com/lab-solutions/resources/docs/TCH-30-Minute-Guide-to-ICP-MS-006355G_01.pdf. (Accessed: 16th September 2018)
3. *Inductively Coupled Plasma Mass Spectrometry Handbook*. (Blackwell Publishing Ltd., 2005). doi:10.1002/9781444305463
4. Klemm, S. O., Topalov, A. A., Laska, C. A. & Mayrhofer, K. J. J. Coupling of a high throughput microelectrochemical cell with online multielemental trace analysis by ICP-MS. *Electrochem. commun.* **13**, 1533–1535 (2011).
5. Available at: https://www.energy.gov/eere/fuelcells/durability-working-group. (Accessed: 9th September 2018)
6. Available at: https://www.energy.gov/eere/fuelcells/downloads/fuel-cell-technologies-office-multi-year-research-development-and-22. (Accessed: 9th September 2018)
7. Available at: https://www.nace.org/uploadedFiles/Publications/ccsupp.pdf. (Accessed: 18th September 2018)
8. Ferreira, P. J. *et al.* Instability of Pt／C Electrocatalysts in Proton Exchange Membrane Fuel Cells: A Mechanistic Investigation . *J. Electrochem. Soc.* **152**, A2256–A2271 (2005).
9. Pourbaix, M. *Atlas of electrochemical equilibria in aqueous solutions*. (Pergamon Press, 1966).
10. Wang, X., Kumar, R. & Myers, D. J. Effect of Voltage on Platinum Dissolution: Relevance to Polymer Electrolyte Fuel Cells . *Electrochem. Solid-State Lett.* **9**, A225–A227 (2006).
11. Gilman, S. Modification of the surface area of platinum electrodes by the application of single pulses. *J. Electroanal. Chem.* **9**, 276–281 (1965).
12. Biegler, T. Area Changes of a Smooth Platinum Electrode. *J. Electrochem. Soc.* **114**, 1261–1262 (1967).
13. Johnson, D. C., Napp, D. T. & Bruckenstein, S. A ring-disk electrode study of the current/potential behaviour of platinum in 1.0 M sulphuric and 0.1 M perchloric acids. *Electrochim. Acta* **15**, 1493–1509 (1970).
14. Vetter, K. J. & Schultze, J. W. The kinetics of the electrochemical formation and reduction of monomolecular oxide layers on platinum in 0.5 M H2SO4: Part I. Potentiostatic pulse measurements. *J. Electroanal. Chem. Interfacial Electrochem.* **34**, 131–139 (1972).
15. Kinoshita, K., Lundquist, J. T. & Stonehart, P. Potential cycling effects on platinum electrocatalyst surfaces. *J. Electroanal. Chem. Interfacial Electrochem.* **48**, 157–166 (1973).
16. Rand, D. A. J. & Woods, R. A study of the dissolution of platinum, palladium, rhodium and gold electrodes in 1 m sulphuric acid by cyclic voltammetry. *J. Electroanal. Chem. Interfacial Electrochem.* **35**, 209–218 (1972).
17. Debe, M. K. Electrocatalyst approaches and challenges for automotive fuel cells. *Nature* **486**, 43 (2012).
18. Clavilier, J., Faure, R., Guinet, G. & Durand, R. Preparation of monocrystalline Pt microelectrodes and electrochemical study of the plane surfaces cut in the direction of the {111} and {110} planes. *J. Electroanal. Chem. Interfacial Electrochem.* **107**, 205–

209 (1980).
19. Markovic, N., Hanson, M., McDougall, G. & Yeager, E. The effects of anions on hydrogen electrosorption on platinum single-crystal electrodes. *J. Electroanal. Chem. Interfacial Electrochem.* **214**, 555–566 (1986).
20. Tidswell, I. M., Marković, N. M. & Ross, P. N. Potential dependent surface relaxation of the Pt(001)/electrolyte interface. *Phys. Rev. Lett.* **71**, 1601–1604 (1993).
21. Tidswell, I. M., Marković, N. M., Lucas, C. A. & Ross, P. N. In situ x-ray-scattering study of the Au(001) reconstruction in alkaline and acidic electrolytes. *Phys. Rev. B* **47**, 16542–16553 (1993).
22. Marković, N. M. & Ross, P. N. Surface science studies of model fuel cell electrocatalysts. *Surf. Sci. Rep.* **45**, 117–229 (2002).
23. Stamenkovic, V. R. *et al.* Improved Oxygen Reduction Activity on Pt₃Ni(111) via Increased Surface Site Availability. *Science (80-.).* **315**, 493 LP-497 (2007).
24. Tian, N., Zhou, Z.-Y., Sun, S.-G., Ding, Y. & Wang, Z. L. Synthesis of Tetrahexahedral Platinum Nanocrystals with High-Index Facets and High Electro-Oxidation Activity. *Science (80-.).* **316**, 732 LP-735 (2007).
25. Lim, B. *et al.* Pd-Pt Bimetallic Nanodendrites with High Activity for Oxygen Reduction. *Science (80-.).* **324**, 1302 LP-1305 (2009).
26. Greeley, J., Rossmeisl, J., Hellmann, A. & Norskov, J. K. Theoretical Trends in Particle Size Effects for the Oxygen Reduction Reaction. *Zeitschrift für Phys. Chemie* **221**, 1209–1220 (2007).
27. Conway, B. E. Electrochemical oxide film formation at noble metals as a surface-chemical process. *Prog. Surf. Sci.* **49**, 331–452 (1995).
28. Kolb, D. M. Reconstruction phenomena at metal-electrolyte interfaces. *Prog. Surf. Sci.* **51**, 109–173 (1996).
29. Komanicky, V. *et al.* Stability and Dissolution of Platinum Surfaces in Perchloric Acid. *J. Electrochem. Soc.* **153**, B446–B451 (2006).
30. Itaya, K. In situ scanning tunneling microscopy in electrolyte solutions. *Prog. Surf. Sci.* **58**, 121–247 (1998).
31. Kolb, D. M. Structure studies of metal electrodes by in-situ scanning tunneling microscopy. *Electrochim. Acta* **45**, 2387–2402 (2000).
32. Ocko, B. M., Helgesen, G., Schardt, B., Wang, J. & Hamelin, A. Charge induced (1\ifmmode\times\else\texttimes\fi{}3) reconstruction of the Au(110) surface: An x-ray scattering study. *Phys. Rev. Lett.* **69**, 3350–3353 (1992).
33. Marković, N. M., Grgur, B. N., Lucas, C. A. & Ross, P. N. Surface electrochemistry of CO on Pt(110)-(1 × 2) and Pt(110)-(1 × 1) surfaces. *Surf. Sci.* **384**, L805–L814 (1997).
34. Lucas, C. A., Marković, N. M. & Ross, P. N. Surface Structure and Relaxation at the Pt(110)/Electrolyte Interface. *Phys. Rev. Lett.* **77**, 4922–4925 (1996).
35. Ocko, B. M., Wang, J., Davenport, A. & Isaacs, H. In situ x-ray reflectivity and diffraction studies of the Au(001) reconstruction in an electrochemical cell. *Phys. Rev. Lett.* **65**, 1466–1469 (1990).
36. Available at: https://www.hydrogen.energy.gov/pdfs/review18/fc135_borup_2018_o.pdf. (Accessed: 9th October 2018)
37. Homazava, N., Ulrich, A., Trottmann, M. & Krähenbühl, U. Micro-capillary system coupled to ICP-MS as a novel technique for investigation of micro-corrosion

processes. *J. Anal. At. Spectrom.* **22**, 1122–1130 (2007).
38. Lopes, P. P. *et al.* Relationships between Atomic Level Surface Structure and Stability/Activity of Platinum Surface Atoms in Aqueous Environments. *ACS Catal.* **6**, 2536–2544 (2016).
39. Lopes, P. P. *et al.* Dynamics of electrochemical Pt dissolution at atomic and molecular levels. *J. Electroanal. Chem.* **819**, 123–129 (2018).
40. Stamenkovic, V. R., Strmcnik, D., Lopes, P. P. & Markovic, N. M. Energy and fuels from electrochemical interfaces. *Nat. Mater.* **16**, 57 (2016).
41. Grey, C. P. & Tarascon, J. M. Sustainability and in situ monitoring in battery development. *Nat. Mater.* **16**, 45 (2016).
42. Montoya, J. H. *et al.* Materials for solar fuels and chemicals. *Nat. Mater.* **16**, 70 (2016).
43. Wilson, R. & Turner, A. P. F. Glucose oxidase: an ideal enzyme. *Biosens. Bioelectron.* **7**, 165–185 (1992).
44. Wang, J. Electrochemical biosensors: Towards point-of-care cancer diagnostics. *Biosens. Bioelectron.* **21**, 1887–1892 (2006).
45. Hirt, L., Reiser, A., Spolenak, R. & Zambelli, T. Additive Manufacturing of Metal Structures at the Micrometer Scale. *Adv. Mater.* **29**, 1604211 (2017).
46. *Modern Electroplating*. (John Wiley & Sons, Inc., 2010). doi:10.1002/9780470602638
47. Tallman, D. E., Spinks, G., Dominis, A. & Wallace, G. G. Electroactive conducting polymers for corrosion control. *J. Solid State Electrochem.* **6**, 73–84 (2002).
48. Spinks, G. M., Dominis, A. J., Wallace, G. G. & Tallman, D. E. Electroactive conducting polymers for corrosion control. *J. Solid State Electrochem.* **6**, 85–100 (2002).
49. Landolt, D. *Corrosion and Surface Chemistry of Metals*. (EFPL Press, 2007). doi:10.1201/9781439807880
50. Clavilier, J. The role of anion on the electrochemical behaviour of a {111} platinum surface; an unusual splitting of the voltammogram in the hydrogen region. *J. Electroanal. Chem. Interfacial Electrochem.* **107**, 211–216 (1980).
51. Markovića, N. M., Sarraf, S. T., Gasteiger, H. A. & Ross, P. N. Hydrogen electrochemistry on platinum low-index single-crystal surfaces in alkaline solution. *J. Chem. Soc. Faraday Trans.* **92**, 3719–3725 (1996).
52. Markovic, N. M., Gasteiger, H. A. & Ross, P. N. Oxygen Reduction on Platinum Low-Index Single-Crystal Surfaces in Sulfuric Acid Solution: Rotating Ring-Pt(hkl) Disk Studies. *J. Phys. Chem.* **99**, 3411–3415 (1995).
53. Greeley, J. & Markovic, N. M. The road from animal electricity to green energy: combining experiment and theory in electrocatalysis. *Energy Environ. Sci.* **5**, 9246–9256 (2012).
54. Gómez-Marín, A. M. & Feliu, J. M. Oxide growth dynamics at Pt(111) in absence of specific adsorption: A mechanistic study. *Electrochim. Acta* **104**, 367–377 (2013).
55. Gómez-Marín, A. M., Clavilier, J. & Feliu, J. M. Sequential Pt(111) oxide formation in perchloric acid: An electrochemical study of surface species inter-conversion. *J. Electroanal. Chem.* **688**, 360–370 (2013).
56. *Fuel Cell Catalysis*. (John Wiley & Sons, Inc., 2009). doi:10.1002/9780470463772
57. Strmcnik, D. *et al.* When Small is Big: The Role of Impurities in Electrocatalysis. *Top. Catal.* **58**, 1174–1180 (2015).
58. Stamenkovic, V., M. Markovic, N. & Ross, P. N. Structure-relationships in electrocatalysis: oxygen reduction and hydrogen oxidation reactions on Pt(111) and

Pt(100) in solutions containing chloride ions. *J. Electroanal. Chem.* **500**, 44–51 (2001).
59. Conway, B. E. & Jerkiewicz, G. Surface orientation dependence of oxide film growth at platinum single crystals. *J. Electroanal. Chem.* **339**, 123–146 (1992).
60. Marković, N. M., Schmidt, T. J., Stamenković, V. & Ross, P. N. Oxygen Reduction Reaction on Pt and Pt Bimetallic Surfaces: A Selective Review. *Fuel Cells* **1**, 105–116 (2001).
61. Itaya, K., Sugawara, S., Sashikata, K. & Furuya, N. In situ scanning tunneling microscopy of platinum (111) surface with the observation of monatomic steps. *J. Vac. Sci. Technol. A* **8**, 515–519 (1990).
62. Alsabet, M., Grden, M. & Jerkiewicz, G. Comprehensive study of the growth of thin oxide layers on Pt electrodes under well-defined temperature, potential, and time conditions. *J. Electroanal. Chem.* **589**, 120–127 (2006).
63. Gómez–Marín, A. M. & Ticianelli, E. A. A reviewed vision of the oxygen reduction reaction mechanism on Pt-based catalysts. *Curr. Opin. Electrochem.* **9**, 129–136 (2018).
64. Strmcnik, D. S. *et al.* Unique Activity of Platinum Adislands in the CO Electrooxidation Reaction. *J. Am. Chem. Soc.* **130**, 15332–15339 (2008).
65. Gileadi, E. *Electrode Kinetics for Chemists, Chemical Engineers and Materials Scientists*. (VCH, 1993).
66. Li, D. *et al.* Functional links between Pt single crystal morphology and nanoparticles with different size and shape: the oxygen reduction reaction case. *Energy Environ. Sci.* **7**, 4061–4069 (2014).
67. May, T. W. & Wiedmeyer, R. H. A table of polyatomic interferences in ICP-MS. *At. Spectrosc.* **19**, 150–155 (1998).
68. Available at: https://www.perkinelmer.com/CMSResources/Images/44-74379ATL_TableOfPolyatomicInterferences.pdf. (Accessed: 9th October 2018)
69. Bard, A. J. & Faulkner, L. R. *Electrochemical Methods: Fundamentals and Applications*. (John Wiley & Sons, Inc., 2000).
70. Strmcnik, D. *et al.* The role of non-covalent interactions in electrocatalytic fuel-cell reactions on platinum. *Nat. Chem.* **1**, 466 (2009).
71. van der Vliet, D. *et al.* On the importance of correcting for the uncompensated Ohmic resistance in model experiments of the Oxygen Reduction Reaction. *J. Electroanal. Chem.* **647**, 29–34 (2010).
72. Menzel, A. *et al.* High-density electrosorbed carbon monoxide monolayers on Pt(111) under atmospheric pressure. *Phys. Rev. B* **75**, 35426 (2007).
73. Lucas, C. A., Marković, N. M., Tidswell, I. M. & Ross, P. N. In situ X-ray scattering study of the Pt(111)-solution interface: Ordered anion structures and their influence on copper underpotential deposition. *Phys. B Condens. Matter* **221**, 245–250 (1996).
74. You, H., Zurawski, D. J., Nagy, Z. & Yonco, R. M. In-situ x-ray reflectivity study of incipient oxidation of Pt(111) surface in electrolyte solutions. *J. Chem. Phys.* **100**, 4699–4702 (1994).
75. Liu, Y., Barbour, A., Komanicky, V. & You, H. X-ray Crystal Truncation Rod Studies of Surface Oxidation and Reduction on Pt(111). *J. Phys. Chem. C* **120**, 16174–16178 (2016).
76. Tidswell, I. M., Markovic, N. M. & Ross, P. N. Potential dependent surface structure of the Pt(1 1 1) electrolyte interface. *J. Electroanal. Chem.* **376**, 119–126 (1994).
77. Wakisaka, M., Udagawa, Y., Suzuki, H., Uchida, H. & Watanabe, M. Structural effects

on the surface oxidation processes at Pt single-crystal electrodes studied by X-ray photoelectron spectroscopy. *Energy Environ. Sci.* **4**, 1662–1666 (2011).
78. Jerkiewicz, G., Vatankhah, G., Lessard, J., Soriaga, M. P. & Park, Y.-S. Surface-oxide growth at platinum electrodes in aqueous H2SO4: Reexamination of its mechanism through combined cyclic-voltammetry, electrochemical quartz-crystal nanobalance, and Auger electron spectroscopy measurements. *Electrochim. Acta* **49**, 1451–1459 (2004).
79. Conway, B. E., Barnett, B., Angerstein-Kozlowska, H. & Tilak, B. V. A surface-electrochemical basis for the direct logarithmic growth law for initial stages of extension of anodic oxide films formed at noble metals. *J. Chem. Phys.* **93**, 8361–8373 (1990).
80. Topalov, A. A. *et al.* Towards a comprehensive understanding of platinum dissolution in acidic media. *Chem. Sci.* **5**, 631–638 (2014).
81. Liu, Y. *et al.* Stability Limits and Defect Dynamics in Ag Nanoparticles Probed by Bragg Coherent Diffractive Imaging. *Nano Lett.* **17**, 1595–1601 (2017).
82. Parsons, R. Structural effects on adsorption at the solid metal/electrolyte interface. *J. Electroanal. Chem. Interfacial Electrochem.* **150**, 51–57 (1983).
83. Kuzume, A., Herrero, E. & Feliu, J. M. Oxygen reduction on stepped platinum surfaces in acidic media. *J. Electroanal. Chem.* **599**, 333–343 (2007).
84. Lide, D. R., Baysinger, G. & Berger, L. I. *CRC Handbook of Chemistry and Physics*. (CRC Press, 2004).
85. Shannon, R. D. Revised effective ionic radii and systematic studies of interatomic distances in halides and chalcogenides. *Acta Crystallogr. Sect. A* **32**, 751–767 (1976).
86. Schlögl, K., Mayrhofer, K. J. J., Hanzlik, M. & Arenz, M. Identical-location TEM investigations of Pt/C electrocatalyst degradation at elevated temperatures. *J. Electroanal. Chem.* **662**, 355–360 (2011).
87. Arenz, M. & Zana, A. Fuel cell catalyst degradation: Identical location electron microscopy and related methods. *Nano Energy* **29**, 299–313 (2016).
88. Nikkuni, F. R., Dubau, L., Ticianelli, E. A. & Chatenet, M. Accelerated degradation of Pt3Co/C and Pt/C electrocatalysts studied by identical-location transmission electron microscopy in polymer electrolyte environment. *Appl. Catal. B Environ.* **176–177**, 486–499 (2015).
89. Hodnik, N. *et al.* Severe accelerated degradation of PEMFC platinum catalyst: A thin film IL-SEM study. *Electrochem. commun.* **30**, 75–78 (2013).
90. Borup, R. *et al.* Scientific Aspects of Polymer Electrolyte Fuel Cell Durability and Degradation. *Chem. Rev.* **107**, 3904–3951 (2007).
91. Dicks, D. R. *Early Greek Astronomy to Aristotle (Aspects of Greek and Roman Life)*. (Cornell University Press, 1970).
92. CHARLSON, R. J. *et al.* Climate Forcing by Anthropogenic Aerosols. *Science (80-.).* **255**, 423 LP-430 (1992).
93. Allen, C. D. *et al.* A global overview of drought and heat-induced tree mortality reveals emerging climate change risks for forests. *For. Ecol. Manage.* **259**, 660–684 (2010).
94. Available at: https://www.tfes.org. (Accessed: 26th September 2018)
95. Available at: https://www.eia.gov. (Accessed: 26th September 2018)
96. Available at: https://www.eia.gov/totalenergy/data/annual/showtext.php?t=ptb1101. (Accessed:

26th September 2018)
97. Available at: http://www.worldometers.info/world-population/world-population-by-year/. (Accessed: 26th September 2018)
98. Lewis, N. S. & Nocera, D. G. Powering the planet: Chemical challenges in solar energy utilization. *Proc. Natl. Acad. Sci.* **103**, 15729 LP-15735 (2006).
99. Nocera, D. G. Chemistry of Personalized Solar Energy. *Inorg. Chem.* **48**, 10001–10017 (2009).
100. Liu, C., Colón, B. C., Ziesack, M., Silver, P. A. & Nocera, D. G. Water splitting–biosynthetic system with CO₂ reduction efficiencies exceeding photosynthesis. *Science (80-.).* **352**, 1210 LP-1213 (2016).
101. Torella, J. P. *et al.* Efficient solar-to-fuels production from a hybrid microbial–water-splitting catalyst system. *Proc. Natl. Acad. Sci.* **112**, 2337 LP-2342 (2015).
102. Dresselhaus, M. S. & Thomas, I. L. Alternative energy technologies. *Nature* **414**, 332 (2001).
103. Cook, T. R. *et al.* Solar Energy Supply and Storage for the Legacy and Nonlegacy Worlds. *Chem. Rev.* **110**, 6474–6502 (2010).
104. Reece, S. Y. *et al.* Wireless Solar Water Splitting Using Silicon-Based Semiconductors and Earth-Abundant Catalysts. *Science (80-.).* **334**, 645 LP-648 (2011).
105. Nocera, D. G. The Artificial Leaf. *Acc. Chem. Res.* **45**, 767–776 (2012).
106. Blankenship, R. E. *et al.* Comparing Photosynthetic and Photovoltaic Efficiencies and Recognizing the Potential for Improvement. *Science (80-.).* **332**, 805 LP-809 (2011).
107. Esswein, A. J. & Nocera, D. G. Hydrogen Production by Molecular Photocatalysis. *Chem. Rev.* **107**, 4022–4047 (2007).
108. Available at: https://www.eia.gov/environment/emissions/carbon/. (Accessed: 26th September 2018)
109. Cortright, R. D., Davda, R. R. & Dumesic, J. A. Hydrogen from catalytic reforming of biomass-derived hydrocarbons in liquid water. *Nature* **418**, 964 (2002).
110. Huber, G. W., Iborra, S. & Corma, A. Synthesis of Transportation Fuels from Biomass: Chemistry, Catalysts, and Engineering. *Chem. Rev.* **106**, 4044–4098 (2006).
111. Holladay, J. D., Hu, J., King, D. L. & Wang, Y. An overview of hydrogen production technologies. *Catal. Today* **139**, 244–260 (2009).
112. Cheng, X. *et al.* A review of PEM hydrogen fuel cell contamination: Impacts, mechanisms, and mitigation. *J. Power Sources* **165**, 739–756 (2007).
113. Baschuk, J. J. & Li, X. Carbon monoxide poisoning of proton exchange membrane fuel cells. *Int. J. Energy Res.* **25**, 695–713 (2001).
114. Available at: https://www.eia.gov/renewable/afv/users.php?fs=a&ufueltype=HYD. (Accessed: 26th September 2018)
115. Gust, D., Moore, T. A. & Moore, A. L. Solar Fuels via Artificial Photosynthesis. *Acc. Chem. Res.* **42**, 1890–1898 (2009).
116. Evans, D. J. & Pickett, C. J. Chemistry and the hydrogenases. *Chem. Soc. Rev.* **32**, 268–275 (2003).
117. Rauchfuss, T. B. Research on Soluble Metal Sulfides: From Polysulfido Complexes to Functional Models for the Hydrogenases. *Inorg. Chem.* **43**, 14–26 (2004).
118. SIEGBAHN, P. E. R. E. M. B. T.-A. in I. C. PROTON AND ELECTRON TRANSFERS IN [NiFe] HYDROGENASE. in *Advances in Inorganic Chemistry* **56**, 101–125 (Academic Press, 2004).
119. Volbeda, A. & Fontecilla-Camps, J. C. The active site and catalytic mechanism of NiFe

hydrogenases. *Dalt. Trans.* 4030–4038 (2003). doi:10.1039/B304316A
120. Lamle, S. E., Vincent, K. A., Halliwell, L. M., Albracht, S. P. J. & Armstrong, F. A. Hydrogenase on an electrode: a remarkable heterogeneous catalyst. *Dalt. Trans.* 4152–4157 (2003). doi:10.1039/B306234C
121. Mejia-Rodriguez, R., Chong, D., Reibenspies, J. H., Soriaga, M. P. & Darensbourg, M. Y. The Hydrophilic Phosphatriazaadamantane Ligand in the Development of H2 Production Electrocatalysts: Iron Hydrogenase Model Complexes. *J. Am. Chem. Soc.* **126**, 12004–12014 (2004).
122. Rees, D. C. & Howard, J. B. The Interface Between the Biological and Inorganic Worlds: Iron-Sulfur Metalloclusters. *Science (80-.).* **300**, 929 LP-931 (2003).
123. Lee, S. C. & Holm, R. H. Speculative synthetic chemistry and the nitrogenase problem. *Proc. Natl. Acad. Sci.* **100**, 3595 LP-3600 (2003).
124. Lembke, D., Bertolazzi, S. & Kis, A. Single-Layer MoS2 Electronics. *Acc. Chem. Res.* **48**, 100–110 (2015).
125. Donnet, C., Martin, J. M., Le Mogne, T. & Belin, M. Super-low friction of MoS2 coatings in various environments. *Tribol. Int.* **29**, 123–128 (1996).
126. Lauritsen, J. V *et al.* Atomic-scale insight into structure and morphology changes of MoS2 nanoclusters in hydrotreating catalysts. *J. Catal.* **221**, 510–522 (2004).
127. Besenbacher, F. *et al.* Recent STM, DFT and HAADF-STEM studies of sulfide-based hydrotreating catalysts: Insight into mechanistic, structural and particle size effects. *Catal. Today* **130**, 86–96 (2008).
128. Lauritsen, J. V *et al.* Location and coordination of promoter atoms in Co- and Ni-promoted MoS2-based hydrotreating catalysts. *J. Catal.* **249**, 220–233 (2007).
129. Tuxen, A. *et al.* Size Threshold in the Dibenzothiophene Adsorption on MoS2 Nanoclusters. *ACS Nano* **4**, 4677–4682 (2010).
130. Tuxen, A. K. *et al.* Atomic-scale insight into adsorption of sterically hindered dibenzothiophenes on MoS2 and Co–Mo–S hydrotreating catalysts. *J. Catal.* **295**, 146–154 (2012).
131. Kibsgaard, J. *et al.* Comparative atomic-scale analysis of promotional effects by late 3d-transition metals in MoS2 hydrotreating catalysts. *J. Catal.* **272**, 195–203 (2010).
132. Temel, B. *et al.* Atomic-scale insight into the origin of pyridine inhibition of MoS2-based hydrotreating catalysts. *J. Catal.* **271**, 280–289 (2010).
133. Tuxen, A. *et al.* An atomic-scale investigation of carbon in MoS2 hydrotreating catalysts sulfided by organosulfur compounds. *J. Catal.* **281**, 345–351 (2011).
134. Lauritsen, J. V & Besenbacher, F. Atom-resolved scanning tunneling microscopy investigations of molecular adsorption on MoS2 and CoMoS hydrodesulfurization catalysts. *J. Catal.* **328**, 49–58 (2015).
135. Kibsgaard, J. *et al.* Scanning tunneling microscopy studies of TiO2-supported hydrotreating catalysts: Anisotropic particle shapes by edge-specific MoS2–support bonding. *J. Catal.* **263**, 98–103 (2009).
136. Hinnemann, B. *et al.* Biomimetic Hydrogen Evolution: MoS2 Nanoparticles as Catalyst for Hydrogen Evolution. *J. Am. Chem. Soc.* **127**, 5308–5309 (2005).
137. Jaramillo, T. F. *et al.* Identification of Active Edge Sites for Electrochemical H₂ Evolution from MoS₂ Nanocatalysts. *Science (80-.).* **317**, 100 LP-102 (2007).
138. Land, T. A., Michely, T., Behm, R. J., Hemminger, J. C. & Comsa, G. STM investigation of single layer graphite structures produced on Pt(111) by hydrocarbon

decomposition. *Surf. Sci.* **264**, 261–270 (1992).
139. Gamo, Y., Nagashima, A., Wakabayashi, M., Terai, M. & Oshima, C. Atomic structure of monolayer graphite formed on Ni(111). *Surf. Sci.* **374**, 61–64 (1997).
140. Forbeaux, I., Themlin, J.-M. & Debever, J.-M. Heteroepitaxial graphite on $6H\ensuremath{-}\mathrm{SiC}(0001):$ Interface formation through conduction-band electronic structure. *Phys. Rev. B* **58**, 16396–16406 (1998).
141. Gao, W., Alemany, L. B., Ci, L. & Ajayan, P. M. New insights into the structure and reduction of graphite oxide. *Nat. Chem.* **1**, 403 (2009).
142. Thomsen, C. & Reich, S. Double Resonant Raman Scattering in Graphite. *Phys. Rev. Lett.* **85**, 5214–5217 (2000).
143. Dresselhaus, M. S. & Dresselhaus, G. Intercalation compounds of graphite. *Adv. Phys.* **51**, 1–186 (2002).
144. Ferrari, A. C. Raman spectroscopy of graphene and graphite: Disorder, electron–phonon coupling, doping and nonadiabatic effects. *Solid State Commun.* **143**, 47–57 (2007).
145. Manzeli, S., Ovchinnikov, D., Pasquier, D., Yazyev, O. V & Kis, A. 2D transition metal dichalcogenides. *Nat. Rev. Mater.* **2**, 17033 (2017).
146. Chhowalla, M. *et al.* The chemistry of two-dimensional layered transition metal dichalcogenide nanosheets. *Nat. Chem.* **5**, 263 (2013).
147. Wang, Q. H., Kalantar-Zadeh, K., Kis, A., Coleman, J. N. & Strano, M. S. Electronics and optoelectronics of two-dimensional transition metal dichalcogenides. *Nat. Nanotechnol.* **7**, 699 (2012).
148. Radisavljevic, B., Radenovic, A., Brivio, J., Giacometti, V. & Kis, A. Single-layer MoS2 transistors. *Nat. Nanotechnol.* **6**, 147 (2011).
149. Kam, K. K. & Parkinson, B. A. Detailed photocurrent spectroscopy of the semiconducting group VIB transition metal dichalcogenides. *J. Phys. Chem.* **86**, 463–467 (1982).
150. Mak, K. F., Lee, C., Hone, J., Shan, J. & Heinz, T. F. Atomically Thin ${\mathrm{MoS}}_{2}$: A New Direct-Gap Semiconductor. *Phys. Rev. Lett.* **105**, 136805 (2010).
151. Lukowski, M. A. *et al.* Enhanced Hydrogen Evolution Catalysis from Chemically Exfoliated Metallic MoS2 Nanosheets. *J. Am. Chem. Soc.* **135**, 10274–10277 (2013).
152. Ge, P. *et al.* Hydrogen evolution across nano-Schottky junctions at carbon supported MoS2 catalysts in biphasic liquid systems. *Chem. Commun.* **48**, 6484–6486 (2012).
153. Yu, Y. *et al.* High phase-purity 1T'-MoS2- and 1T'-MoSe2-layered crystals. *Nat. Chem.* **10**, 638–643 (2018).
154. Li, Y. *et al.* MoS2 Nanoparticles Grown on Graphene: An Advanced Catalyst for the Hydrogen Evolution Reaction. *J. Am. Chem. Soc.* **133**, 7296–7299 (2011).
155. Kibsgaard, J., Jaramillo, T. F. & Besenbacher, F. Building an appropriate active-site motif into a hydrogen-evolution catalyst with thiomolybdate [Mo3S13]2− clusters. *Nat. Chem.* **6**, 248 (2014).
156. Xie, J. *et al.* Defect-Rich MoS2 Ultrathin Nanosheets with Additional Active Edge Sites for Enhanced Electrocatalytic Hydrogen Evolution. *Adv. Mater.* **25**, 5807–5813 (2013).
157. Merki, D., Fierro, S., Vrubel, H. & Hu, X. Amorphous molybdenum sulfide films as catalysts for electrochemical hydrogen production in water. *Chem. Sci.* **2**, 1262–1267 (2011).
158. Karunadasa, H. I. *et al.* A Molecular MoS₂ Edge Site Mimic for

Catalytic Hydrogen Generation. *Science (80-.).* **335**, 698 LP-702 (2012).
159. Ding, Y. *et al.* First principles study of structural, vibrational and electronic properties of graphene-like MX2 (M=Mo, Nb, W, Ta; X=S, Se, Te) monolayers. *Phys. B Condens. Matter* **406**, 2254–2260 (2011).
160. Morales-Guio, C. G. & Hu, X. Amorphous Molybdenum Sulfides as Hydrogen Evolution Catalysts. *Acc. Chem. Res.* **47**, 2671–2681 (2014).
161. Vrubel, H. & Hu, X. Growth and Activation of an Amorphous Molybdenum Sulfide Hydrogen Evolving Catalyst. *ACS Catal.* **3**, 2002–2011 (2013).
162. Geng, X. *et al.* Pure and stable metallic phase molybdenum disulfide nanosheets for hydrogen evolution reaction. *Nat. Commun.* **7**, 10672 (2016).
163. Liu, C. *et al.* Vertical single or few-layer MoS2 nanosheets rooting into TiO2 nanofibers for highly efficient photocatalytic hydrogen evolution. *Appl. Catal. B Environ.* **164**, 1–9 (2015).
164. Yan, Y. *et al.* Vertically oriented MoS2 and WS2 nanosheets directly grown on carbon cloth as efficient and stable 3-dimensional hydrogen-evolving cathodes. *J. Mater. Chem. A* **3**, 131–135 (2015).
165. Tang, Y.-J. *et al.* Porous Molybdenum-Based Hybrid Catalysts for Highly Efficient Hydrogen Evolution. *Angew. Chemie Int. Ed.* **54**, 12928–12932 (2015).
166. Duerloo, K.-A. N., Li, Y. & Reed, E. J. Structural phase transitions in two-dimensional Mo- and W-dichalcogenide monolayers. *Nat. Commun.* **5**, 4214 (2014).
167. Wang, H. *et al.* Electrochemical Tuning of MoS2 Nanoparticles on Three-Dimensional Substrate for Efficient Hydrogen Evolution. *ACS Nano* **8**, 4940–4947 (2014).
168. Xie, J. *et al.* Controllable Disorder Engineering in Oxygen-Incorporated MoS2 Ultrathin Nanosheets for Efficient Hydrogen Evolution. *J. Am. Chem. Soc.* **135**, 17881–17888 (2013).
169. Ho, T. A. *et al.* Edge-On MoS2 Thin Films by Atomic Layer Deposition for Understanding the Interplay between the Active Area and Hydrogen Evolution Reaction. *Chem. Mater.* **29**, 7604–7614 (2017).
170. Schalenbach, M. *et al.* Nickel-molybdenum alloy catalysts for the hydrogen evolution reaction: Activity and stability revised. *Electrochim. Acta* **259**, 1154–1161 (2018).
171. Staszak-Jirkovský, J. *et al.* Design of active and stable Co–Mo–Sx chalcogels as pH-universal catalysts for the hydrogen evolution reaction. *Nat. Mater.* **15**, 197 (2015).
172. Huang, Y., Nielsen, R. J., Goddard, W. A. & Soriaga, M. P. The Reaction Mechanism with Free Energy Barriers for Electrochemical Dihydrogen Evolution on MoS2. *J. Am. Chem. Soc.* **137**, 6692–6698 (2015).